12 90

UNIVERSIDADE Ð
COIMBRA

António Francisco Gonçalves Figo de Carvalho

FAST ALGORITHM OF SIMULATION POSITRON EMISSION SPECIES GENERATION FOR A MULTI-BEAMLET PROTON THERAPY TREATMENT PLANS

September 2023

António Francisco Gonçalves Figo de Carvalho

FAST ALGORITHM OF SIMULATION POSITRON EMISSION SPECIES GENERATION FOR A MULTI-BEAMLET PROTON THERAPY TREATMENT PLANS

Dissertation for the degree of Master in Biomedical Engineering supervised by Professor Doctor Paulo Alexandre Vieira Crespo and Professor Doctor Andrey Morozov and presented to the Department of Physics of the Faculty of Sciences and Technology of the University of Coimbra.

September 2023

This work was developed in collaboration with:

LIP - Laboratório de Instrumentação e Física Experimental de Partículas

Acknowledgements

Abstract

Proton radiation therapy allows the deposition of energy concentrated in the tumor region while minimizing damage to the surrounding tissues. However, despite this advantage, there is a challenge in precisely stopping protons at the tumor site, which may result in under-irradiation of this region. Therefore, to mitigate these risks, a method of proton therapy range verification is necessary.

Positron emission tomography (PET) imaging is a practical approach for proton range verification. Nuclear interactions of the proton beam in tissue lead to positron-emitting isotopes, enabling PET image acquisition by utilizing beam-induced patient activation.

The primary objective of PET is to confirm the proton beam's range rather than the complete dose distribution. This is because the activation observed through PET does not directly correspond to the dose distribution. Therefore, with the purpose of verifying if the treatment is being delivered as planned, Monte Carlo codes capable of simulating nuclear interaction frequency and location are used. This enables the comparison of the predicted activity distribution with the measured activity distribution, and if there is any difference between these distributions, it is a sign that deviations in the treatment are occurring and thus need to be adjusted.

The TOF-PET for Proton Therapy (TPPT) consortium, a collaboration between American and Portuguese institutions, has designed an in-beam PET equipped with highly precise Time of Flight (TOF) capabilities for verifying the range during proton radiation therapy. To simulate the operation of the TOF-PET prototype designed by the TPPT consortium, the Laboratory of Instrumentation and Experimental Particles Physics (LIP) has created a framework developed using the Geant4 toolkit. The work carried out under this Master's project was developed along the following three contributions.

Firstly, test the part of the TPPT framework (TPPTsim) dedicated to the generation of the positron emitting species (PES).

Secondly, the role of the positron range in brain and bone tissue on the activity distribution was studied using the tools generated in the framework.

Thirdly, a faster algorithm to obtain the spatial distribution of PES was developed. This new approach does not rely on Monte-Carlo procedures.

At the end of this work it can be said that: (1) all necessary changes to TPPTsim have been conducted and a description manual has been created; (2) due to the presence of phosphorous and calcium in bone, both leading to the emission of positrons with higher energies, it is shown that positron range only has an impact on the bone activity; (3) the newly developed algorithm greatly decreases the time needed to obtain the spatial distribution of PES, however, proton fluence near the end of the proton path is not accurately represented resulting in a slightly lower mean proton range in comparison to what is observed experimentally by approximately 2 mm.

Keywords

Resumo

A terapia de radiação com protões permite a deposição de energia concentrada na região do tumor, minimizando os danos aos tecidos circundantes. No entanto, apesar dessa vantagem, existe um desafio em parar precisamente os protões no local do tumor, o que pode resultar na sub irradiação dessa região. Portanto, para mitigar estes riscos, é necessário um método de verificação do alcance de protões nesta terapia.

A tomografia por emissão de positrões (PET, do inglês Positron emission tomography) é uma abordagem prática para a verificação do alcance de protões. As interações nucleares do feixe de protões no tecido levam à formação de isótopos emissores de positrões, possibilitando a aquisição de imagens PET através da ativação do paciente induzida pelo feixe.

O principal objetivo do PET é confirmar o alcance do feixe de protões em vez da distribuição completa da dose. Isto ocorre porque a ativação observada por meio do PET não corresponde diretamente à distribuição da dose. Portanto, com o objetivo de verificar se o tratamento está a ser administrado conforme planejado, são usados códigos Monte Carlo capazes de simular a frequência e a localização das interações nucleares. Isto permite a comparação entre a distribuição de atividade prevista e a distribuição de atividade medida, e se houver diferença entre essas distribuições, é um sinal de que o tratamento não está a ocorrer como previsto e, portanto, precisa ser ajustado.

O consórcio TOF-PET para Prototerapia (TPPT, do inglês TOF-PET for Proton Therapy), uma colaboração entre instituições americanas e portuguesas, projetou um PET equipado com capacidades altamente precisas de tempo de voo (TOF, do inglês Time of Flight) para verificar o alcance de protões durante a terapia de radiação com protões. Para simular o funcionamento do protótipo TOF-PET projetado pelo consórcio TPPT, o Laboratório de Instrumentação e Física Experimental de Partículas (LIP) criou uma estrutura para simulações desenvolvida usando o software Geant4. O trabalho desenvolvido no âmbito deste projeto de Mestrado desenrolou-se nas três contribuições abaixo apresentadas.

Primeiramente, testou-se a parte da estrutura de simulações TPPT dedicada à geração das espécies emissoras de positrões (PES, do inglês positron emitting species).

De seguida, estudou-se o papel do alcance de positrões nos tecidos cerebrais e ósseos na distribuição de atividade usando as ferramentas geradas na estrutura de simulações.

Por fim, desenvolveu-se um algoritmo mais rápido para obter a distribuição espacial de PES. Esta nova abordagem não depende de procedimentos Monte Carlo.

Ao final deste trabalho, pode-se afirmar que: (1) todas as alterações necessárias na TPPTsim foram realizadas e um manual de descrição foi criado; (2)devido à presença de fósforo e cálcio nos ossos, ambos levando à emissão de positrões com energias mais elevadas, demonstra-se que o alcance dos positrões apenas

tem impacto na atividade óssea.; (3) o algoritmo recém desenvolvido reduz significativamente o tempo necessário para obter a distribuição espacial das PES, no entanto, a fluência de protões próxima ao final da trajetória dos protões não é representada com precisão, resultando num alcance médio de protões ligeiramente menor em comparação com o que é observado experimentalmente, cerca de 2 mm.

Palavras-Chave

Prototerapia, monitorização do alcance de protões, tomografia por emissão de positrões, tempo de voo, simulações de Monte Carlo, algoritmo rápido

Contents

List of Figures

List of Tables

Chapter 1

Introduction

1.1   Overview and motivation

Cancer is a term that refers to a collection of more than hundred distinct diseases, each characterized by the abnormal proliferation of cells. Unlike normal cells, which follow a regulated life cycle involving controlled growth, division, and replacement, cancer cells defy this organized process, multiplying uncontrollably. This uncontrolled growth leads to the development of tumors, known as malignant tumors or neoplasms. The critical distinction between cancer cells and normal cells lies in their growth patterns and behavior. While normal cells adhere to a regulated lifecycle, cancer cells evade this norm, persistently multiplying and generating abnormal cells. This unrestricted growth and invasive behavior define the hallmark characteristics of cancer cells [Mitra et al., 2018].

Cancer originates from changes in genes that govern how cells function, particularly their growth and division patterns. These genetic alterations leading to cancer can emerge through errors during cell division, as well as DNA damage caused by harmful environmental agents like the chemicals in tobacco smoke or ultraviolet rays from the sun. Additionally, certain genetic mutations can be inherited from parents, predisposing individuals to cancer. Although the body normally rids itself of cells with compromised DNA to avert cancer, this safeguarding mechanism weakens with age, contributing to an elevated cancer risk later in life [NCI, 2021]. According to the World Health Organization, in 2020 it is estimated that 19.3 million new cases and 10 million deaths occurred due to this disease [GCO, 2020].

As a form of cancer treatment there are different options available. These options are dependent on several factors depending on the conditions of the cancer and the patient's health. Amongst the most commonly used techniques are surgery, chemotherapy and radiation therapy [Mayo, 2022].

Over 50% of patients undergo radiation therapy. This treatment employs ionizing radiation to damage rapidly dividing cells' DNA and critical components, leading to tumor shrinkage and cell death. Measured in grays (Gy), radiation is delivered in divided doses called fractions, aiming to maximize cancer cell de-

struction while limiting harm to healthy tissues and organs [Chaput and Regnier, 2021].

Radiotherapy can be administered using different techniques, it can be delivered externally (external beam radiotherapy [EBRT]), internally (brachytherapy), or through intravenous radioisotope administration targeting specific tissues. EBRT, the most commonly used, employs linear accelerators to direct photons (x-rays) or particles (e.g. electrons, protons, carbon ions, etc.) at a target. The initial stage of preparing for EBRT involves a simulation session. This entails using imaging techniques like CT or MRI, placing markers or tattoos for patient positioning reference, and using immobilization tools on the treatment table. The radiation oncologist and physicists collaborate to design a treatment plan detailing the targeted tissue volume, required dose, and the safe delivery of the dose over multiple sessions [Chaput and Regnier, 2021].

Historically, photon therapy has been commonly used. This technique involves using intensity-modulated radiotherapy, volumetric modulated arc therapy, or 3-dimensional conformal radiotherapy to direct multiple x-ray beams at a tumor. However, this method has limitations due to the physics of photons, resulting in an unavoidable exit dose downstream from the target (overdose of healthy tissues being a concern). An alternative to resolve this particular problem is to use proton radiation therapy, which makes use of the Bragg peak phenomenon exhibited by protons to concentrate their energy deposition at the end of their path. Thus, by directing protons at the tumor the majority of the radiation dose is deposited precisely in the target area minimizing damage to the surrounding tissues [Baumann et al., 2020; Kryder, 2017]. Additionally, due to the intricate nature of tumor treatment volumes characterized by varying depths and thicknesses, it becomes necessary to adjust the beam energy. Thus, instead of using a monoenergetic beam it is necessary to modulate the beam energies in order to generate a spread out Bragg peak (SOBP), strategically spanning the required treatment area [Leeman et al., 2017].

Figure 1.1 shows the depth-dose curves typically for a monoenergetic proton beam, SOBP and X-ray beam.
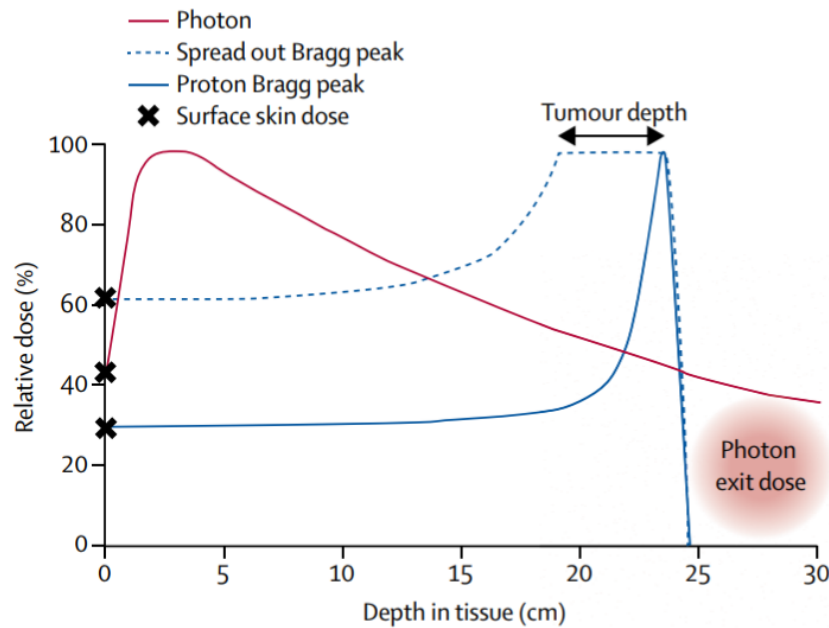
Figure 1.1: Comparison between the depth-dose curves for photon and proton beams. Taken from [Leeman et al., 2017]

While proton therapy holds potential advantages, a significant challenge lies in precisely stopping protons at the tumor site. This is due to the sensitivity of proton beams to varying tissue densities as they traverse the body towards the target. Additionally, as the beam penetrates greater depths, scattering effects lead to less sharp lateral and longitudinal margins. Changes in tissue composition, such as organ movement or alterations in bone position between treatments, can impact target coverage and surrounding tissue doses [Kryder, 2017]. Therefore, to mitigate these risks a method of proton therapy range verification is necessary.

Positron emission tomography (PET) imaging is a practical approach for proton range verification that dates back to the 1970s. Nuclear interactions of the proton beam in tissue lead to positron-emitting isotopes (PES), enabling PET image acquisition by utilizing beam-induced patient activation. For effective verification, PET scanners with minimal post-irradiation delay are preferred (e.g. in-beam PET). Key PES used in this process are ^{11}C and ^{15}O with half-lives of approximately 20 and 2 min, respectively, which when decayed lead to the generation of back-to-back gamma rays from positron-electron annihilation. Through the detection of these gamma rays, a 3D image of the irradiated region is reconstructed [Cho, 2014; Paganetti and El Fakhri, 2015].

The primary objective of PET is to confirm the proton beam's range rather than the complete dose distribution. This is because the activation observed through PET does not directly correspond to the dose distribution, given that protons primarily dissipate their energy through long-range interactions. Since PET images cannot directly match dose distribution, a distinct reference is required. For this purpose, Monte Carlo codes capable of simulating nuclear interaction frequency and location are used. This enables the creation of an expected PET image for comparison with the measured and reconstructed image, focusing on distal edge

signal [Paganetti and El Fakhri, 2015].

In-beam PET scanners present a valuable advantage by enabling real-time signal acquisition during treatment, thereby minimizing washout effects and achieving strong correlation between deposited dose and measured activity. However, the successful operation of these scanners demands attention to factors like beam alignment, patient positioning, and handlin. The inherent constraint of limited coverage, necessary to ensure the smooth passage of the treatment beam, introduces its own set of challenges, such as high image noise and artifacts in PET monitoring [Abouzahr et al., 2023]. To minimize these image artifacts and consecutively improve the reconstructed PET image, information of time-of-flight (TOF) should be included [Cambraia Lopes et al., 2016].

1.2 Objectives

This thesis was developed under the TOF-PET for Proton Therapy (TPPT) consortium, a collaboration between PETsys Electronics S.A. (Portugal), LIP – Laboratory of Instrumentation and Experimental Particles Physics (Portugal), ICNAS – Institute of Nuclear Sciences Applied to Health (Portugal), C2TN – Center for Nuclear Sciences and Technologies (Portugal), University of Texas at Austin (USA), and University of Texas MD Anderson Proton Therapy Center (USA) [UT Austin Portugal, 2020].

The project's objective is to showcase the viability of utilizing Positron Emission Tomography (PET) equipped with highly precise Time of Flight (TOF) capabilities for verifying the range during proton radiation therapy, so that later it can be used in medical sites such as the MD Anderson Cancer Center [UT Austin Portugal, 2020].

The goal of LIP's group is to develop a framework in order to simulate the operation of the TOF-PET prototype designed by the TPPT consortium. This framework is developed using the Geant4 toolkit, a software used to simulate particle interaction with matter. Using the tools developed within this framework allows the acquisition of the activity and image reconstruction resulting from the administered radiation during a treatment plan. These reconstructions can then be used for the purpose of verifying the accurate delivery of the treatment.

The objectives of this Master thesis consist in contributing to the framework developed by LIP's group, especially in the development of a fast algorithm of simulation of the positron-emitting activity generation for a proton therapy treatment plan created in the MD Anderson Cancer Center.

1.3 Master thesis structure

This document is structured into 7 chapters. Chapter 2, Theoretical Background, provides the theoretical background needed to comprehend the physical pro-

cesses discussed in this thesis. Chapter 3, Range Verification in Proton Therapy, summarizes the main techniques used for range verification in proton therapy, focusing mainly on positron emission tomography. Chapter 4, Simulation Framework, provides information regarding the framework developed by LIP-Coimbra group, focusing mainly on the TTPTsim part. Chapter 5, Computational Approaches for PES Generation Modeling, presents the different approaches available for PES generation in the framework. Chapter 6, Effect of the Positron Range on the Activity induced in Brain and Bone, provides information regarding the role of positron range in brain and bone on activity distribution. Chapter 7, Fast Algorithm, presents information and results regarding the algorithm developed during this master thesis. Chapter 8, Conclusions, highlights the main conclusions of this thesis and presents an outlook for future work.

1.4   My personal contribution to the project

My personal role in the work on the project was in the following:

1) I was the main beta-tester of the part of the TPPT framework dedicated to the generation of the positron emitting species. Due to my hand-on experience with the framework I was tasked and successfully conducted the development of the framework documentation (chapter 4) [github, 2023]

2) I have conducted a comprehensive simulation study on the role of the positron range in brain and bone tissue on the activity distribution (chapter 6)

3) I have developed a fast algorithm to obtain the spatial distribution of the positron emission species using an approach that does not rely on Monte-Carlo procedures (chapter 7)

Chapter 2

Theoretical Background

This chapter offers an overview of the primary interactions between charged particles and photons with matter. Along with this, information regarding the radioactive decay of radionuclides is also presented.

2.1 Interaction of charged particles with matter

The interaction of charged particles with matter can be characterized by two main aspects, one being the loss of the energy of the particle and the other the change in the particle's traveling direction. These aspects occur due to the particle's Coulomb interactions with matter such as inelastic interactions with the atomic electrons and elastic scattering on the nuclei. Less frequent than the preceding processes, there is also the case of nuclear reactions and bremsstrahlung [Leo, 1994].

To help explain the different processes with charged particles more clearly, charged particles can be divided into two groups: one composed of heavier particles like protons, and another of electrons and positrons [Leo, 1994]. In nuclear physics terminology, heavy charged particles comprise nuclei equal or heavier than iron and silicon. In radiobiology, heavy charged particles comprise nuclei equal or heavier than helium. In this thesis, heavy charged particles comprise all atomic nuclei.

2.1.1 Energy loss of heavy charged particles

In matter, heavy charged particles predominantly experience energy loss due to inelastic interactions. In these interactions the energy loss by the heavy charged particles is transferred to atoms, leading to ionization or excitation of the atom. Although the energy transferred in each interaction is a small fraction of the particle's total kinetic energy, the numerous interactions in a short distance result in significant cumulative energy loss. This type of interaction is categorized into two types: soft collisions that result in excitation and hard collisions that cause

ionization. In the case of hard collisions, sometimes the kinetic energy of the released electron is enough for said electron to cause a secondary ionization. This high energy electron is referred to as delta (or a knock-on) electron [Leo, 1994].

Although with a smaller frequency when compared to inelastic interactions, elastic scattering also occurs. In most cases, elastic scattering results in minimal energy transfer due to the larger masses of the nuclei in most materials compared to the incident particle. Thus, the primary contribution to energy loss still arises from interactions with atomic electrons [Leo, 1994].

2.1.1.1   Bethe-Bloch formula

To quantify the average energy loss per unit path length a quantity called stopping power is introduced. It can be represented as [Leo, 1994]:

$$S = -\frac{dE}{dx} \tag{2.1}$$

where the minus sign indicates that the energy is lost by the particle.

This quantity was first calculated by Bohr, but later a formula was developed by Bethe, Bloch and other authors and became known as Bethe-Bloch formula [Leo, 1994]:

$$-\frac{dE}{dx} = 2\pi N_a r_e^2 m_e c^2 \rho \frac{Z}{A} \frac{z^2}{\beta^2} ln(\frac{2m_e \gamma^2 v^2 W_{max}}{I^2}) - 2\beta^2 - \delta - 2\frac{C}{Z} \tag{2.2}$$

with

r_e : classical electron radius = 2.817 x 10^{13} cm

m_e : electron mass

N_a : Avogadro's number = $6.022 x 10^{23} mol^{-1}$

I : mean excitation potential

Z : atomic number of absorbing material

A : atomic weight of absorbing material

ρ : density of absorbing material

z : charge of incident particle in units of e

$\beta = \frac{v}{c}$ of the incident particle

$\gamma = \frac{1}{\sqrt{1-\beta^2}}$

δ : density correction

C : shell correction

W_{max} : maximum energy transfer in a single collision ($\simeq 2m_e c^2 \beta^2 \gamma^2$)

Equation 2.2 suggests that the energy loss of the incident particle is directly proportional to the Z/A ratio of the absorbing material and square of the charge of the incident particle, which in the case of a proton is equal to 1. Additionally, it is also proportional to the inverse square of the velocity of the incident particle.

An example of the energy loss by different particles in accordance with the Bethe-Bloch formula as a function of their kinetic energy is shown in Figure 2.1. The illustration in Figure 2.1 does not encompass the extremely low-energy range where the Bethe-Bloch formula becomes ineffective. When the particle's velocity is low and comparable to the orbital electrons' velocity within the material, the rate of energy loss, dE/dx, reaches a peak and then decreases steeply as the particle's velocity decreases. In this low energy region, multiple intricate factors contribute. Among these, a crucial aspect is the particle's tendency to pick up electrons for part of the time. This results in a reduction of the particle's effective charge and subsequently its stopping ability [Leo, 1994].
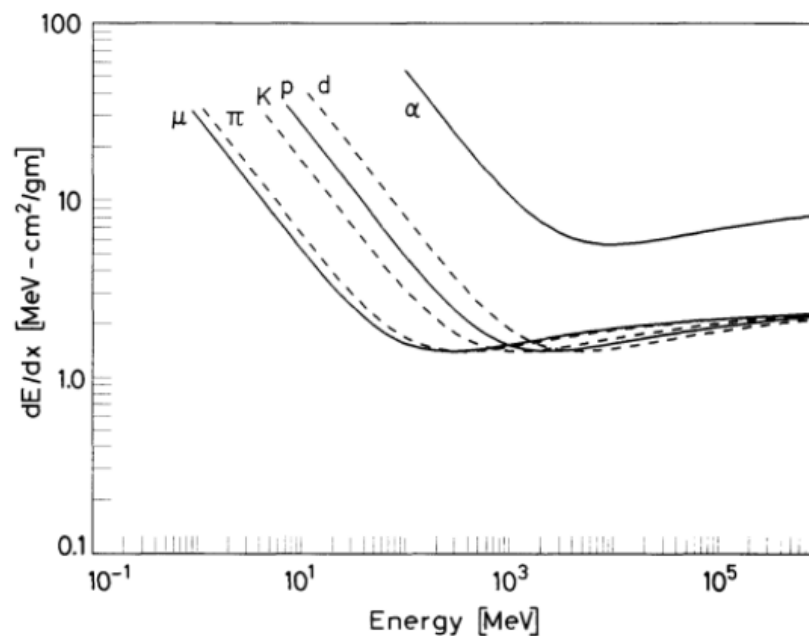
Figure 2.1: Illustration of the stopping power, dE/dx, of different particles as a function of their kinetic energy. Taken from [Leo, 1994]

2.1.1.2 The Bragg curve

The Bragg curve, shown in Figure 2.2, is a characteristic feature observed in heavy-charged particles and serves to illustrate the energy loss experienced by ionizing radiation as it traverses a material. This curve is particularly representative of the Bragg peak, an outcome attributed to the inverse square of the velocity of heavy-charged particles dependency of the stopping power. The occurrence of this peak is due to the fact that the interaction probability undergoes a rapid increase just before the particle comes to a complete stop. Throughout the majority of its trajectory, the particle retains a consistent charge, while the specific energy loss rises according to the inverse square dependence. Toward the terminal

portion of the trajectory, the particle's charge can decrease due to the pick up of electrons, leading to a decline in the rate of energy loss (dE/dx) [Nuclear-power, 2018].
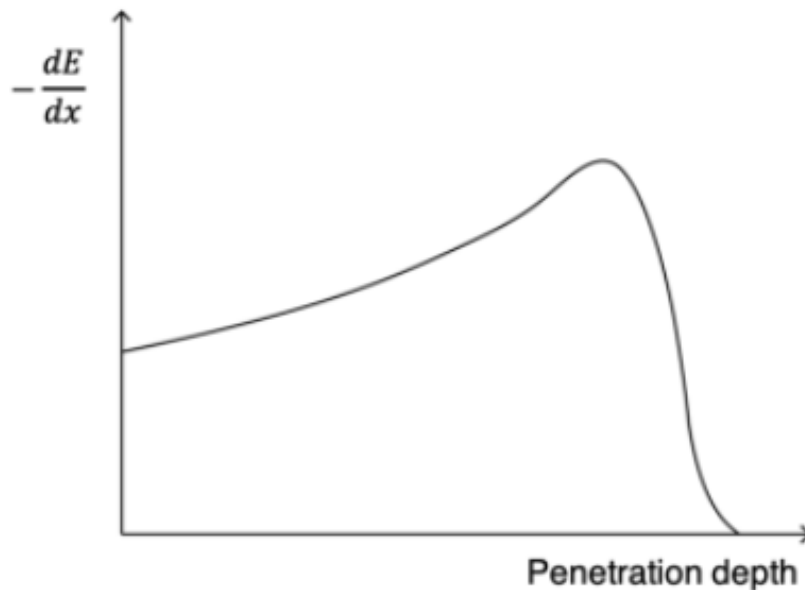
Figure 2.2: Illustration of a typical Bragg curve. It shows the variation of the stopping power as a function of the penetration depth. The particle is more ionizing towards the end of its path. Taken from [Leo, 1994]

2.1.1.3 Range

When interacting with matter, heavy charged particles travel a certain distance until their kinetic energy is fully dissipated. This distance, which can be better defined as the distance in a straight line from the particle's initial position to the particle's end position, is known as range. The range value is dependent on the type of particle and material considered as well as the initial kinetic energy of the particle [Leo, 1994].

Experimentally, the range value of a certain particle can be determined by directing a beam of said particles with the intended energy through varying material depths. Then the fraction of particles that manage to travel through the materials is recorded. Using the data from the experiment a graph of the fraction of transmitted particles versus absorber thickness can be created (Figure 2.3). This curve is named as range number-distance curve [Leo, 1994].

Approaching the range value, the drop in the fraction of particles that manage to travel through the materials occurs. However, this fraction does not immediately reach the expected background level (fraction of particles that manage to travel through the materials equal to zero). Instead, the decline follows a gradual slope across a range of thicknesses. This result occurs because of the statistical nature of energy loss, since even if two identical particles possess the same initial energy, they will not generally experience an identical number of interactions and

therefore the same energy loss. Consequently, measurements involving a group of identical particles display a statistical range distribution, centered around a mean value. This phenomenon is referred to as range straggling. This distribution is approximately Gaussian in shape. The midpoint of the descending slope in Figure 2.3 corresponds to the mean range, representing the thickness at which around half of the particles are absorbed [Leo, 1994].

However, more commonly desired is the thickness at which all particles are absorbed. In order to determine this point it involves the drawing of a tangent at the midpoint of the number-distance curve and extending it to the zero-level. This derived value is known as the extrapolated range [Leo, 1994].
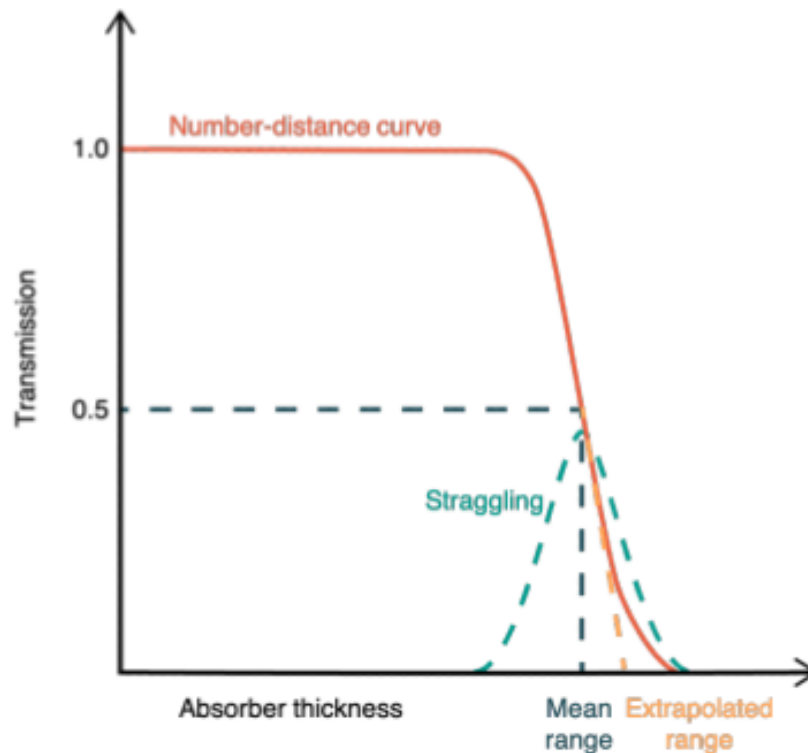
Figure 2.3: Illustration of a typical number-distance curve. Taken from [Leo, 1994]

From a theoretical point of view, in order to determine the range value the integration of the energy loss per unit path length for a given energy, T, has to be performed [Leo, 1994]:

$$S(T) = \int_0^T (\frac{dE}{dx})^{-1} dE \qquad (2.3)$$

This integration estimates the value for the mean range as if the particle traveled in a straight line, therefore ignoring the impact of multiple Coulomb scattering (discussed in detail in section 2.1.3) which could lead to the range value being longer than what it actually is. However, in the case of heavy charged particles, the influence of multiple Coulomb scattering is typically minor, which implies that the range value obtained can be considered as similar to the actual one [Leo,

1994].

2.1.1.4   Nuclear reactions

Nuclear reaction is a process in which a heavy charged particle, e.g. a proton, or the nucleons of a heavy charged particle (e.g. carbon ion), engage with the nucleons of a target nucleus. For this to occur, the energy of the incident particle must be sufficiently high to overcome the inherent electromagnetic repulsion between the protons within the interacting particles. This energy barrier is referred to as the Coulomb barrier. When the energy is below this barrier, the nuclei will merely repel each other [Matis, 2001].

In a collision between an incident particle and a target nucleus, two potential outcomes can occur: the incident particle may scatter elastically, leaving the target nucleus in its original state, or the target nucleus may experience internal excitement, subsequently decaying through the emission of radiation or nucleons [Matis, 2001].

For example, when a proton interacts with the nucleus of oxygen, ^{16}O, it can result in the production of an isotope of carbon, ^{11}C, and the emission of three protons and three neutrons.
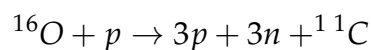
$$^{16}O + p \rightarrow 3p + 3n + ^{11}C$$

In this thesis this reaction will be abbreviated as 16O(p,3p3n)11C.

The parameter that indicates the probability of these nuclear reactions occurring is called cross-section, σ. More precisely, the concept of cross-section describes the probability of a specific atomic nucleus or subatomic particle undergoing a particular interaction when interacting with a specific type of incident particle. This parameter is quantified in terms of an area, and its numerical value is set in such a way that if the incident particle were to hit a circular area of equivalent size, perpendicular to its trajectory and centered on the target nucleus or particle, the anticipated reaction would take place. On the other hand, if the particle misses this defined area, the reaction would not occur. It is worth noting that the reaction cross section typically differs from the geometrical cross-sectional area of the target nucleus or particle. Despite not being a part of the International System of Units, the conventional unit used for cross-section is barn (b) which is equal to $10^{-24}m^2$ [Britannica, 2018].

For fast particle reactions, probabilities are often smaller than the nucleus's geometrical cross-section, typically in the millibarn range. The interaction probability depends on both the nucleus's area and the incoming particle's characteristics, such as its energy [Bailey, 2015].

2.1.2   Energy loss of electrons and positrons

Like heavy charged particles, electrons and positrons also lose some of their energy through inelastic collisions with the atomic electrons resulting in either ionization or excitation of the absorber atoms and through elastic scattering with the atomic nuclei. Additionally due to their small mass a new process has to be considered. This process is known as bremsstrahlung. This radiation is created due to acceleration of the electron/positron as it changes its travel direction due to the electrical interaction with the nucleus [Leo, 1994].

When low MeV energies are considered this process has a small effect in the total energy loss by these particles, however as the particle's energy increases the radiation created in this process also increases. After the energy passes a certain threshold the total energy loss is dominated by the radiation created through bremsstrahlung (Figure 2.4) [Leo, 1994].

The total energy loss for electrons and positrons is given by the following expression [Leo, 1994]:

$$\left(\frac{dE}{dx}\right)_{total} = \left(\frac{dE}{dx}\right)_{bremsstrahlung} + \left(\frac{dE}{dx}\right)_{collisions} \tag{2.4}$$
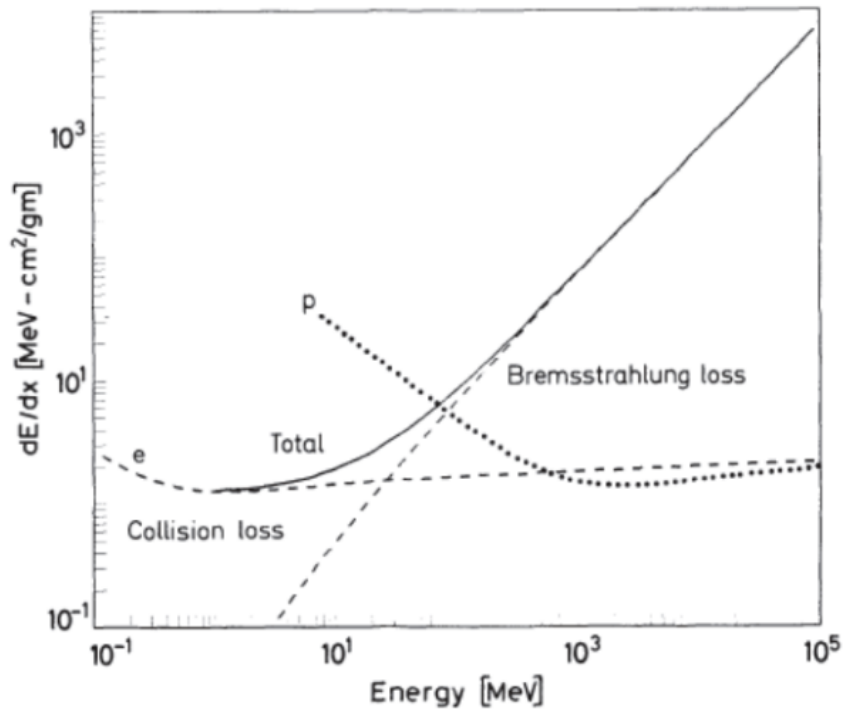
Figure 2.4: Comparison between the energy loss by radiation vs collision for electrons in copper as a function of their kinetic energy. Additionally, the energy loss for protons is also shown. Taken from [Leo, 1994]

2.1.3 Multiple Coulomb Scattering

Lastly, as already mentioned, charged particles also experience elastic Coulomb scattering due to interactions with the atomic nuclei. Assuming that the nuclei are much heavier then the incident particles the energy transferred to the nucleus is very small. Adding the fact that the incident particle suffers a small angular deflection each time it interacts with the nuclei it will follow a random zigzag path as it travels through the matter [Leo, 1994].

2.2 Radioactive decay

Radioactive decay is the emission of energy through ionizing radiation like alpha, beta, and gamma rays. Generally, an element's most prevalent form is its stable state, but there always exists an unstable variation. These unstable forms, known as radionuclides, emit ionizing radiation, making them radioactive. During decay, a radionuclide undergoes a transformation, resulting in it transforming into a different nucleus. This nucleus can undergo continuous changes into new nuclei until they attain stability, ceasing their radioactive emission. A significant portion of radionuclides experience a single decay event before reaching stability. However, some radionuclides exhibit multi-step decay processes. This sequence of nuclei transformation, culminating in a stable state, is termed a decay chain [EPA, 2023].

To quantify the number of decaying nuclides, $\triangle$ N, during a time interval, $\triangle$ t, the total number of existing nuclei, N, has to be considered. Since the number of existing nuclei will decrease as time progresses the following proportionality can be formulated [Grupen et al., 2010]:

$$\triangle N \sim -N \triangle t \qquad (2.5)$$

Which can also be represented using an infinitesimal time interval, dt, and infinitesimal number of nuclei, dN:

$$dN \sim -Ndt \qquad (2.6)$$

From this relation one can get an equation by introducing a constant of proportionality which in this case was named as decay constant and is represented by λ and given in $second^{-1}$.

$$dN = -\lambda Ndt \qquad (2.7)$$

By resolving the differential equation 2.7, the following equation is obtained:

$$N_t = N_0 e^{-\lambda t} \qquad (2.8)$$

where N_t and N_0 represent the number of existing nuclei at time t and t = 0 respectively.

Besides this type of quantification, there is another quantity used to characterize the number of decays that happen per second. It is called activity, A, and is given in becquerel (Bq). Thus, the activity is equal to the changing number of existing nuclei over a period of time. Since a decrease in the number of nuclei translates into a positive activity the following equation is obtained [Grupen et al., 2010]:

$$A = -\frac{\triangle N}{\triangle t} \tag{2.9}$$

Similarly to equation of the number of nuclei, equation 2.9 can be represented as:

$$A_t = A_0 e^{-\lambda t} \tag{2.10}$$

where A_t and A_0 represent the activity at time t and t = 0 respectively.

2.2.1 Half-life and lifetime

Half-life, $T_{1/2}$, value unique for every radionuclide, is the time at which fifty percent of the originally atomic nuclei have undergone decay [Grupen et al., 2010]. It can be represented using the decay constant:

$$T_{1/2} = \frac{ln2}{\lambda} \tag{2.11}$$

Lifetime τ is the time required for the sample's activity to decrease to $1/e$ of its original level [Leo, 1994]. It can be represented using the decay constant and therefore the half-life:

$$\tau = \frac{1}{\lambda} = \frac{T_{1/2}}{ln2} \tag{2.12}$$

2.2.2 Types of radioactive decay

The majority of radionuclides undergo decay through one or a mix of the subsequent processes: alpha decay, beta (plus and minus) decay, electron capture (EC) and gamma emission [Leo, 1994].

1) Alpha Decay

Alpha decay is a type of decay observed primarily in nuclei with considerable mass, characterized by an excess of protons and neutrons that renders them inherently unstable. During decay the nucleus emits an alpha particle,^4He [Leo, 1994]:

$$(Z, A) \rightarrow (Z - 2, A - 4) + \alpha$$
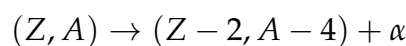
2) Beta Decay

Beta decay is a type of decay that can occur when a neutron or a proton within the nuclei, characterized by an excess of the respective nucleon, undergoes a weak-interaction decay, resulting in the emission of fast electrons or positrons known as beta particles [Leo, 1994].

In a nucleus rich in neutrons, a neutron can transform itself into a proton, thus emitted in the process an electron and antineutrino. This type of decay is known as beta minus [Leo, 1994]:

$$n \rightarrow p + e^- + \bar{\nu}$$
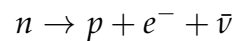
In a nucleus rich in protons, a proton can transform itself into a neutron, thus emitted in the process a positron and neutrino. This type of decay is known as beta plus [Leo, 1994]:

$$p \rightarrow n + e^+ + \nu$$
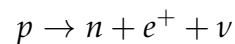
3) Electron Capture

Electron capture is a type of decay that can occur in a nucleus rich in protons via the capture of an orbital electron. Both particles will then combine to form a neutron and neutrino [Leo, 1994].

$$p + e^- \rightarrow n + \nu$$
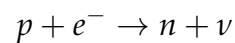
In this process, due to the participation of an orbital electron, a void is left in the atomic shell, which is then filled by another atomic electron, causing the emission of a characteristic x-rays. In some cases, this x-ray can be absorbed by an atomic electron, resulting in the emission of an Auger electron. The emission of the Auger electron leaves the atomic shell again with a vacancy which has to be filled with an outer shell electron, if available, leading to a further emission of a characteristic x-ray [Leo, 1994].

4) Gamma Emission

Gamma emission is another type of type of radioactive decay that can occur in an unstable nucleus. Unlike alpha or beta decay, this process does not emit charged particles from the nucleus. Instead, it involves the emission of a high-energy electromagnetic radiation (γ-ray) [Leo, 1994].

The emission of a gamma ray could lead to the occurrence of internal conversion. In this process, the gamma ray is absorbed by an orbital electron leading to the ejection of the electron. The void left in the atomic shell is then filled by an electron from an outer shell which leads to the emission of a characteristic x-ray and possible Auger electron [Leo, 1994].

2.3 Interaction of photons with matter

One of the products that result from the many possible interactions of certain particles are the photons, either it being x-rays or γ-rays [Leo, 1994].

When photons interact with matter the main processes that can occur are the following [Leo, 1994]:

1) Photoelectric effect

2) Compton scattering

3) Pair production

4) Rayleigh scattering

2.3.1 Photoelectric effect

The process of photoelectric effect involves the absorption of energy from an incident photon by an atomic electron, leading to the ejection of the electron from the atom. The kinetic energy obtained by the ejected electron is equal to the initial energy of the absorbed photon minus the binding energy of the electron B_e [Leo, 1994]:

$$E = hv - B_e \tag{2.13}$$

In order to conserve momentum, the photoelectric effect can only occur in the case of bound electrons, where the nucleus absorbs the recoil momentum [Leo, 1994].

The ejection of an atomic electron leads to the emission of characteristic x-rays and/or Auger electrons (more detailed information of this process in sub-section 2.2.2 - 3) Electron Capture) [Leo, 1994].

The photoelectric cross-section, σ_{ph} is given by [Podgoršak, 2010]:

$$\sigma_{ph} = \frac{8\pi}{3} r_e^2 \rho \frac{N_a}{A} Z^n \alpha^4 \sqrt{\frac{32}{\epsilon^7}} \tag{2.14}$$

with

r_e : classical electron radius = 2.817 x 10^{13} cm

ρ : density of absorbing material

N_a : Avogadro's number = $6.022 x 10^{23} mol^{-1}$

A : atomic weight of absorbing material

Z : atomic number of absorbing material

α : fine structure constant = 1/137

ϵ : photon energy divided by electron rest mass energy

n: power of the Z dependence. It ranges from n=4 at relative low photon energies to n=4.6 at higher photon energies.

Figure 2.5 shows the typical photoelectric cross-section as a function of the energy of the incident photon. For energies surpassing the atom's highest electron binding energy (K shell), the cross section remains small. It then sharply increases as the K-shell energy is approached. Following this, there's a significant drop in the cross section at the K absorption edge due to the unavailability of K-shell electrons for the photoelectric effect. Below this energy, the cross section rises again, with fluctuations at the L, M, and other electron level thresholds [Leo, 1994].
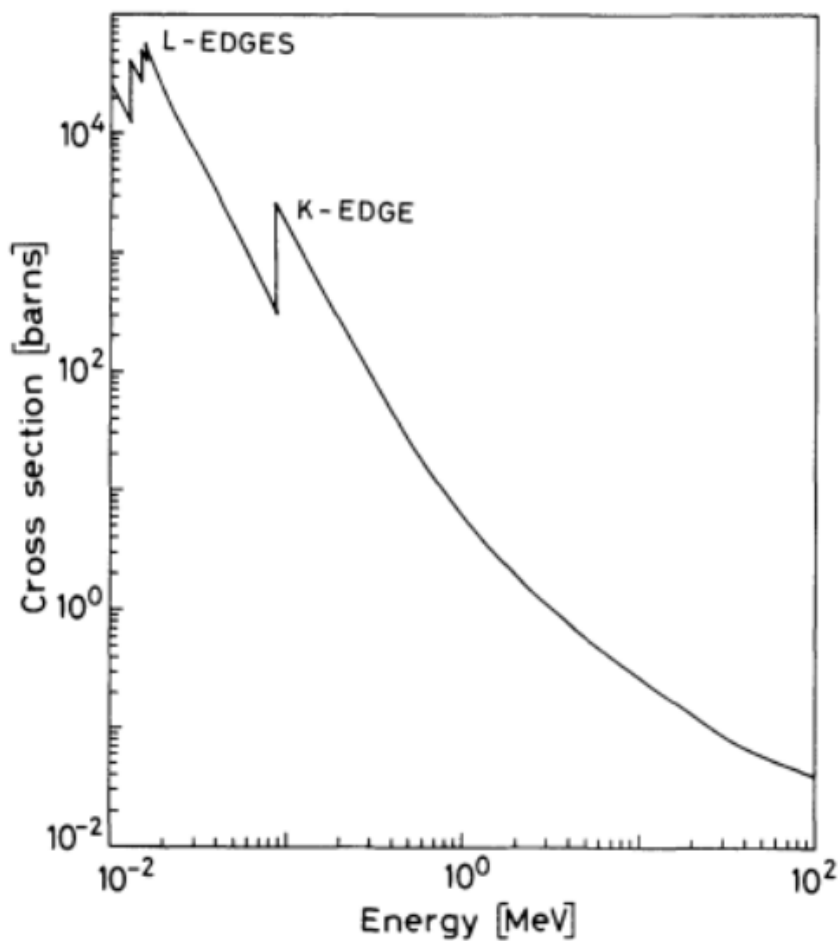
Figure 2.5: Photoelectric cross-section for lead. Taken from [Leo, 1994]

2.3.2 Compton scattering

The process of Compton scattering involves the scattering of photons by free electrons. While electrons within matter are typically bound, if the photon's energy considerably exceeds the electron binding energy, this binding energy's impact can be disregarded, permitting the electrons to be treated as free electrons [Leo, 1994].

18

So that the momentum and energy are conserved, when incident photon interacts with a free electron , the photon and electron are deflected with an angle of θ and φ, respectively, in relation to the initial direction of the incident photon (Figure 2.6) [Leo, 1994].
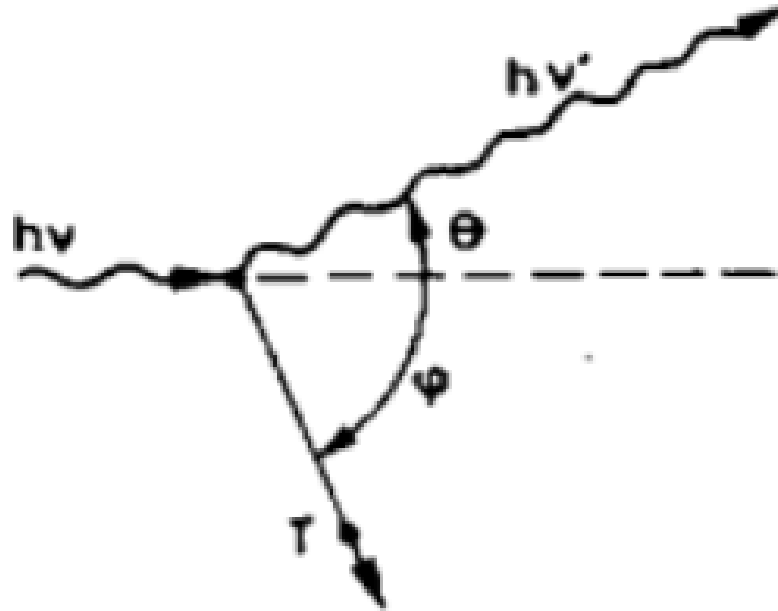
Figure 2.6: Illustration of the kinematics of Compton scattering. Taken from [Leo, 1994]

The scattered photon has an energy that is given by [Leo, 1994]:

$$hv' = \frac{hv}{1 + \gamma(1 - cos\theta)} \tag{2.15}$$

where $\gamma = \frac{hv}{m_e c^2}$. The scattered electron has an energy that is given by [Leo, 1994]:

$$T = hv - hv' = hv\frac{\gamma(1 - cos\theta)}{1 + \gamma(1 - cos\theta)} \tag{2.16}$$

The Compton scattering cross-section, σ_c is given by [Podgoršak, 2010]:

At very low energies:

$$\sigma_c = \frac{Z}{A}N_a\frac{8\pi}{3}r_e^2 \tag{2.17}$$

19

At high energies:

$$\sigma_c = \frac{Z}{A} N_a \pi r_e^2 \frac{2ln(2\epsilon) + 1.64}{2\epsilon} \tag{2.18}$$

with

Z : atomic number of absorbing material

A : atomic weight of absorbing material

N_a : Avogadro's number = $6.022 x 10^{23} mol^{-1}$

r_e : classical electron radius = 2.817×10^{13} cm

ϵ : photon energy divided by electron rest mass energy

Figure 2.7 shows the total Compton scattering cross-section, σ_c, as a function of the energy of the incident photon. Also represented is the Compton scattered cross-section, σ^S, which is defined as the average fraction of the total energy contained in the scattered photon, and the absorption cross-section, σ^a, which is defined as the average energy transferred to the scattered electron. The sum of σ^a with σ^S is equal to σ_c [Leo, 1994].

As it can be seen from Figure 2.7, the total Compton scattering cross-section decreases with the increase in the energy of the incident photon.
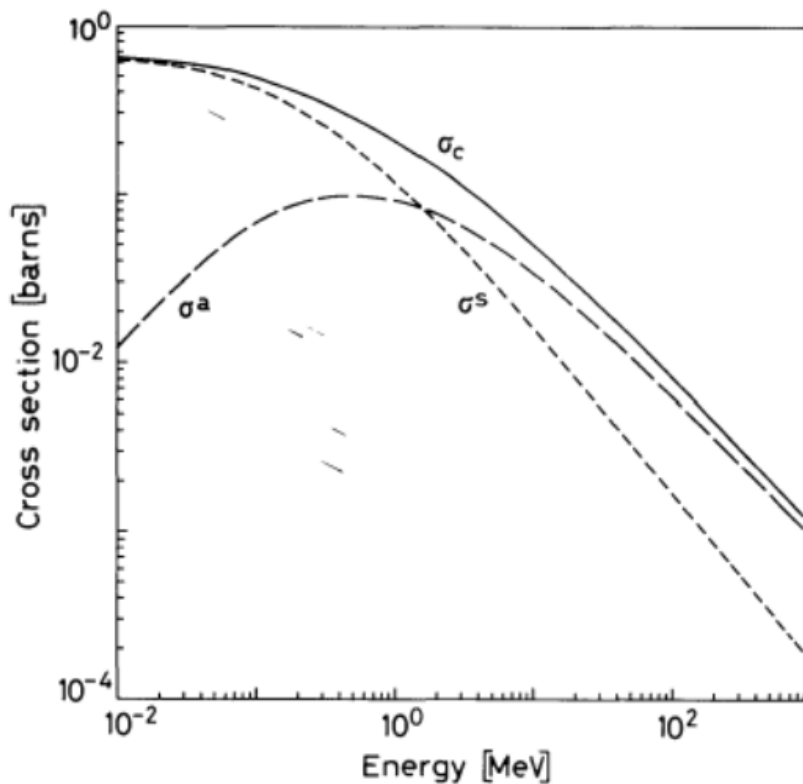
Figure 2.7: Total Compton scattering cross-sections. Taken from [Leo, 1994]

2.3.3 Pair Production

The process of pair production involves the conversion of a photon into an electron-positron pair. This phenomenon requires the presence of a third particle, typically a nucleus, to maintain momentum conservation. Additionally, for the pair to be formed, the photon's energy must exceed 1.022 MeV, which corresponds to the sum of the rest energy of an electron and positron [Leo, 1994].

Pair production can occur through two different mechanisms: standard pair production, where the extra momentum is absorbed by the atomic nucleus of the absorber, resulting in exceedingly small recoil energy and the creation of two particles (an electron and a positron); and electronic pair production, also known as triplet production, where an orbital electron of the absorber picks up the extra photon momentum, potentially leading to significant recoil energy, resulting in the creation of three particles (two electrons and a positron) leaving the interaction site [Podgoršak, 2010].

Regarding the generated positron, it will interact with the surrounding material until its energy decreases sufficiently for annihilation to occur through interaction with an electron. The result of this interaction is the creation of two annihilation gamma rays that are emitted in opposite directions with an energy of 511 keV [Leo, 1994].

The pair production cross-section, σ_p is given by [Podgoršak, 2010]:

$$\sigma_p = r_e^2 \rho \frac{N_a}{A} Z^2 \alpha P(\epsilon, Z) \qquad (2.19)$$

with

r_e : classical electron radius = 2.817 x 10^{13} cm

ρ : density of absorbing material

N_a : Avogadro's number = $6.022 x 10^{23} mol^{-1}$

A : atomic weight of absorbing material

Z : atomic number of absorbing material

α : fine structure constant = 1/137

$P(\epsilon, Z)$: function of the photon energy and atomic number of the absorber, as given in Table 2.1

ϵ : photon energy divided by electron rest mass energy

Figure 2.8 shows the pair production cross-section as a function of the energy of the photon. The cross-section is zero for energies below 1.0222 MeV and increases rapidly as the energy of the photon rises.

Field	Energy range	$P(\epsilon, Z)$
Nucleus	$1 \ll \epsilon \ll 1/(\alpha Z^{1/3})$	$\frac{28}{9}\ln(2\epsilon) - \frac{218}{27}$
Nucleus	$\epsilon \gg 1/(\alpha Z^{1/3})$	$\frac{28}{9}ln\frac{183}{Z^{1/3}} - \frac{2}{27}$
Nucleus	Outside the limits above but $\epsilon > 4$	$\frac{28}{9}ln(2\epsilon) - \frac{218}{27} - 1.027$
Electron	$\epsilon > 4$	$\frac{1}{Z}(\frac{28}{9}ln(2\epsilon) - 11.3)$

Table 2.1: Characteristics of atomic cross section for pair production in the field of the nucleus and in the field of an orbital electron. Taken from [Podgoršak, 2010]

.
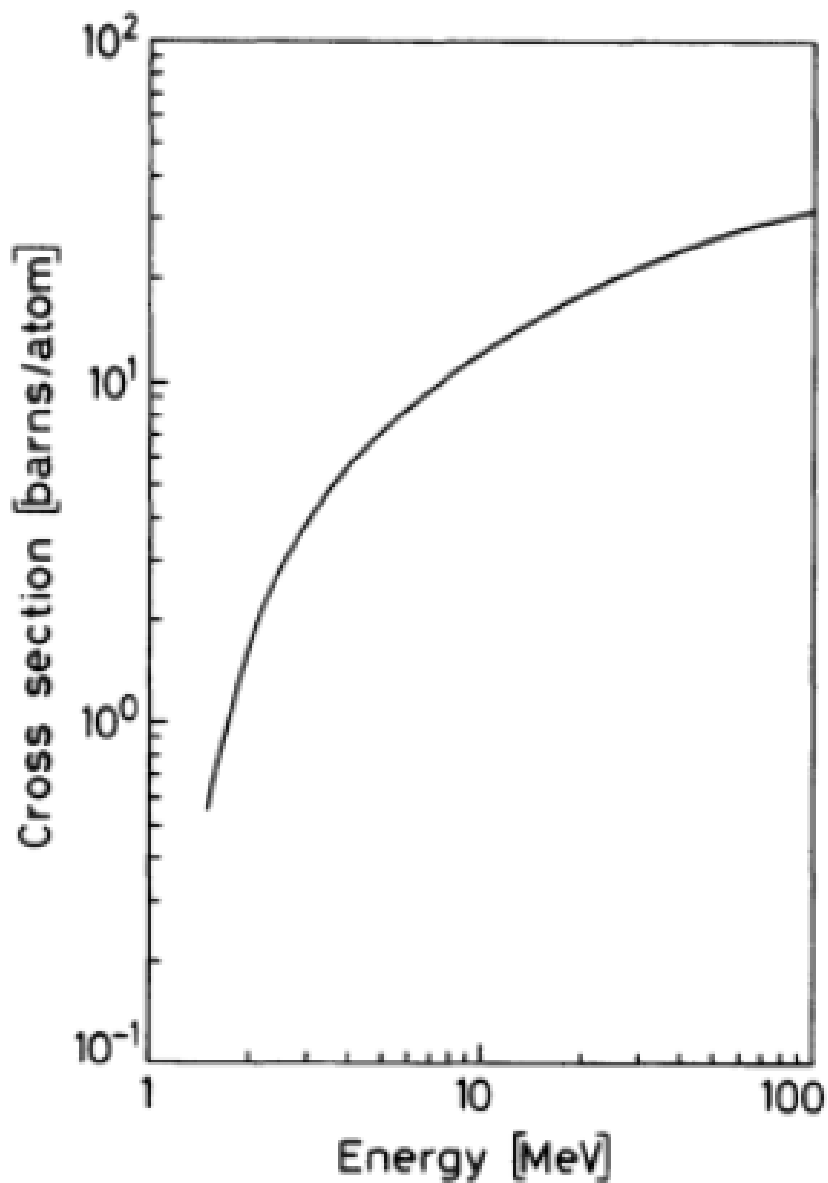
Figure 2.8: Pair production cross-section for lead. Taken from [Leo, 1994]

2.3.4 Rayleigh scattering

The process of Rayleigh scattering involves the scattering of photons due to the collective influence of the entire atom. During this process, all the electrons within the atom contribute coherently, leading to its alternative name, coherent scattering [Leo, 1994].

It is crucial to note that almost no energy is conveyed to the medium. The atoms do not undergo excitation or ionization; only the photon's trajectory is altered [Leo, 1994].

2.3.5 Interaction dominance

As could be seen in the previous sub-sections, the probability for a photon to undergo one of the described interaction processes depends on two main factors: one is the photon energy, E, and the other is the atomic number of the material, Z. The relative contributions of the three main interaction processes are shown in Figure 2.9 [Podgorsak, 2005].

In general, according to Figure 2.9, the photoelectric effect process predominance in heavier elements at lower photon energies, the Compton scattering process predominance in situations involving intermediate values of photon energy and the pair production process predominance in heavier elements at higher photon energies.

For example, a 100 keV photon will interact with a carbon (Z = 6) material mainly through Compton scattering and with a silver (Z = 47) material mainly through the photoelectric effect. At higher energies such as 10 MeV photons will interact with a carbon material mainly through Compton scattering and with a silver material mainly through pair production [Podgorsak, 2005].
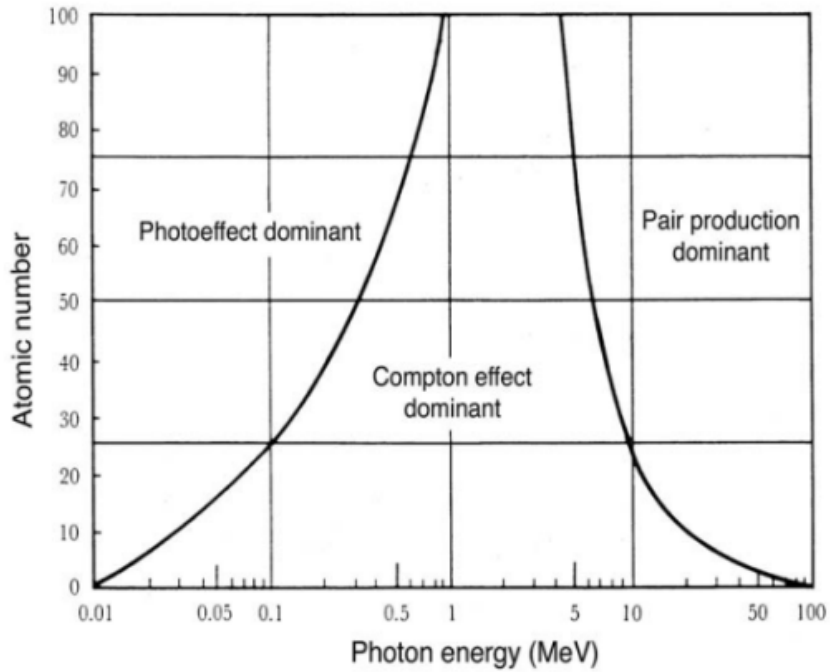
Figure 2.9: Illustration of the regions of relative predominance of the three main processes of photon interaction with matter. The left curve represents the region at which the cross-section of both photoelectric effect and compton scattering are equal and the right curve represents the region at which the cross-section of both compton scattering and pair production are equal. Taken from [Podgorsak, 2005]

Chapter 3

Range Verification in Proton Therapy

3.1 State of the art

The utilization of proton therapy is on the rise in radiation oncology, with an increasing number of patients undergoing this treatment. As previously mentioned, the growing interest in this technique is primarily due to the unique physical characteristics of the depth-dose curve, which features a dose peak called the Bragg peak. Unlike photon-based methods, proton treatment techniques consistently result in lower total energy deposition in patients, often referred to as integral dose. One contributing factor to this difference is the absence of an exit dose in proton therapy. Moreover, the Bragg peak concept offers the potential for precise targeting of critical structures, enhancing the flexibility of treatment planning compared to all modern forms of photon therapy [Paganetti, 2012].

To maximize the potential benefits of proton therapy, an accurate prediction of proton beam ranges within patients is crucial during both treatment planning and delivery. Inaccurate determination of safety margins has more significant implications in proton therapy compared to photon therapy. Underestimating margins in photon therapy could lead to insufficient tumor dosages, while in proton therapy, such underestimation could result in parts of the tumor receiving no dose. Additionally, due to range uncertainties, overdosage of healthy cells might occur, which can lead to the death of healthy cells [Paganetti, 2012].

Proton therapy introduces uncertainties that originate from various factors. Proton therapy treatment planning relies on computed tomography (CT) scans, which introduce uncertainties due to factors such as CT noise, artifacts, resolution limitations, and the Hounsfield unit (HU) conversion: CT scans are not only used to know the anatomy of the irradiated location but also to translate the CT data into relative stopping powers for proton beams using HU conversion methods. However, these conversions cannot be directly validated in vivo, contributing to potential range inaccuracies in treatment planning [Zhu and Fakhri, 2013].

In the context of proton therapy for curative treatment, where high doses (typically 40 to 80 Gy) are required, the treatment must be divided into daily fractions due to radiobiological reasons. However, this fractionation approach introduces

its own set of challenges. Firstly, because CT scans are not conducted before each treatment session, uncertainties can arise from variations in anatomical structures, such as tumor shrinkage or growth, or fluctuations in patient weight over the course of treatment, or even the filling/emptying of cavities with edema or mucus. Moreover, as treatment progresses, other sources of uncertainties come into play, including errors in patient setup and positioning, as well as potential movements of internal organs [Chaput and Regnier, 2021; Zhu and Fakhri, 2013].

Due to these problems, validation of proton beam range holds significant importance in guaranteeing the treatment is being administered correctly. Given that proton beams stop entirely within the body, real-time in vivo treatment monitoring of the proton beam range becomes challenging. There are two promising non-invasive methods that can be used for in vivo verification of the proton range. These methods are prompt gamma imaging (PGI) and positron emission tomography (PET) [Moteabbed et al., 2011; Zhu and Fakhri, 2013].

Prompt gamma imaging (PGI) is a technique that uses the prompt gamma (PG) rays which are created from the inelastic interactions between incoming protons and patient target nuclei. During certain interactions, the target nucleus becomes temporarily excited and then emits a photon (referred to as a PG) upon returning to its ground state. These PG photons are emitted isotropically and can be detected (within a few nanoseconds) after the nuclear interactions occur. Moreover, they have a sufficiently high production rate making their reconstruction feasible for real-time range verification during proton therapy [Moteabbed et al., 2011].

There are two main categories of prompt-gamma detection techniques for proton range verification: imaging techniques and non-imaging techniques [Wronska and Dauvergne, 2021].

Imaging techniques use a detector to create an image of the spatial distribution of prompt gamma emission positions in the patient. Important in this technique is the presence of a collimator. The image can then be used to directly reconstruct the range of the particle [Wronska and Dauvergne, 2021].

Non-imaging techniques do not create an image of the prompt gamma emission positions distribution. Instead, they measure the total number of prompt gammas emitted or the time difference between the emission of prompt gammas and the arrival of the charged particle at the detector. These measurements can then be used to determine indirectly the range of the particle [Wronska and Dauvergne, 2021].

PET is a technique that can be used for proton range monitoring in proton therapy. It achieves this by detecting gamma pairs generated during the annihilation of positrons. These positrons are emitted as a result of the inelastic interaction between the proton beam and atomic nuclei, giving rise to unstable isotopes decaying via the beta-plus mechanism [Moteabbed et al., 2011].

There are three types of PET imaging systems: in-beam (or online), off-line and in-room. In-beam PET is performed during the treatment. Off-line PET, the most common type , is performed in a different location after the proton therapy treatment has been completed. In-room PET is performed in the treatment room itself

immediately after the proton therapy has been completed [Moteabbed et al., 2011; Zhu and Fakhri, 2013].
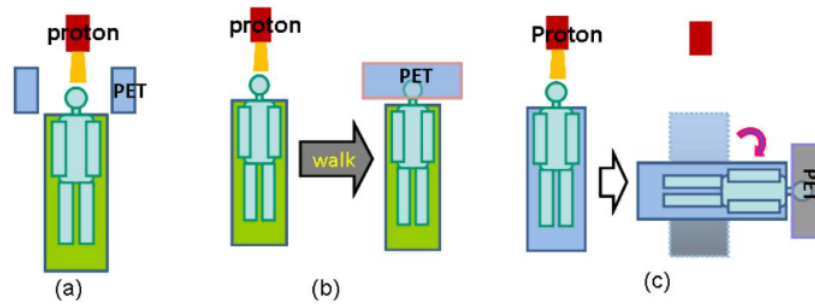
Figure 3.1: Illustration of the three types of PET: (a) in-beam PET; (b) offline PET (patient is moved to a different location from where proton therapy occurred); (c) in-roomPET (patient is moved to the PET scanner location which is in the same location where the proton therapy occurred). Taken from [Zhu and Fakhri, 2013]

Using PET to validate the proton beam range to guarantee if the treatment is being administered correctly comes with a challenge. This challenge arises because the activity reconstructed using this technique cannot be directly correlated with the dose distribution (Figure 3.2). Therefore, to enable comparison between PET scanner images and dose distribution, a distinct reference is needed. This involves using Monte Carlo codes, which not only simulate dose but also nuclear interaction frequency and location. These simulations create an expected PET image in the patient, aiding comparison with the measured and simulated image in terms of distal edge [Paganetti and El Fakhri, 2015].

Several challenges prevent the accuracy of range verification using this method. One concern is the precision of the Monte Carlo simulation, as accurate cross-sections for isotope production in tissues are lacking due to uncertainties in CT Hounsfield unit conversion to material composition and the focus of physics experiments on thin targets instead of a thick target, like a patient, where the proton energy spectrum is wider. Additionally, simulation results need correction for biological washout, considering changing activity in perfused tissues over time. Finally, there could also be some differences between simulated and measured results due to the activity depending on time (due to the half-lives of isotopes) and efficiency of PET detectors which have an impact on activity distribution obtained in PET [Paganetti and El Fakhri, 2015].
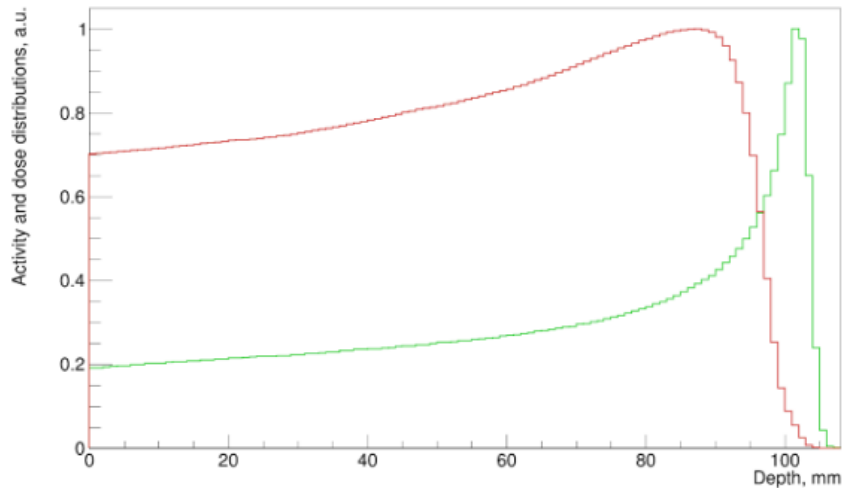
Figure 3.2: Normalized activity distribution (red curve) and dose distribution (green curve) obtained from the irradiation of a PMMA phantom with a proton beam. Obtained via simulation

3.2 Positron Emission Tomography

Positron emission tomography (PET) is an imaging technique that utilizes radioactive tracers to label molecules of interest. These tracers are then injected into the body and travel to the tissues where they are used or taken up. The tracers emit positrons that, when interacting with electrons in the tissue, produce almost back-to-back gamma rays. Through the detection of these gamma rays, a three-dimensional image of the distribution of the tracer in the body is reconstructed, allowing for the visualization and assessment of metabolic and functional processes within tissues and organs [Rohren et al., 2004; Ziegler, 2005].

This non-invasive imaging technique was developed in the early 1970s to obtain images of physiologic processes. It is now used in a variety of clinical applications, including oncology, cardiology, and neurology [Rohren et al., 2004; Ziegler, 2005].

3.2.1 PET principles

As already stated before, radionuclides used in PET decay and in the process emit a positron. The most commonly used radiopharmaceutical in PET imaging is 18F fluorodeoxyglucose (FDG). FDG is a glucose analog that is taken up by cells that are actively metabolizing glucose. This makes FDG a useful tracer for imaging tumors, as they tend to have higher glucose metabolism than healthy tissues. FDG is injected into the body and is taken up by cells within minutes. The PET detector assembly then images the distribution of FDG in the body. The images can be used to identify tumors, assess the extent of cancer, and monitor the response to treatment. Other commonly used radionuclides are ^{11}C, ^{15}O and ^{13}N [Rohren et al., 2004].

When a positron is emitted from these radioactive atoms, it travels through the tissue for a short distance. It gradually loses energy through interactions with electrons and atomic nuclei in the tissue. Eventually, the positron encounters an electron within the absorber, leading to either direct annihilation or annihilation through an intermediate process, resulting in the creation of a metastable hydrogen-like entity known as positronium (Ps). During annihilation two gamma rays of 511 keV each are emitted in almost opposite directions [Podgoršak, 2010; Ziegler, 2005].

A factor regarding the emission of the annihilation gammas is that they are not emitted at exactly 180 degrees apart due to the small residual momentum that positron and electron often have before annihilation. This effect is known as noncolinearity and the angular distribution of the gamma rays is approximately Gaussian, with a full width at half maximum (FWHM) of about 0.5 degrees [Radiology-key, 2016]. Another factor regarding this process is that a percentage of positron annihilations occur before the positron loses all of its kinetic energy. This is known as in-flight annihilation. The two gammas emitted in in-flight annihilation are not of identical energies because the positron kinetic energy is not zero when it annihilates [Bailey, 2015].

The simultaneous detection of two 511 keV gammas by PET scanner's detector is used to determine the location where the annihilation might have occurred. Through the repetition of the process, multiple positions of annihilation are determined and the data is used to reconstruct cross-sectional images of the body [Rohren et al., 2004].

To gain a solid grasp of how PET works, it is imperative to delve into its intricacies, including aspects such as scanner configuration and the gamma detection process. This information is discussed in the following sub-sections.

3.2.1.1 PET scanner

Scintillation detectors are extensively employed gamma-ray sensors, serving as the core technology for nearly all currently operational PET scanners. These detectors are constructed using dense scintillator crystal materials, which serve as the primary medium for interacting with gamma rays and high-energy photons. When these particles deposit energy within the scintillator material, it emits visible light. Subsequently, this emitted light is captured by a visible light photon detector, usually a photomultiplier tube (PMT), which then converts it into an electrical current. Modern scanners are substituting bulky PMT light detectors by silicon photomultipliers, a much smaller detector that has emerged in the last decade. These detectors (scintillators coupled to either PMTS or SiPMs) are positioned strategically around the imaging target, commonly forming a ring-shaped configuration, as observed in the PET scanner of Figure 3.3 [Cherry et al., 2011].

In the context of PET imaging, it is crucial to understand that 511 keV gamma rays travel in opposite directions along a nearly straight path and are detectable outside the body by the PET scanner. The detector electronics are interconnected in a way that if two detection occurrences happen unmistakably within a short time-

window, they are categorized as coincidence events. This classification signifies that these two detections stem from the same annihilation event. Notably, each coincidence event is assigned to a line of response (LOR) connecting the two pertinent detectors. Subsequently, these coincidence events are organized into arrays that align with projections across the patient's body and are later reconstructed using traditional tomographic techniques. The resulting images provide a visual depiction of the tracer's distribution within the subject's body [Tong et al., 2010; Washington, 1999].
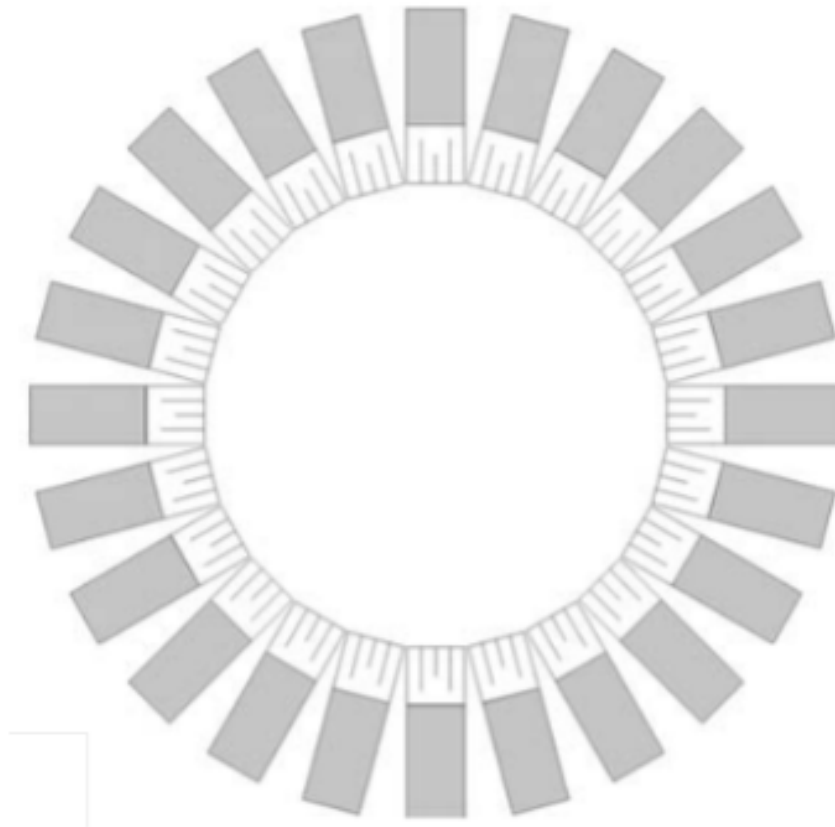
Figure 3.3: Diagram illustrating the transaxial view of a ring-shaped PET scanner. Taken from [Cherry et al., 2011]

3.2.1.2 Types of coincidence events

There are four types of coincidence events: true, scattered, random and multiple. The first three are illustrated in Figure 3.4 [Washington, 1999].

True coincidences occur when detectors detect both gamma rays from an annihilation event at the same time, without the gamma rays interacting before detection. Within the coincidence time-window, no other events are detected. Scattered coincidences occur when at least one of the detected gamma rays has undergone Compton scattering before being detected. This scattering changes the gamma ray's direction, often leading to misassignment of the coincidence event to the wrong LOR (LOR not corresponding to a real annihilation event) [Wash-

ington, 1999].

Random coincidences occur when two gamma rays, not originating from the same annihilation event, are detected within the system's coincidence time-window [Washington, 1999].

Multiple coincidences occur when more than two gamma rays are detected within the defined coincidence time-window. This scenario presents a challenge in determining which line of response the event should be assigned to, ultimately resulting in the event's rejection [Washington, 1999].
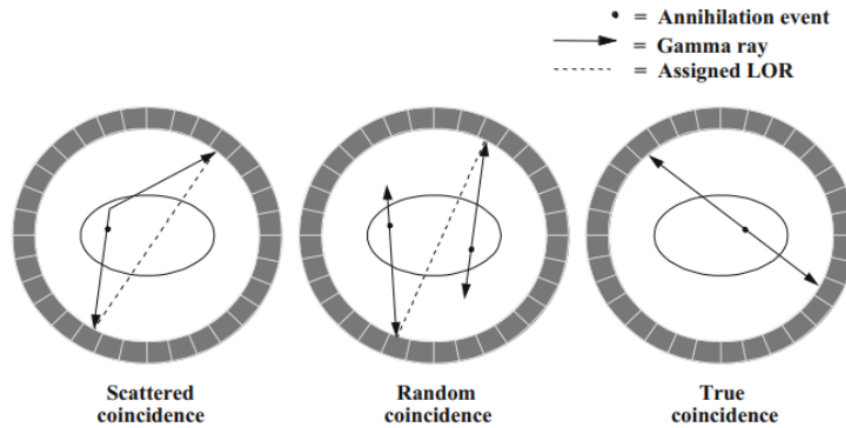
Figure 3.4: Three types of coincidences in a PET detector: True, Scatter, and Random. Taken from [Washington, 1999]

3.2.1.3 Time of flight PET

The process of coincidence detection involves pinpointing the positron annihilation event somewhere along or in the vicinity of a LOR. If in addition to this process the detection time of each gamma ray is included it is possible, depending on the temporal resolution of this detection (ability of a pair of detectors to distinguish the time discrepancy between the interactions of two coincident gamma rays), to estimate the location of the annihilation event along the LOR. This is where time-of-flight PET (TOF-PET) can be used [Flower, 2016; Schaart, 2021].

To determine the positron annihilation position along a LOR formed by detectors a and b, the coordinate x, indicating the distance from the LOR center to the annihilation point, is calculated as $x = (t_b - t_a)c/2$, where c represents the speed of light. This equation establishes a direct relationship between the coincidence time resolution, τ, and the spatial resolution, with the spatial resolution being proportional to τ. The principle of this imaging technique is shown in Figure 3.5 [Crespo et al., 2007].

Therefore, utilizing TOF information helps narrow down the annihilation point's location, significantly reducing the influence of Compton scattered and external photons entering the PET's field-of-view (FOV). This, in turn, minimizes background noise from scattered and random coincidences, ultimately enhancing the signal-to-noise ratio in TOF-PET images [Crespo et al., 2007].
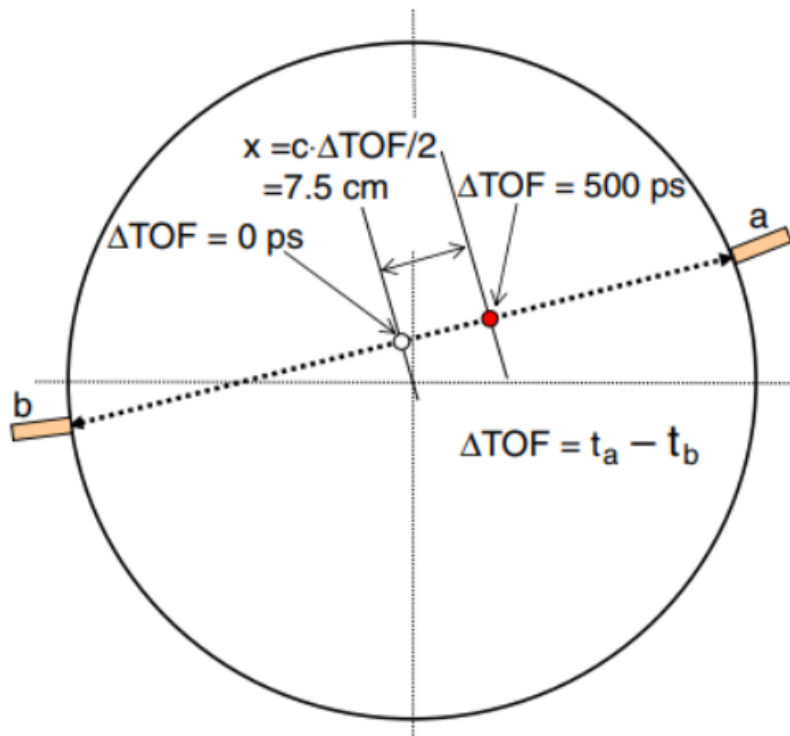
Figure 3.5: Principle of TOF-PET imaging. Within the circumference an annihilation event is located 7.5 cm from the middle of the LOR between detector a and b. Taken from [Crespo et al., 2007]

3.2.1.4   Spatial resolution

The main factors influencing PET image spatial resolution, which for a clinical PET scanner falls in the range of 4 to 5 mm, include scintillator crystal size, non-colinearity of annihilating gamma rays and the range of emitted positrons [CMG, 2018; Shukla and Kumar, 2006].

Detectors in a PET scanner form rings around a patient, with each pair defining a channel of around 4-6 mm width. Smaller scintillator crystals reduce spatial variation within channels, directly improving spatial resolution and accuracy [Shukla and Kumar, 2006].

Noncolinearity refers to deviations from the assumption that annihilated gamma rays travel exactly back-to-back. If positrons and electrons have residual momentum during annihilation, noncolinearity introduces directional error, potentially degrading image resolution. In a standard whole body PET scanner, noncolinearity within a 100 cm diameter may worsen resolution by about 0.2 cm [Shukla and Kumar, 2006].

Positrons are emitted from the unstable nucleus with a variable range of energies and move through the material for a limited distance while losing energy, ultimately leading to their annihilation. As the energy of positrons increases, their range correspondingly extends. For instance, the misposition error due to the positron range is approximately 0.2 mm for ^{18}F and increases to 1.2 mm for ^{15}O

positrons [Shukla and Kumar, 2006].

3.2.1.5 Sensitivity

The PET scanner's sensitivity, when considered with an empty (air) interior, is determined by the fraction of the annihilation gamma pairs created in the FOV that are detected and used for image reconstruction. This sensitivity is mainly influenced by the scanner's solid angle, Ω which is the extent it covers at the center of the FOV, and also by the squared detector efficiency (ability to effectively capture and record the gamma rays that arrive in the detector), ϵ, because both gamma rays must be detected for a coincidence to be recorded. With the current technology, sensitivity typically falls within the range of 0.5% to 5% [Flower, 2016].

3.2.2 In-beam TOF-PET for proton therapy range verification

As already mentioned, PET imaging of induced activity can happen either during proton irradiation (in-beam/online PET) or after treatment (off-line PET and in-room PET). Using in-beam PET, garanties that all produced PES have a significant contribution to the measured activity, while off-line images mostly display activity from PES whose half-life is higher than the time needed to prepare the PET imaging setup. The difference between these two techniques of imaging (during and after treatment administration) occurs due to the type of PES that are most commonly produced when a patient is irradiated by a proton beam. The primary PES produced are ^{11}C, ^{15}O and ^{10}C, with half-lives of approximately 20 minutes, 2 minutes, and 19 seconds, respectively. The crucial distinction arises mainly from the short half-lives of ^{10}C and ^{15}O. As a result, it becomes essential to employ in-beam PET for effectively capturing and quantifying the contributions of these short-lived isotopes [Enghardt et al., 2004; Knopf and Lomax, 2013].

It is also important to note that the in-beam approach for PET detection offers a distinct advantage over off-line range detection in terms of the quantity of beta plus decays available. This abundance of beta plus decays in the in-beam approach significantly reduces the required imaging time when compared to off-line PET detection. This shorter imaging duration has several merits, particularly in mitigating the impact of disruptive biological wash-out processes and patient discomfort [Knopf and Lomax, 2013].

However, in-beam PET also comes with some disadvantages. Integration of in-beam PET imaging equipment into the treatment environment poses geometric limitations due to beam portal requirements, often resulting in the ring-shaped scanner being divided into a dual-head configuration (Figure 3.6). This division into a dual-head configuration can potentially lead to challenges in image reconstruction. Specifically, there may be regions within the reconstructed images where spatial resolution is compromised. This limitation arises from the fact that, in this configuration, there exists the possibility of gamma rays avoiding detection, as the scanner is not in a full-ring configuration [Knopf and Lomax, 2013;

Vandenberghe et al., 2016].

To address these image-degrading effects and enhance the overall image quality, TOF information is a valuable asset. The incorporation of TOF data not only enhances spatial resolution but also proves to be instrumental in overcoming the constraints encountered in in-beam PET imaging configurations [Crespo et al., 2007].
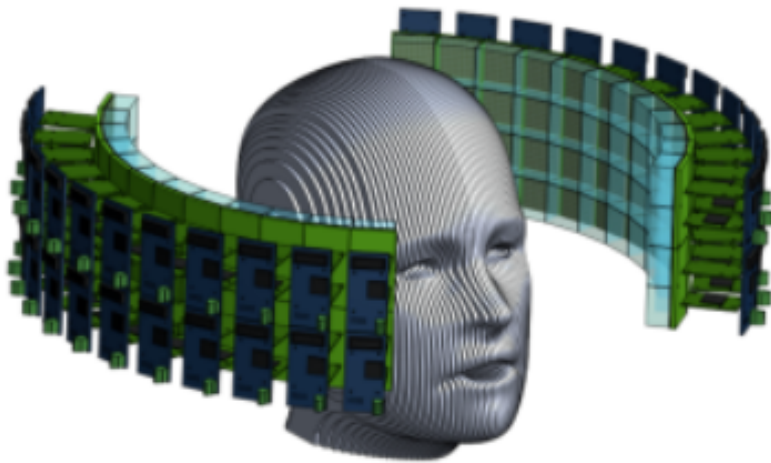
Figure 3.6: TOF-PET prototype designed and developed by the TPPT consortium. Taken from [UT Austin Portugal, 2020]

Chapter 4

Simulation Framework

With the purpose of simulating the in-beam TOF-PET prototype developed for range verification in proton therapy, LIP-Coimbra group decided to create a framework using Geant4 toolkit. Using the tools developed within this framework allows the acquisition of the activity and image reconstruction resulting from the administered radiation during a treatment plan.

This chapter describes the simulation framework created for this project, with a focus on the TPPTsim component. Besides this information, an overview regarding Monte Carlo simulations and the Geant4 toolkit is also provided.

4.1 Monte Carlo simulations

Monte Carlo simulation is a simulation technique that involves using random sampling and statistical analysis to calculate outcomes. It's particularly useful for situations where exact results are unknown. This approach involves selecting statistical distributions for input parameters and drawing random samples from these distributions to represent input values. These inputs lead to corresponding output parameters, each representing a specific scenario in the simulation. Multiple simulation runs yield various sets of output values, which are then statistically analyzed to inform decision-making. The variation in output is characterized using sampling statistics of the output parameters [Raychaudhuri, 2008].

In order to conduct a Monte Carlo simulation the following steps are necessary [Raychaudhuri, 2008]:

1) Static Model Generation: Develop a deterministic model resembling the real scenario, using most likely input parameter values and mathematical relationships to produce desired outputs.

2) Input Distribution Identification: Enhance the deterministic model by incorporating risk factors. Identify underlying distributions governing input variables using historical data and standard statistical methods.

3) Random Variable Generation: Generate random numbers from the identified distributions for input variables. These numbers constitute sets of inputs for the deterministic model, producing sets of output values.

4) Analysis and Decision Making: With output value samples from the simulation, conduct statistical analysis to gain confidence in decision-making based on simulation outcomes. This step aids in assessing potential outcomes and making informed choices.

4.2 GEANT4

Geant4, the acronym for Geometry and Tracking 4, is a versatile Monte Carlo simulation Toolkit developed at CERN in the 1990s. Originally designed for particle physics experiments like the Large Hadron Collider, it uses Object-Oriented technology to model particle interactions with matter. It was first used for High Energy Physics (HEP) experiments but expanded to other fields like space science and medical physics due to its flexibility [Guatelli et al., 2011].

Geant4 is the sole open-source Monte Carlo code for radiation physics research, covering a broad range from HEP to lower energy scales. It offers extensive capabilities for modeling both detectors and physics. Users can replicate experimental setups by defining geometries, materials, particles, and their interactions. The toolkit permites particle tracking within materials, even when electromagnetic fields are present, and facilitates the description of detector responses. Additionally, Geant4 provides interfaces that allow users to engage with their simulation applications, store outcomes in analysis objects like histograms, and utilize visualization tools and graphical user interfaces. Its success comes from its variety of physics models which include both electromagnetic and hadronic interactions of particles with matter [Guatelli et al., 2011].

In the next sub-sections the key components necessary in order to customize Geant4 simulation are described. Three of these components are user mandatory classes: detector construction, physics list and primary particle generator. Additionally there are optional classes that the user can use. The component that includes some of these classes is referred to as scoring system [Guatelli et al., 2011].

4.2.1 Detector Construction

The detector construction component focuses on the definition of the detector structure of an experimental set-up. To define its geometry three conceptual layers need to be considered [Guatelli et al., 2011]:

1) Solid

Layer used to define the shape and size of the detector

2) Logical volume

Layer used to define attributes of the detector. These attributes can include the type of material the detector is composed of, the presence of an electromagnetic field and the sensitivity.

3) Physical volume

Layer used to define the spatial position of the logical volume with respect to the inclosing mother volume (usually called *World* volume).

In order for these concepts to be implemented in the simulation they have to be constructed in the detector construction class, *G4VUserDetectorConstruction* [Guatelli et al., 2011].

4.2.2 Physics List

The idea of a physics list components originates from the recognition that Geant4 cannot provide a singular modeling algorithm that encompasses the complete energy domain, from zero to the TeV scale, to address all established processes and particles. Instead, a synthesis of concepts and approaches is commonly employed to carry out simulation tasks [Geant4, 2023].

Users have the option to create their own physics list, but Geant4 also provides pre-made physics lists for user convenience, supported by the development team. These lists are recommended for certain tasks, yet users can construct their own physics list to align with their project's requirements and preferences [Geant4, 2023].

In order for these concepts to be implemented in the simulation they have to be executed in the physics list class, *G4VUserPhysicsList* [Geant4, 2023].

4.2.3 Primary Particle Generator

Primary particle generator component is used to specify how primary particles are generated. Users can define, among others, the type of particle to be generated, its initial kinetic energy, position of generation and momentum direction [Geant4, 2023].

In order for these concepts to be implemented in the simulation they have to be executed in the primary particle generator class, *G4VUserPrimaryGeneratorAction* [Geant4, 2023].

4.2.4 Scoring system

Geant4 features a scoring system that allows the collection and analysis of simulation data. This system allows users to track and analyze the behavior of par-

ticles as they traverse through the defined geometries. Various quantities, such as energy deposition, particle trajectories, and interactions, can be recorded for analysis [Geant4, 2023].

Under this scoring system there are important optional classes, among others, such as *G4UserTrackingAction* and *G4UserSteppingAction* [Geant4, 2023].

4.2.4.1   G4UserTrackingAction

This *G4UserTrackingAction* class symbolizes the actions performed by the generated particle at the start or end point of processing one track. In order to better understand its functions an explanation of what a track is needs to be given [Geant4, 2023].

A track in Geant4 is a snapshot of a particle. It keeps the current information of the particle, such as its energy, momentum, position, and time. It also has static information about the particle, such as its mass, charge, and lifetime [Geant4, 2023].

The main methods available in the *G4UserTrackingAction* class include [Geant4, 2023]:

1) *PreUserTrackingAction*(const *G4Track**): This method is called before the tracking of each new particle starts. Using the information contained in the track the users can perform setup tasks or modify the particle's behavior before tracking begins.

2) *PostUserTrackingAction*(const *G4Track**): This method is called after the tracking of a particle is completed. Using the information contained in the track the user can perform tasks such as analyzing the particle's trajectory or recording data.

4.2.4.2   G4UserSteppingAction

The *G4UserSteppingAction* class symbolizes the actions performed by the generated particle at each end of stepping. In order to better understand its functions an explanation of what a step is needs to be given [Geant4, 2023].

A step in Geant4 is a discrete portion of the trajectory of a particle. It is defined by the two endpoints of the step, the *PreStepPoint* and the *PostStepPoint*. The *PreStepPoint* is the position and momentum of the particle before it takes a step, and the *PostStepPoint* is the position and momentum of the particle after it takes a step. The step also stores the change in track properties between the two points. These properties, such as energy and momentum, are updated as the various active processes are invoked [Geant4, 2023].

The main method available in the *G4UserSteppingAction* class is [Geant4, 2023]:

1) *UserSteppingAction*(const *G4Step**): This method is called at the end of each

particle step. Using the information contained in the step the user can perform tasks such as modifying the characteristics of a particle, data recording or check the type of interaction with matter that occurred.

4.3   TPPT framework: TPPTsim

The goal of the TPPT project is to prove the feasibility of using TOF-PET for range verification in proton therapy. To study the process of proton interactions and accurately assess the proton range within biological tissues, a framework was developed utilizing the capabilities of the Geant4 simulation toolkit.

The TPPT framework consists of three linked parts: the TPPTsim (simulator), TPPTbuilder (event builder) and TPPTcoinc (coincidence sorter). In the development of this thesis only the TPPTsim part was used, thus, more detailed information will be provided for this part in contrast with the other two.

The TPPTsim framework has two main purposes. The first one is to provide stimulation-based predictions for the spatial distributions of the activity of the positron emitting species and the dose induced by a proton beam. The second one is to conduct simulations providing data on the energy deposition in the scintillators of the TPPT TOF-PET scanner.

The TPPTbuilder main purpose is to define scintillation events, characterized by the time mark and energy, based on the data for energy deposition in the detector's scintillators obtained in TPPTsim using Geant4 simulations.

The TPPTcoinc purpose is to find coincidences in the scintillation events, constructed by TPPTbuilder using the simulation data from TPPTsim.

When considering the inner workings of the TPPTsim framework four aspects need to be considered. They are designated as Phantom, Detector composition, Source and Simulation Mode.

Phantom is an object (single or a composite one) defined in the geometry which represents the physical phantom. Detector composition defines the composition of the scanner. Source is the component responsible for generation of the primary particles. Simulation Mode defines the type of the simulation to be conducted.

An example of a simplistic simulation configuration, defining a box-shaped phantom of PMMA material, a detector consisting only of scintillators, a primary source generating 100 MeV protons isotropically from a point at (0,0,0) coordinates with the timestamp of 0 ns, and starting the Geant4 GUI as the simulation mode, is the following:

SM.Phantom = new PhantomBox(200.0*mm, 200.0*mm, 200.0*mm, EMaterial::PMMA);

SM.DetectorComposition.add(DetComp::Scintillator);

SM.SourceMode = new SourcePoint(new Proton(100.0*MeV), new ConstantTime(0), 0,0,0);

SM.SimMode = new ModeGui();

The result of running TPPTsim with this configuration will be opening of the following window:
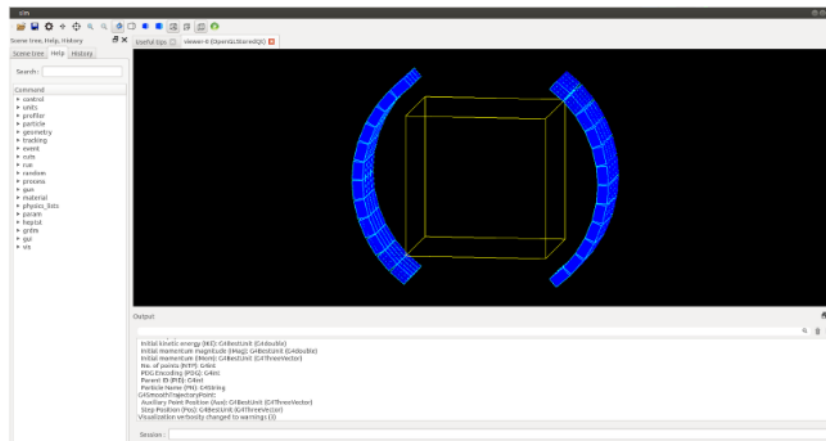
Figure 4.1: Visual window opened upon the simulation start

When the green "play" button situated at the right side of the top toolbar is pressed, the result of a Geant4 simulation of a single proton will be shown:
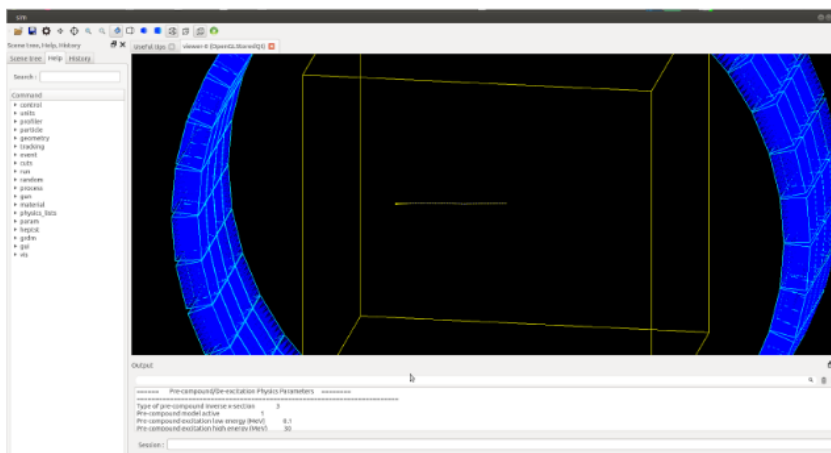
Figure 4.2: Visual window of when a proton is generated

It is important to mention that in order to conduct a simulation a phantom, source and simulation mode must always be provided. The detector composition can be omitted if the detector is not required for the selected simulation mode.

The following sections will describe the different options available in each of the four main aspects previously presented. More detailed information regarding the signature and argument explanation of each method of the four main aspects can be found in TPPTsim manual, in which i had the main contribution in writing [github, 2023].

4.3.1 Phantom

The framework offers a spectrum of choices for which phantom to use, encompassing simulation configurations:

1) Without the incorporation of a phantom.

2) With a phantom exhibiting a box-shaped geometry.

3) With a phantom featuring a cylindrical morphology.

4) With a phantom derived from CT data sourced from a DICOM file.

5) With a Derenzo phantom.

4.3.2 Detector composition

The framework offers a spectrum of choices for which detector composition to use. This includes all the components of the TPPT scanner (scintillators and support structures) as well as a special component which is required for a specific simulation mode.
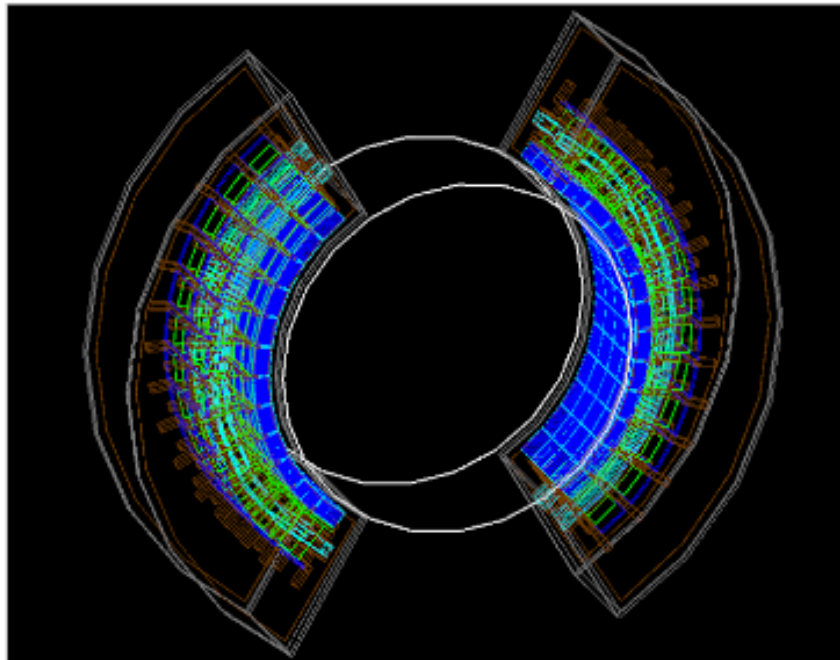
Figure 4.3: Visualization of all detector components available in the framework

1) Scintillators

This is a component that represents the TPPT scanner's scintillators.

2) Support structures

There are several components which represent different support structures of the TPPT scanner: the upper and lower base, housing, silicon photomultipliers, printed circuit boards, copper "ribs" and cooling assemblies.

   3) Particle recorder

The ParticleRecorder is a physical volume (thin-walled tube) made of air which should be added to the geometry in order to use the "ParticleLogger" simulation mode. This volume is positioned right before the scintillators.

4.3.3   Source

In Geant4, in order to start a simulation, the primary particle generator has to be configured. For each particle to be generated it needs information regarding the particle name, its kinetic energy, the xyz coordinates of the origin, the time of generation and the momentum direction.

The framework offers a spectrum of choices for which source to use. They can be divided into three groups. First are the beam-related sources, second are the sources based on output files created using the framework and third are the special sources.

   1) Beam-related sources

       a) Beamlet

This source is used to generate a parallel beam of particles. The user specifies the particle (and its energy), the time generation, the beam origin and direction. Optionally, it is possible to configure the beam profile in the plane perpendicular to the beam direction, e.g. use a beam profile where particles are uniformly generated within a rectangle and round area or according to a Gaussian distribution. If not provided (default), a pencil beam with zero width is generated. Another optional parameter is the number of particles per generation (default is 1).

       b) Multi-beamlet

This source is used to generate a multi-beamlet. Currently, the beam is configured to replicate the conditions of the beam used in the MD Anderson Cancer Center (can be changed by using a different beam calibration file) and the user only needs to specify the information related to each beamlet such as the particle (and its energy), the number of generated particles per beamlet, the time generation and the isocenter position.

   2) Source reading information from files

This type of source generates particles based on the type of file provided by the user. It can be separated into three different cases.

       a) Particles source reading from list file

Individual particles are generated according to the information provided in the specified file. For each particle, the file lists the particle name (Geant4 system),

energy (keV), xyz coordinates of the origin (mm), direction unit vector and time (ns).

b) PES source reading from histogram files

This source can be used to generate positron emitters according to the spatial distribution histograms of the activity, generated by several simulation modes (e.g. probability-based PES generation).

c) Source of gamma pairs using a histogram of the annihilation positions

This source is used to generate back-to-back gamma pairs of 0.511 MeV according to the specified histogram of the spatial distribution of the activity.

3) Special sources

In these types of sources particles direction is sampled assuming isotropic distribution and time generation is done according to the settings provided by the user.

a) Point source

The specified particle is generated at a point with the given coordinates.

b) Na22 point source

This source is used to simulate the decay of ^{22}Na isotope.

c) Line source

The specified particle is generated along a line defined by the given start and end xyz coordinates.

d) Cylindrical source

The specified particle is generated inside a cylinder-shaped region of space with the dimensions given by the user.

e) Material limited source

This source is used to generate the specified particle, uniformly inside a given spatial region (inside a bounding box) but rejecting those positions which are not occupied by a specified material.

f) LYSO natural radioactivity source

This source is used to simulate the natural radioactivity from Lu176 inside the scintillators of the TPPT scanner.

g) Source mixer

This source is used to combine more than one source in a simulation run. The user provides a list of sources and their respectful statistical weights. For generation, one of the sources is randomly selected based on the statistical weights.

4.3.4   Simulation mode

Simulation mode defines what task is to be conducted during the simulation. The simulation modes currently implemented in the framework are presented in this section.

The framework offers a spectrum of choices for which simulation mode to use, encompassing:

1) Energy deposited in scintillators

This mode is used to record energy deposition in the scintillators of the TPPT scanner. The data include the scintillator index, the deposited energy and the timestamp for each deposition.

2) Dose distribution

This simulation mode is used to record the dose (or, alternatively, the deposited energy) in a specified region of space. This region is defined by a given number of box-shaped voxels and their sizes for each direction (in X, Y and Z) and the origin position in the world.

3) PES generation using brute-force algorithm

This simulation mode generates a list of positron emitting isotopes produced inside the phantom for the configured source of primary protons using the brute-force algorithm (see chapter 5 section 5.2 for detailed explanation of this algorithm). The record for each individual isotope includes its symbol (e.g. C11 for carbon-11), XYZ position and timestamp.

4) PES generation using probability-based algorithm

This simulation mode generates the spatial distribution of the PET activity inside the phantom for the configured source of primary protons using the probability-based algorithm (see chapter 5 section 5.3 for detailed explanation of this algorithm). The spatial distribution of the PET activity data is recorded in 3D histograms for each configured PES reaction channel. Each histogram bin stores the number of observable decays (during a specified time window) in that location.

5) PET activity generation using probability-based algorithm

This simulation mode is similar to the one previously described, but with one substantial difference: instead of providing the spatial distribution of the observable activity for each reaction channel independently, this mode outputs the combined activity for all channels. More specifically, this output represents the combined PET activity induced by the treatment and observable during the specified time intervals in the given region of space.

6) Positron annihilation positions

This simulation mode is used to collect spatial distribution of the positron annihilation positions in a specified region of space. The user configures the 3D binning for the region of interest. Each bin represents the number of annihilated positrons in that location.

7) Visualization mode

This mode is used to draw the detector's geometry using the Qt-based visualization tool provided by Geant4. It can also be used to show the tracks resulting from a simulation run with one call of the configured source of the primaries.

8) Particle tracing

This simulation mode can be used to perform different tests of the detector geometry by configuring a source of test particles ("geantino") with a fixed direction and then observing the log of the trajectory of the particle. The mode automatically starts the Geant4's visualization tool.

9) Particle logger

This simulation mode can be used to split time-consuming simulations in stages. It allows storing information on the particles which arrive at the special geometric volume "ParticleLogger" in a file. The information consists of the full particle name, energy, position and direction. After saving the information for a particle to the file, tracking for that particle is stopped.

Chapter 5

Computational Approaches for PES Generation Modeling

As already seen, the TPPT framework has different tools that enable the emulation of proton therapy treatment. One of these tools is to generate the spatial distribution of PES generated during the interaction of protons with matter. This chapter explores the diverse approaches within TPPT dedicated to achieving the spatial characterization of PES distributions.

The TPPT research group has developed four approaches to predict the spatial and temporal distributions of the positron-emitting activity generated in biological tissues in response of their exposure to the proton beam:

- Direct Geant4 simulation with a reference physics list

- Monte Carlo simulation with a custom PES generator:

    - brute-force algorithm
    - probability-based algorithm

- A fast algorithm which does not rely on Monte Carlo simulations

Due to the substantial significance of the fourth approach in this work, the fast algorithm will be discussed in a separate chapter.

5.1 Direct Geant4 simulation with a reference physics list

Geant4 has several alternative models that the user can choose from depending on the type of interactions which matter for a particular task. A collection of such models is referred to as a physics list. In this case where the intention is to study the interactions that occur using proton beams the physics lists recommended are those which in their name include "BERT" (stands for Bertini Cascade model), or

"BIC" (Binary cascade model). For example, the physics list QGSP_BIC_HP could be used. This physics list uses four Geant4 models. It utilizes the Quark gluon string model (QGS), the low energy parametrization mode (LEP), the Binary Cascade model (BIC) and the High Precision Neutron Model (HP) [Banerjee et al., 2011; Wright and Incerti, 2009].

To assess predictive power of these internal models, a simulation test was conducted to extract the effective cross-sections for ^{11}C and ^{10}C production from ^{12}C in response to proton beam irradiation for all major reference physics lists of Geant4. These cross-sectional results were then compared to experimental ones available in [Horst et al., 2019].

Among the tested physics lists the best results were obtained when using QGSP_BIC_HP physics list (Figure 5.1).

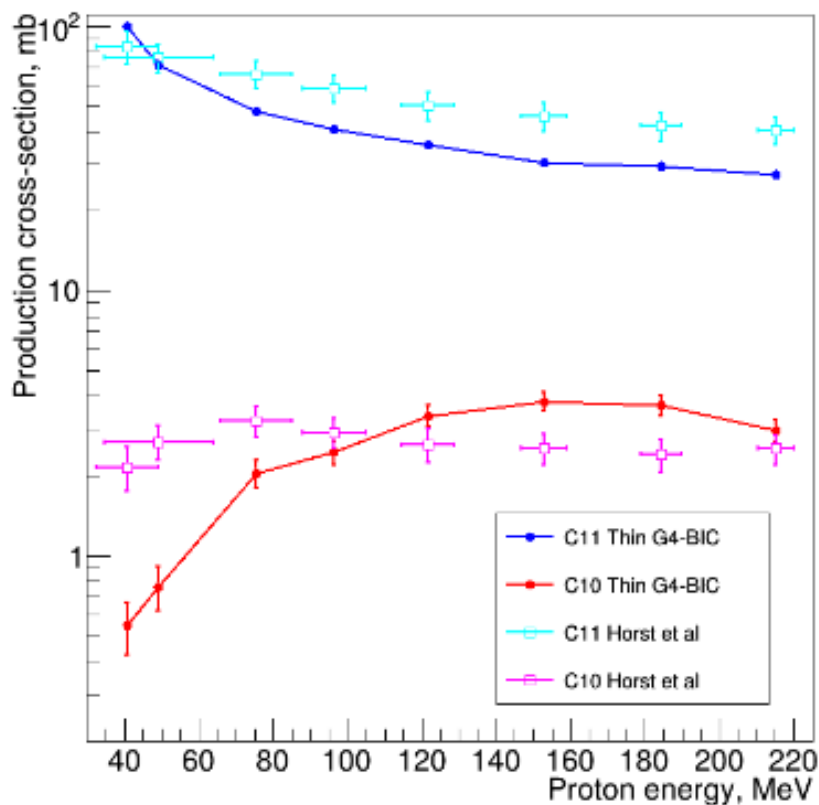Figure 5.1: Comparison between the effective cross-sections obtained using the QGSP_BIC_HP physics list and cross-sections experimental results of both ^{10}C and ^{11}C

Despite exhibiting results close to the experimental ones, QGSP_BIC_HP physics list is still a bad match to the measured cross-sections [Banerjee et al., 2011].

As a result, a more accurate approach is required to simulate PES production in proton beams.

5.2 Monte Carlo simulation with a custom PES generator

This Monte Carlo approach makes use of Geant4 particle tracking to follow the trajectory and energy of generated protons, but instead of tracking the entirety of the consequent particles, all secondary particles produced are eliminated (not tracked) and only the tracking of primary protons is kept. In the PES production phase, this approach disregards the Geant4 internal models and introduces a custom Monte Carlo procedure using the production cross-sections for a specific set of proton induced reactions. Therefore, the relevant PES produced in human tissue needs to be identified.

The study to establish the relevant PES and their generation cross-sections was conducted by the Heidelberg Ion-Beam Therapy Center (HIT) group and their results were published in [Bauer et al., 2013]. The HIT group concluded that for an offline PET scanner there are six main production channels that contribute to the activity (Table 5.1).

Nuclear reaction channel	Radionuclide half-time (s)
12C(p,pn)11C	$T_{1/2}(^{11}C) = 1222.8$
16O(p, 3p3n)11C	$T_{1/2}(^{11}C) = 1222.8$
16O(p, pn)15O	$T_{1/2}(^{15}O) = 597.6$
16O(p, 2p2n)13N	$T_{1/2}(^{13}N) = 122.4$
40Ca(p, 2pn)38K	$T_{1/2}(^{38}K) = 456.0$
31P(p,pn)P30	$T_{1/2}(^{30}P) = 150.0$

Table 5.1: Six main production channels that contribute to the activity in offline PET and their radionuclides half-times

Information regarding 31P(p,pn)P30 reaction is not present in the article above, but when contacted by our group in order to get the cross-section data the HIT group also provided information regarding this reaction.

To obtain the cross-section data of the PES shown in Table 5.1, the HIT group employed a process of "tuning" to the cross-sectional data so that simulated PES activity corresponds to the activity measured experimentally in their facilities. The group accomplished this tuning process as follows: the simulated activity depth profiles of a specific radionuclide were compared with the actual activity distributions observed experimentally with a PET scanner for each separate radionuclide. Through iterative adjustments to the cross-section data, they systematically minimized the differences between the two types of activity. This encompassed the cycle of modifying the cross-section data, re-running the experiment simulations, and once more comparing the results against the measurements until they matched well.

The cross-section data were then extracted from the graphs presented in the published article. Information regarding the 31P(p,pn)P30 reaction was found in the Experimental Nuclear Reaction Data database. The final result of this process can be found in the following figure:
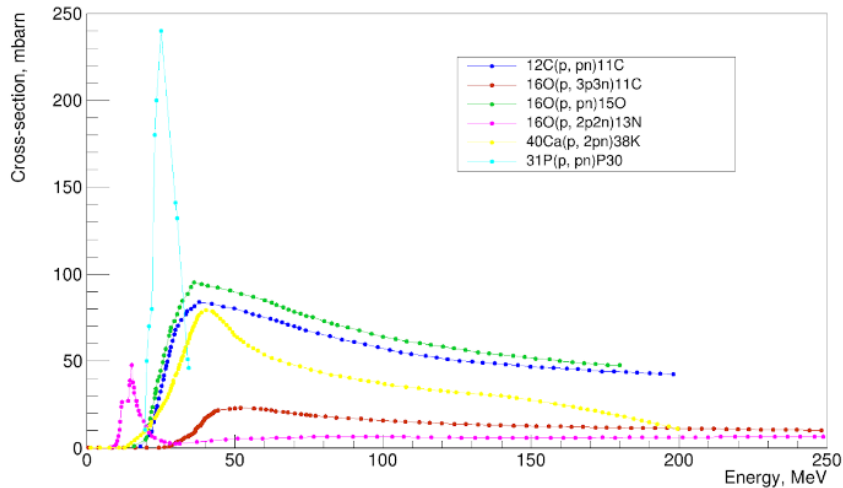

Figure 5.2: "Tuned" cross-sections of the 6 main production channels in human tissue as a function of proton energy

More information regarding the extraction of the cross-section data can be found in the thesis written by Margarida Nunes Simões, a master's student who was affiliated with the LIP-Coimbra group the previous year [Simões, 2022].

This Monte Carlo approach is divided into two algorithms depending on the method used to generate PES. They are the brute-force and probability-based algorithms. Each of these algorithms will be described in the following subsections.

5.2.1 Brute-force algorithm

The brute-force algorithm is used to generate a list of positron emitting isotopes inside the phantom when irradiated by a proton beam. For each generated PES it records which radionuclide is produced, its coordinates and timestamp of origin.

This algorithm starts by automatically loading the cross-section data and then the generation procedure is configured for all materials defined in the simulation. During each Geant4's tracking step of the primary proton, the probability for all possible generation channels is calculated, and using a random number generator, a potentially triggered channel is selected and the trigger step is computed for the current material. If this step is shorter than the proton's step given by Geant4, the positron emitter is generated at the corresponding position and the timestamp is attributed (the mean value of the timestamp of the proton at the beginning and the end of the current step).

To validate this algorithm, the activity obtained using the brute-force algorithm

was compared to literature data obtained in [Bauer et al., 2013]. The experiment was conducted using a PMMA phantom and protons were generated with 125.67 MeV.
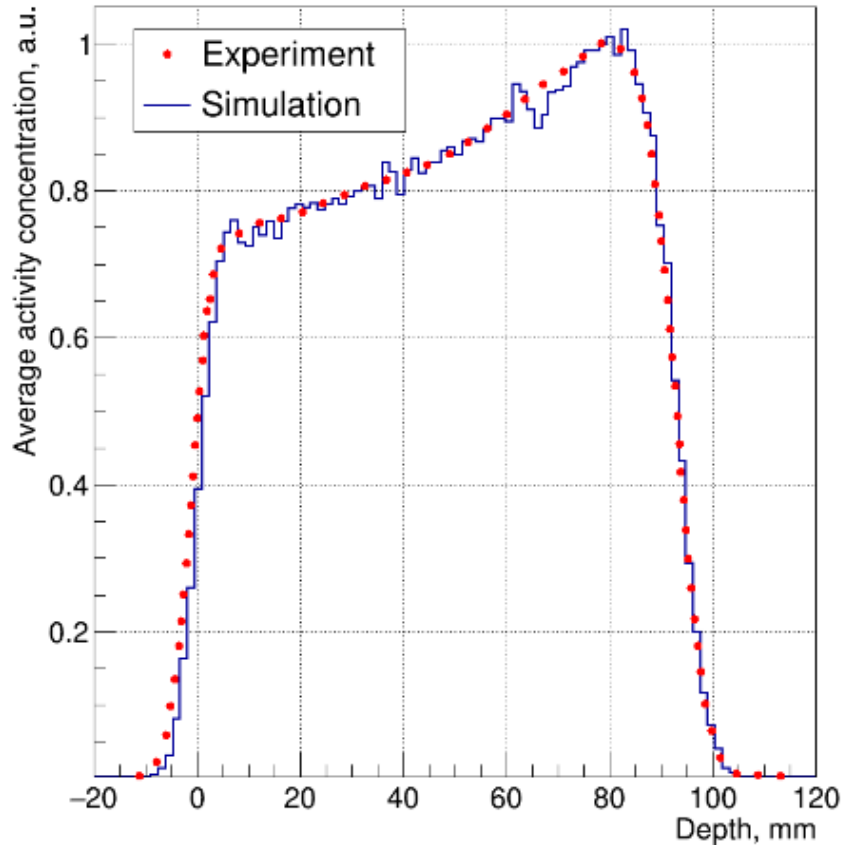
Figure 5.3: Comparison between the average activity concentration given by the brute-force algorithm and experiment data in a PMMA phantom

As it can be seen from Figure 5.3, the results given by the brute-force algorithm match well with the experimental results. Hence, these findings can be utilized to demonstrate the efficacy of the algorithm's approach in generating activity resulting from proton beam irradiation.

The development of this algorithm was driven by its intended application in medical settings. As a result, a simulation was carried out, utilizing the brute-force algorithm, and it was based on the treatment plan established at the MD Anderson Cancer Center. In this context, the objective was to determine the total number of produced PES within a PMMA phantom. To achieve this, a source that mimicked the characteristics of the beam utilized at the MD Anderson Cancer Center was used. Henceforth, in this thesis, this source will be denoted as the *MDA beam*. Specifically, 10^8 protons were used which is the average number used per beamlet in the treatment plan. Under these conditions, the following results were obtained:

Figure 5.4: Total number of produced PES obtained using the brute-force algorithm in a PMMA phantom using the MDA beam

The disadvantage of using this algorithm is the amount of time it takes to complete the simulation. The previous results (Figure 5.4) were obtained when only on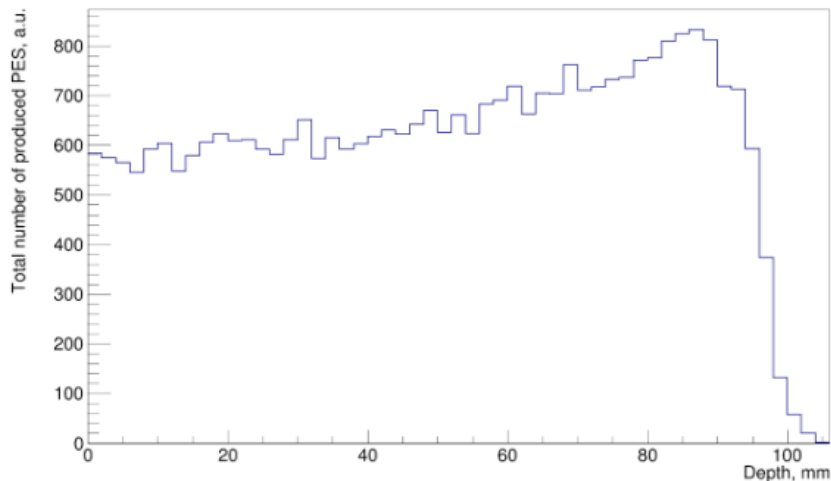e of the treatment beamlets was considered, and it took approximately 12 hours to complete the simulation when using one thread. Thus, when considering the entire treatment, which consists of approximately 1000 beamlets, the time required would be prohibitively long. This process can be accelerated by using a computer cluster, but considering that multiple cases of usage may be required per day and the cluster's resources may be in demand for other purposes, it renders this algorithm unsuitable for practical use. For this reason, a faster algorithm is needed in order to obtain the production of PES in proton beams.

5.2.2 Probability-based algorithm

The probability-based algorithm is used to generate the spatial distribution of the PET activity, avoiding as much as possible the statistical uncertainties in the position distribution characteristic of full Monte Carlo-based approaches. So this algorithm uses a probabilistic approach: during each tracking step of the primary proton, the probabilities of PES generation for each of the configured reaction channels are accumulated directly.

The region of space where the activity is to be measured is divided into 3D voxels. The time interval when the PET scanner will acquire the coincidence events is also considered. As with the brute-force algorithm, only the primary protons are tracked and the custom production cross-sections are used. For each step, the crossed voxels (and the corresponding material) are identified and the trajectory length inside each of them is established. Using the production cross-sections, the probability of generation of each PES is calculated. For each PES channel, using the proton's timestamp (assuming to give directly the isotope production time) and the half-life of the corresponding isotope, the expected contribution to the PET activity is computed and added to the corresponding voxel of the spatial

histogram for that PES channel.

This algorithm allows using a significantly smaller number of primary protons to generate activity spatial profiles of a comparable quality (low level of statistical fluctuations) in comparison to the brute-force algorithm. Thus, instead of using 10^8 protons like in the brute-force algorithm, with the probability algorithm, a similar activity curve can be obtained with the use of 10^5 protons (Figure 5.5). This greatly decreases the simulation's running time. Considering a PMMA phantom, the probability-based approach is faster by three orders of magnitude.
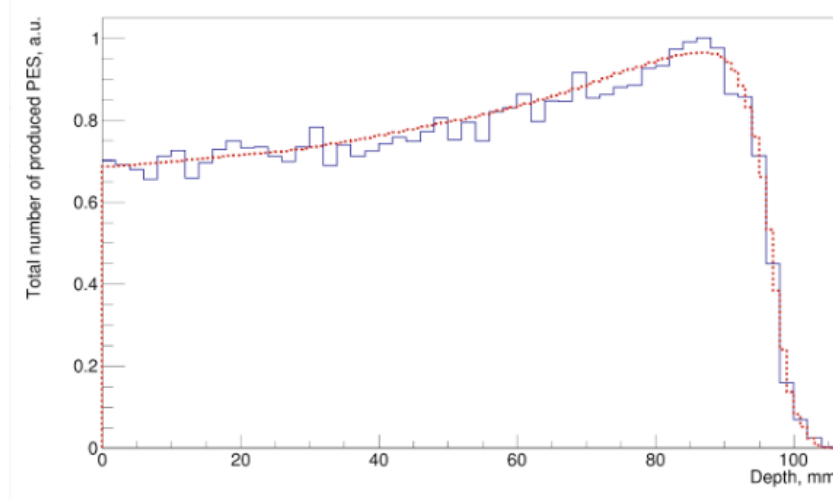

Figure 5.5: Normalized comparison of the total number of PES produced using the brute-force algorithm (blue curve) and probability-based algorithm (red curve) in a PMMA phantom using the MDA beam

The main disadvantage of using this algorithm is that the output it generates does not record the timestamp of each produced PES. Thus, if later simulations are required to reconstruct PES activity, there is no time information of PES decay, which makes the reconstruction process challenging. Another important detail is the position where PES are produced, which, as previously explained, is not stored as the exact position where the process of creation occurs but in the voxel where it occurs. As a result, the resolution for the spatial distributions obtained with this algorithm may be degraded in comparison with the brute-force one if not adequately-small size of the voxel is considered. In this work the size chosen for the voxel is 1 x 1 x 1 mm. This is sufficiently small since the PET scanner crystal size utilized by the TPPT consortium is 3 mm [Abouzahr et al., 2023] and the spatial resolution of PET reconstructions is expected to be above 3 mm [CMG, 2018].

Although the simulation run time is much faster than for the brute-force algorithm, when considering its practical use in a medical environment, where multiple cases of usage may be required per day and the phantom considered is not as simple (anthropomorphic phantom), the time required to obtain the treatment's activity needs to be faster. As a result, a new algorithm is necessary to optimise the process of obtaining PES spatial distribution.

Chapter 6

Effect of the Positron Range on the Activity induced in Brain and Bone

As previously discussed in Chapter 4, the TPPTsim part within the framework serves as a valuable tool for conducting simulations that provide data on the energy deposition in the scintillators of the TPPT TOF-PET scanner. This information can be obtained through the utilization of either the brute-force algorithm or the probability-based algorithm.

This chapter focuses on the probability-based algorithm for generating PES and elaborates on the methodology used to simulate positron emissions originating from these PES within the cranium region.

6.1 Study of positrons emitted by PES with different energies

When considering a tumor in the cranium, it is necessary to examine three distinct scenarios. The tumor can be located either in the brain or inside the bones. In the case of the brain, two different options have to be considered depending on the closeness to the bone. This distinction is due to the effects of PES, Potassium (^{38}K) and Phosphorus (^{30}P), which are mostly created when the protons interact with the bone. The positron emitted by these PES can have a range of up to 10 mm in bone. Due to the high energy with which these positrons are created, they can travel from the bone to the brain which may then affect the activity near the interface between the brain and the bone. In this section, the impact of positrons emitted by *long-range PES*, ^{38}K and ^{30}P, has to be studied in these three scenarios. In the simulation, *short-range PES*, ^{11}C, ^{15}O and ^{13}N, a type of PES that when decayed emit positrons with a short range, will also be taken into consideration.

Before beginning the simulation, some considerations regarding the generation of ^{38}K and ^{30}P can be made. Calcium (Ca) and Phosphorus (P), the elements that produce ^{38}K and ^{30}P, respectively, have a significant molar fraction in bone, and their cross-section cannot be ignored near the Bragg peak (Figure 5.2 of chapter

5). These conditions already point to the potential importance of these isotopes.

To achieve the intended results, the MDA beam with 10^5 protons will be shot into different phantoms that emulate the three different scenarios previously presented. These results are obtained using the probability-based algorithm. The phantoms used have a box-shaped geometry with 200 mm sides and are divided into voxels of 1x1x1 mm^3 size. The materials used to represent the brain and bone are G4_BRAIN_ICRP and G4_BONE_CORTICAL_ICRP, respectively. The major difference between both is that the bone has a higher molar fraction of Ca (22.5%) and P (10.3%), whereas the brain only has P with a molar fraction of 0.4%. In order to get information on the importance of the intended positrons in these simulation conditions, only the tracking of primary protons, long-range and short-range PES and their emitted positrons is performed.

During the simulation, when using the probability-based algorithm, there is a need to generate PES using the respective source. However this source has two ways of creating these particles over the voxel. Option 1 will be to generate the PES at the voxel center (Center Voxel), whereas option 2 will be to generate them randomly inside the voxel(Uniform Distribution). Therefore, the results obtained with both methods are compared in order to choose which one is to be used in the following studies.

Regarding the dual nature of PES generation, the following results were obtained for a phantom made entirely of brain:

1) 1D spatial distribution

Figure 6.1: Comparison of the 1D spatial distributions of the positrons annihilation positions using Center Voxel (blue curve) and Uniform Distribution (red curve) methods for the brain phantom
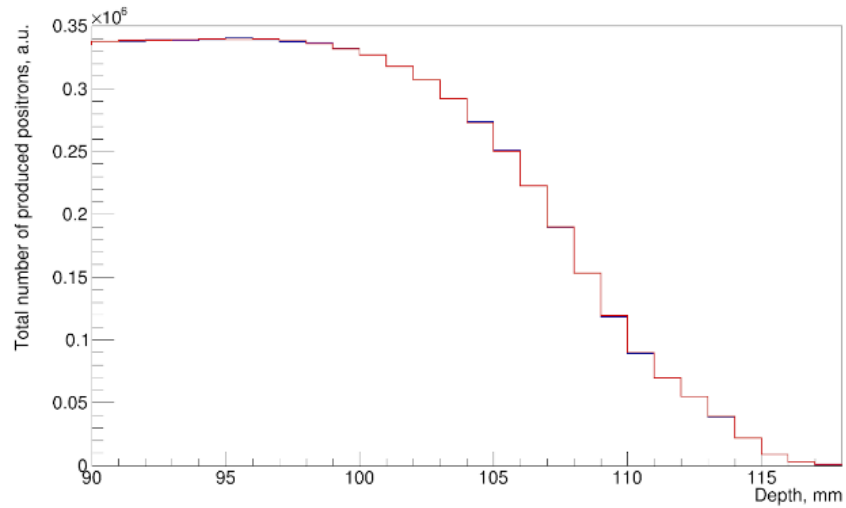
Figure 6.2: Comparison of the 1D spatial distributions of the positrons annihilation positions using Center Voxel (blue curve) and Uniform Distribution (red curve) methods for the brain phantom zoomed at distal edge

In figures 6.1 and 6.2, a distribution of the annihilation positions of all positrons emitted by all PES is shown along the beam in 1D using the both method of PES generation in the voxels. It is clear that the curves for the two approaches are essentially the same.

2) 2D spatial distribution
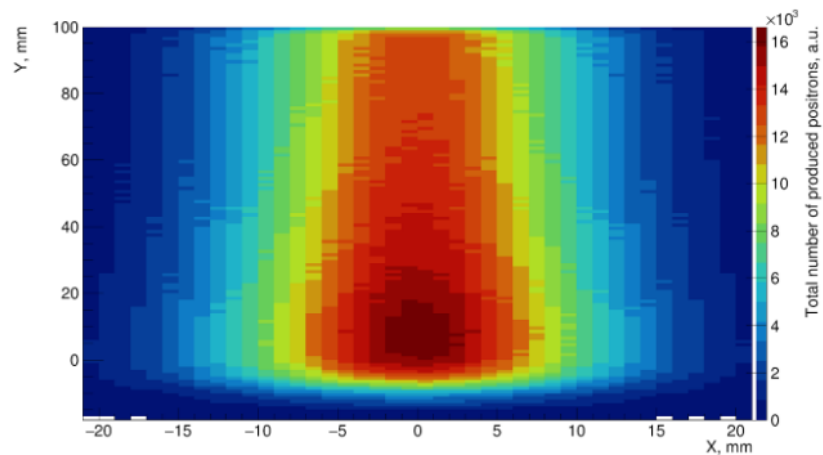
Figure 6.3: Projection of the 2D spatial distribution of positrons annihilation positions using Center Voxel method for a brain phantom
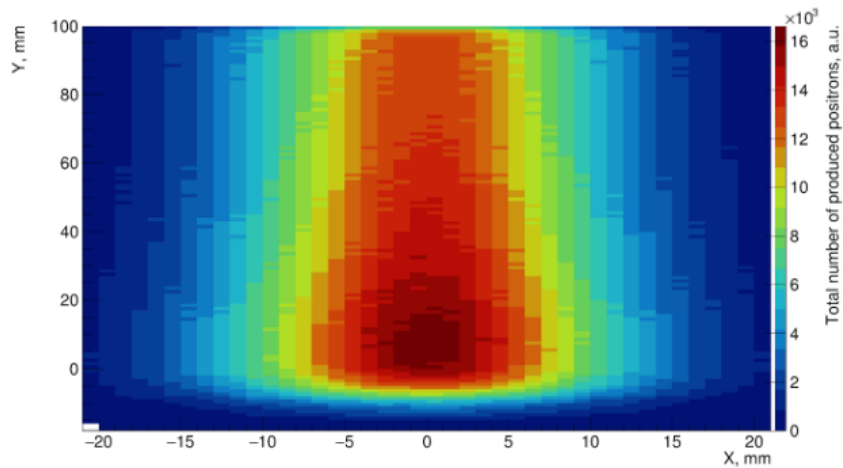
Figure 6.4: Projection of the 2D spatial distribution of positrons annihilation positions using Uniform Distribution method for a brain phantom

In Figures 6.3 and 6.4, the projection of the 2D spatial distribution of positrons annihilation positions is shown. When comparing slices near the peak region of both plots (Figure 6.5), it is clear that the positrons behave in the same way since their curves match well.
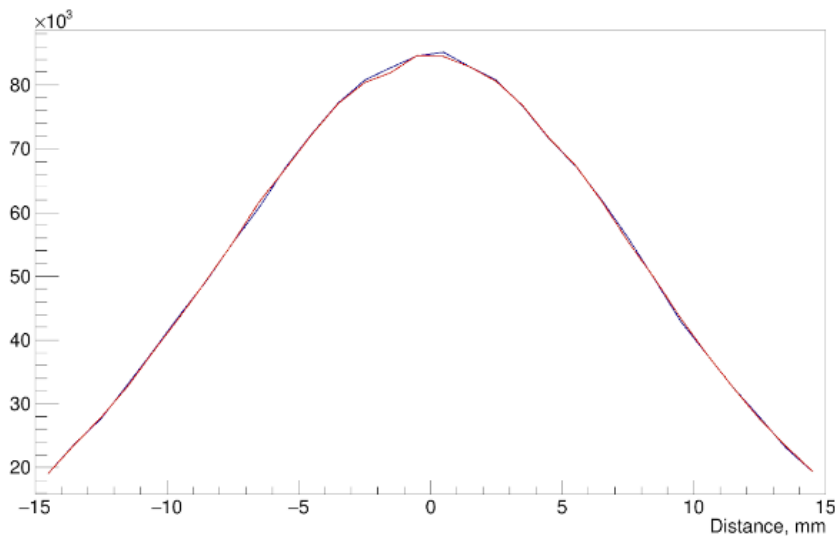
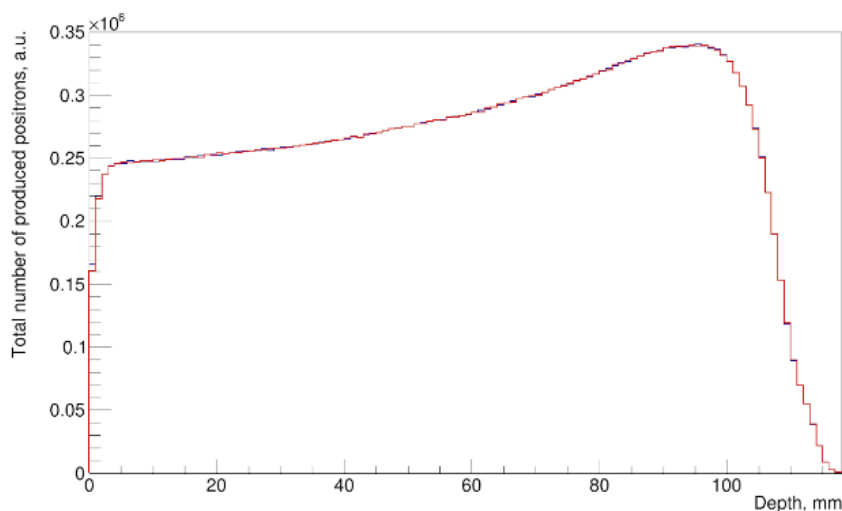Figure 6.5: Slice near the peak region of the projection of the 2D spatial distribution of positrons annihilation positions using Center Voxel (blue curve) and Uniform Distribution (read curve) method for a brain phantom

Based on these results, it can be concluded that applying either of the methods is equivalent because they produce essentially the same results, so the center voxel method was chosen in the following study due to slightly lower computation costs. Similar results were obtained when considering a phantom made of bone, therefore, in these conditions, the same conclusion can be drawn.

It should be noted that statistical fluctuations are negligible for both these and

the following results. For each condition, the results were independently verified with different simulation seeds, and the observed behavior was preserved.

Now that the PES generation method has been confirmed the three study cases will be discussed in detail.

6.1.1   Bone

A phantom entirely made of G4_BONE_CORTICAL_ICRP is used to simulate the bone region where a tumor can be formed.

The first result of the situation is a plot of the 1D spatial distribution of the total number of produced PES for both long-range and short-range PES when using the MDA beam.
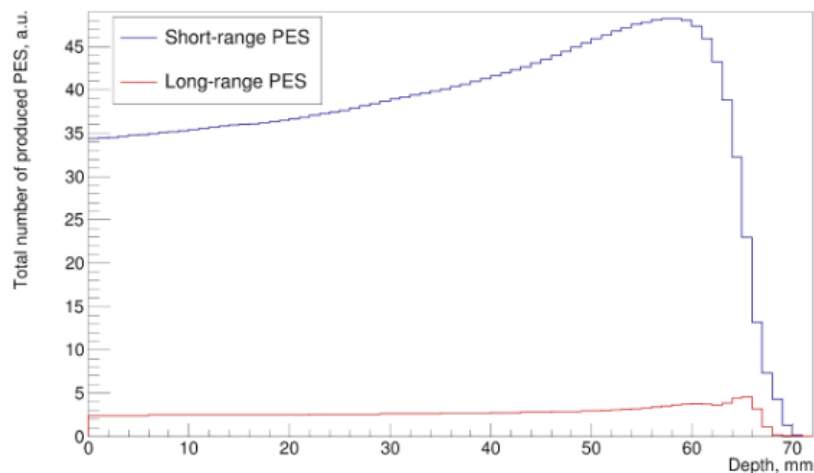
Figure 6.6: Spatial distribution of the total number of produced PES in the brain phantom along the beam direction

Regarding the creation of both types of PES in the bone, it is clear that the effect of long-range PES cannot be overlooked, as their activity is approximately 10% of that of the short-range PES.

The distributions along the beam direction for the total number of the produced PES as well as the positron annihilations are shown in Figures 6.7 and 6.8.
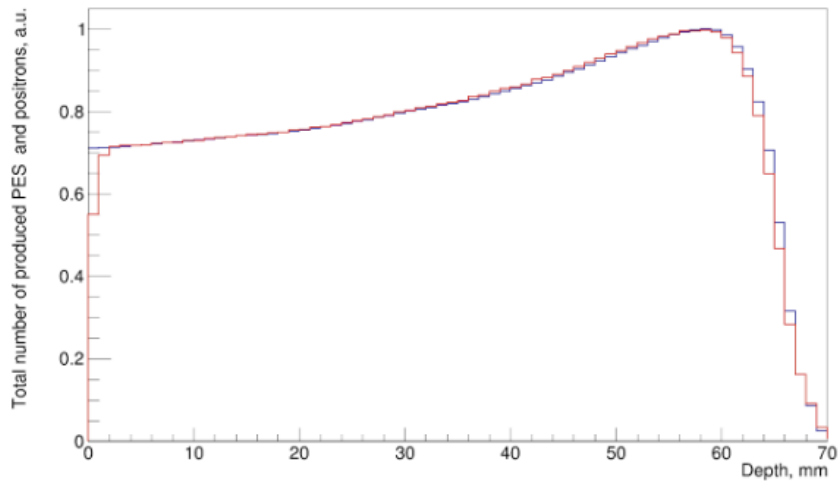
Figure 6.7: Comparison between the 1D spatial distribution of the total number of produced PES positions (blue curve) and their emitted positrons annihilation positions (red curve) in bone phantom along the beam direction

Figure 6.8: Comparison between the spatial distribution of the total number of produced PES positions (blue curve) and their emitted positrons annihilation positions (red curve) in bone phantom along the beam direction zoomed at distal edge

Looking at the graph, it can be seen that although both curves are rather similar along the beam, when considering the distal edge position, the discrepancy between both curves is significant. At a depth of 65.5 mm, this discrepancy can reach levels of approximately 10%. This observation leads to the conclusion that the positron range cannot be disregarded in the bone.

6.1.2 Inner brain

A phantom entirely made of G4_BRAIN_ICRP is used to simulate the brain region where a tumor can be formed and considering the scenario where activity is

not affected by the positrons created in the bones.

The first result of the situation is a plot with a 2D distribution of the total number of produced PES positions for both short-range PES (Figure 6.9) and long-range PES (Figure 6.10). To facilitate comparison, Figure 6.11 shows the long-term PES graph was scaled to the same color scale maximum as the short-term PES graph.
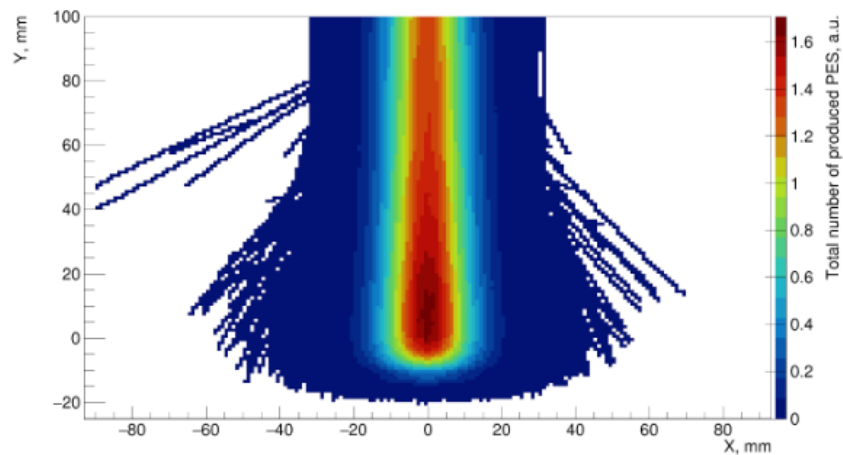
Figure 6.9: Projection of the 2D spatial distribution of the total number of produced short-range PES in brain tissue using the MDA beam
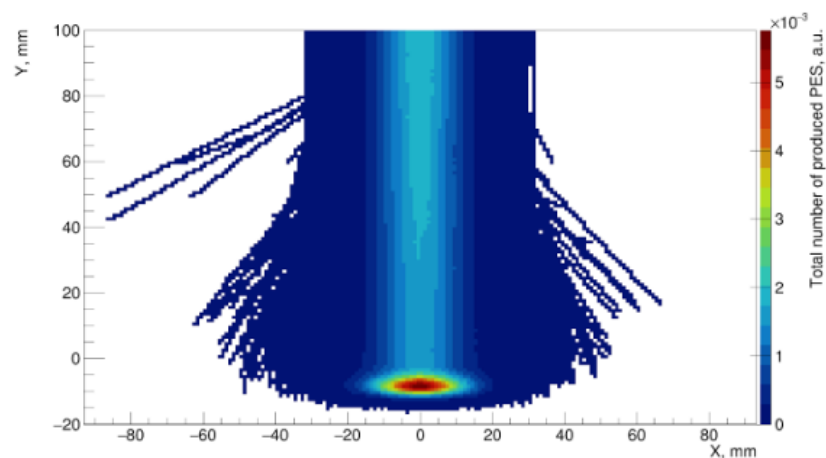
Figure 6.10: Projection of the 2D spatial distribution of the total number of produced long-range PES in brain tissue using the MDA beam
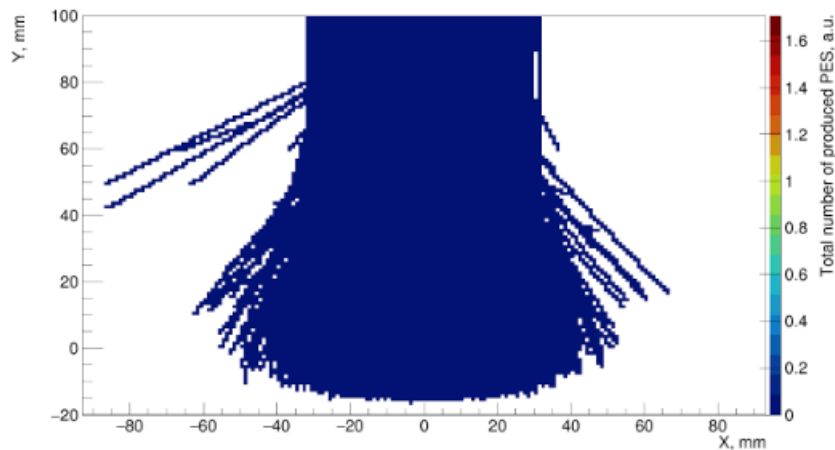
Figure 6.11: Projection of the 2D spatial distribution of the total number of produced long-range PES in brain tissue using the MDA beam in a same color scale maximum as Figure 6.9

When both distributions are considered, it is clear that the long-range PES activity (Figure 6.11) is insignificant when compared to the short-range PES activity (Figure 6.9). This is supported by the original graph of the long-range PES activity (Figure 6.10), whose scale is three orders of magnitude lower than that of short-range PES activity (Figure 6.9). This is to be expected given that the material used to represent the brain contains very little phosphorus and no calcium.

The distributions along the beam direction for the total number of produced PES as well as for the positron annihilations are shown in Figures 6.12 and 6.13)
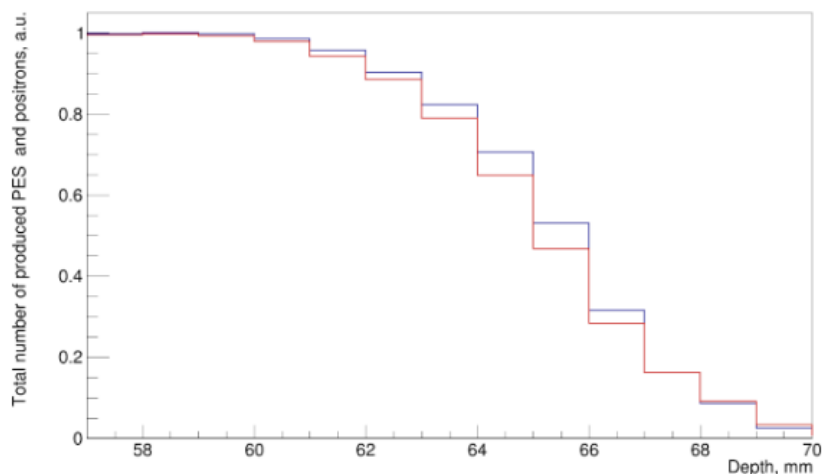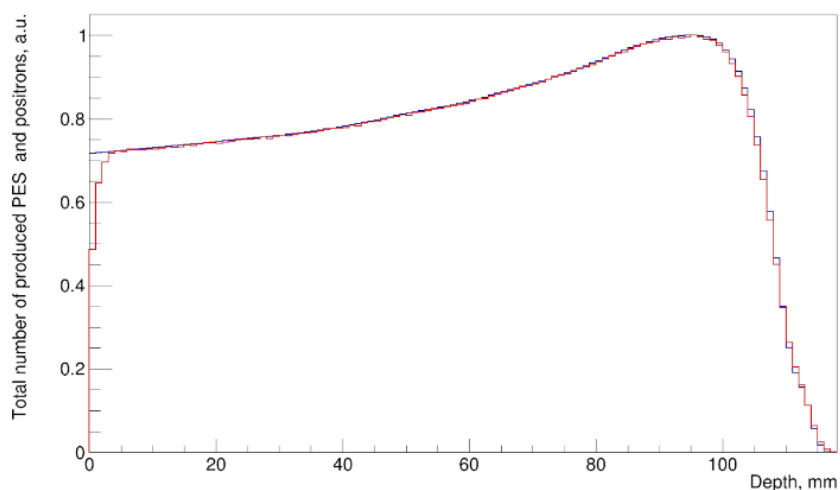

Figure 6.12: Comparison between the 1D distribution of the total number of produced PES position (blue curve) and their emitted positrons annihilation position (red curve) in brain tissue using the MDA beam
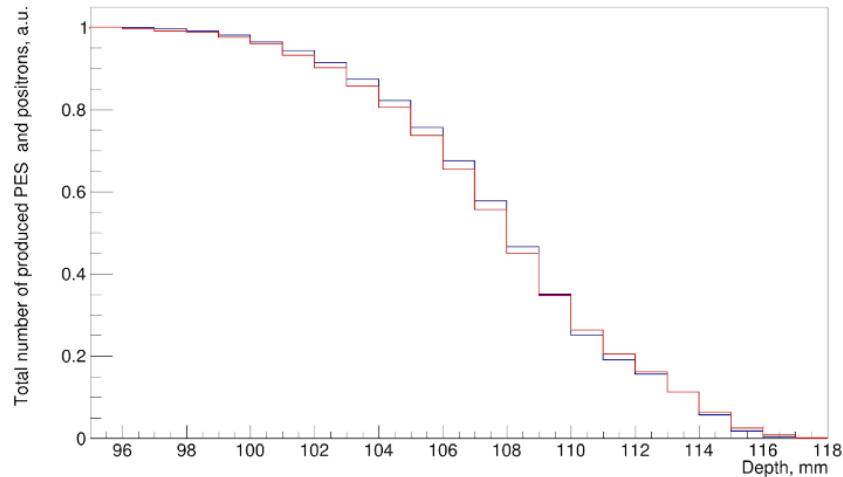
Figure 6.13: Comparison between the 1D distribution of the total number of produced PES position (blue curve) and their emitted positrons annihilation position (red curve) in brain tissue using the MDA beam zoomed at distal edge

It can be seen that the behavior of both curves is similar along the beam, and that when we consider the results at the distal edge, although there is some difference between them, it is minor enough to ignore. In the brain, this discrepancy has a maximum of approximately 3.5%. This difference, when compared to the case of the bone phantom, is due to the fact that the proportion between the long-range PES and the short-range PES in the brain is much smaller than in the bone (Figure 6.6). This observation leads to the inference that the positron range exerts minimal influence on the brain.

6.1.3   Brain close to the interface to bone

A phantom with a region made of G4_BRAIN_ICRP and another made of G4_BONE_-CORTICAL_ICRP is used to simulate the situation where a tumor is formed in the brain and the activity generated by a proton beam irradiation could be affected due to its proximity with the bone. A drawing was created to illustrate how the regions were positioned (Figure 6.14).
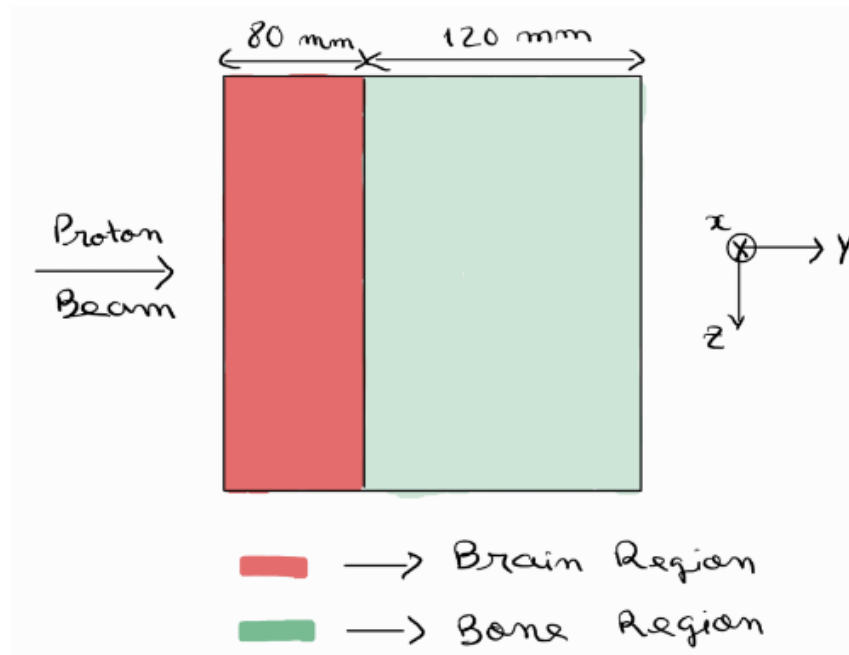
Figure 6.14: Illustration of the phantom with bone and brain region

The objective of this study is to investigate the potential migration of positrons emitted by long-range PES in bone towards the brain region. This analysis is imperative as these positrons possess higher energy levels compared to those emitted by short-range PES, enabling them to traverse longer distances. To evaluate this phenomenon, a graphical representation illustrating the distance, in relation to the bone-brain interface, traveled by positrons that successfully reach the brain region before undergoing annihilation was created (Figure 6.15).
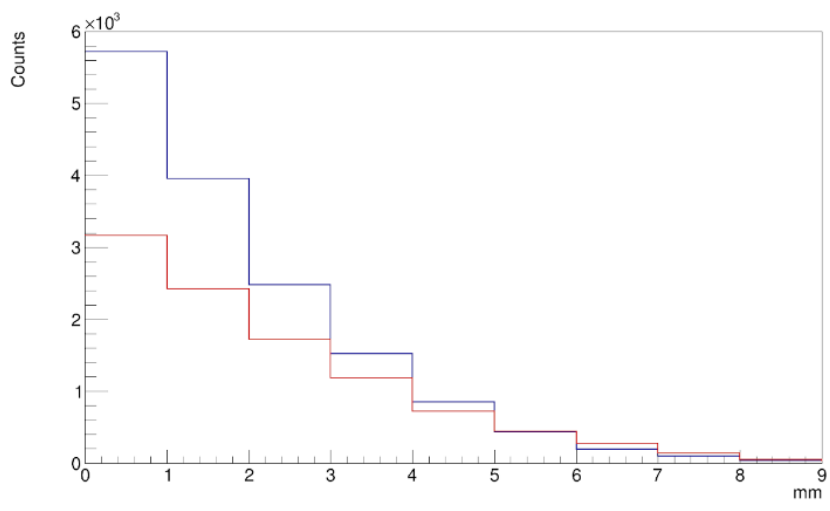
Figure 6.15: Distance between the annihilation position of positrons emitted by ^{30}P (red curve) and ^{38}K (blue curve) and the interface between the brain and bone regions

It can be seen that for both isotopes (^{30}P and ^{38}K), there are some positrons that

manage to travel from the bone to the brain region, but the majority of them are annihilated near the interface. To verify if this number of positrons can have an effect on the activity produced in the brain, their number will be compared to those of the positrons emitted by short-range PES (Figure 6.16).
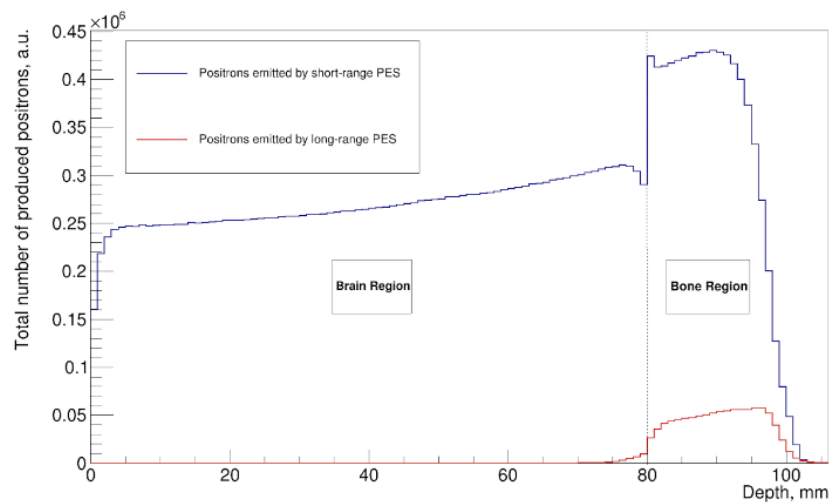
Figure 6.16: 1D distribution of positrons annihilation position in both brain and bone regions using the MDA beam

Figure 6.16 indicates that, in this study scenario, even though protons travel through the brain region before entering the bone region, the ratio between both types of positrons in the bone remains consistent with what was observed in a phantom composed entirely of bone. Specifically, long-range PES positrons comprise nearly 10 percent of short-range PES positrons (Figure 6.6).

To accurately assess the contribution of both types of positrons near the interface in the brain region, the ratio between the number of positrons emitted by short-range and long-range PES was compared (Figure 6.17).
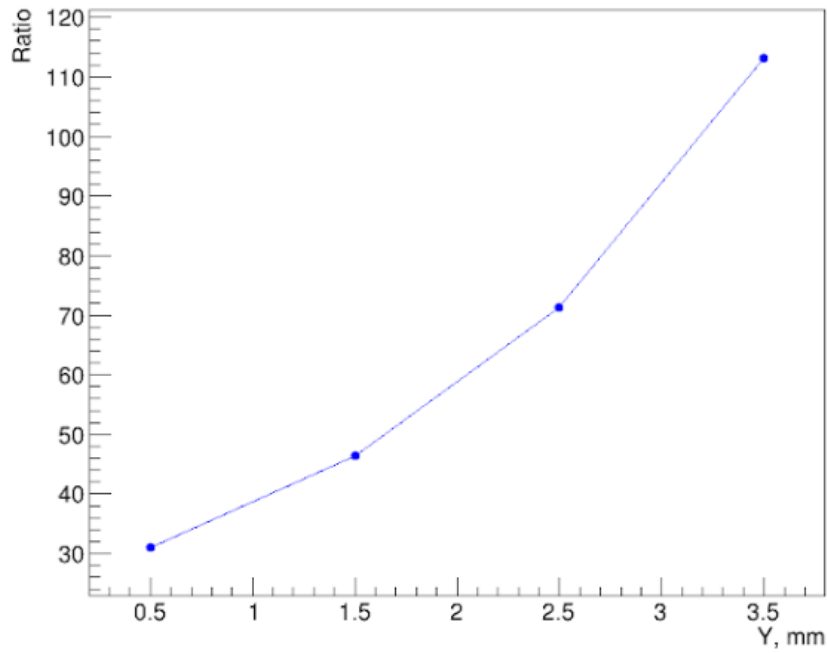
Figure 6.17: Ratio between positrons emitted by the short-range and long-range PES in the brain. Distance is given in relation to the bone-brain interface

Since the ratio near the interface is already as high as 30 and then keeps on increasing, it can be said that positrons emitted by long-range PES from bone do not affect the overall positron activity in the brain.
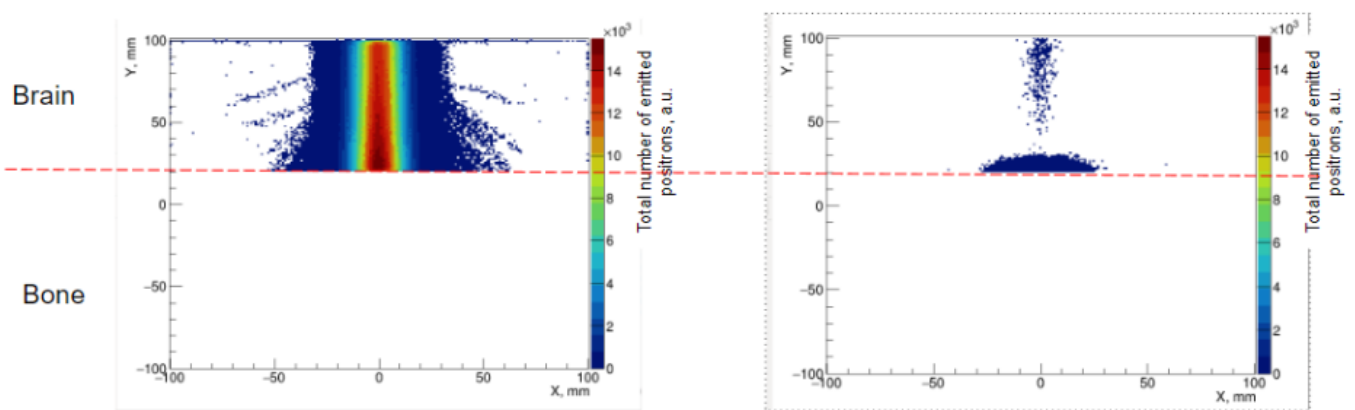
Figure 6.18: Projection of the 2D distribution of the annihilation position of positrons emitted by short-range PES (left graph) and long-range PES (right graph) in the brain region using the MDA beam in the same color scale maximum
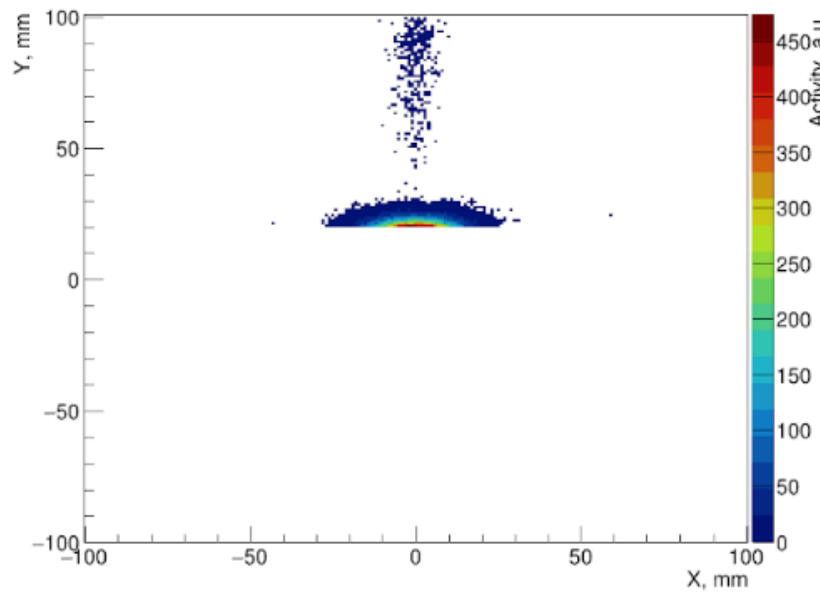
Figure 6.19: Projection of the 2D distribution of the annihilation position of positrons emitted by long-range PES in the brain region using the MDA beam in the original scale

Considering the 2D distributions of the positron annihilation positions (Figure 6.18 and Figure 6.19), it can be concluded that although there are positrons emitted by long-range PES in the brain (Figure 6.18 - right graph and Figure 6.19), their contribution to the activity is negligible when compared to that of the short-range PES positrons (Figure 6.18 - left graph). With this additional information, it is possible to state that positrons emitted by long-term PES in the bone have a small impact on the activity of the brain.

The results above were obtained for a broad range of the protons energies and in all those whose energy was high enough to arrive in the bone region, the same behavior, where the effect of positrons emitted by long-range PES is negligible, was observed.

In conclusion, the results discussed in this chapter demonstrate that the influence of positron range is minimal in all investigated scenarios, except for the bone phantom case. Therefore, when conducting simulations for PET image reconstruction involving bone, it becomes evident that the positron tracking phase holds significant importance and cannot be overlooked.

Chapter 7

Fast Algorithm

As discussed in chapter 5, owing to the high computation costs of the Monte Carlo based algorithms, a faster algorithm needs to be developed to obtain the spatial distribution of the produced PES in a designated region of space. The main idea to speed up the computations is to completely avoid tracking of individual protons inside the phantom and to use instead pre-computed data related to proton transport in the form of look-up tables (LUT).

7.1 Overview of the approach

To model the spatial distribution of PES, the fast algorithm simplifies proton motion within the phantom. Initially, protons are grouped into distinct voxels based on their generation positions. This way, some voxels may not contain any protons, whereas others may contain multiple protons. Additionally, this organization treats all protons within each voxel as a single entity. Furthermore, any lateral straggling of protons is disregarded in favor of the assumption that they exclusively move along a straight path parallel to the y-axis. As a result of this approach, the movement of protons through the stack of voxels is computed only once, thanks to their unified entity status. Thus, voxels have information on the average number of protons, their common energy, and material composition. With this information known, the movement of protons between voxels of the phantom can start.

During each algorithm step, pre-tabulated data is used to generate outputs through specific mathematical models. This data includes information such as the average energy loss of protons per voxel in specific materials. Therefore, in each iteration, using these mathematical models, the algorithm calculates PES generation within each voxel and determines the fraction of protons moving forward with their respective reduced energy . This process continues until average proton energy reaches zero. It is important to note that this algorithm focuses solely on PES generation, excluding dose distribution calculations. Detailed information regarding the implementation of the fast algorithm is presented in sub-section 7.5.

The pre-tabulated data is obtained through Monte Carlo simulations for each material and it is stored in the form of Look-up-Tables (LUT). More detailed information regarding the LUT population can be found in the following sub-section.

7.2   LUT population

In order to effectively implement the fast algorithm, it is necessary to comprehend how protons interact with matter in various materials. As elucidated earlier, this crucial information is compiled in the form of a LUT and is obtained through the execution of Monte Carlo simulations. Importantly, this simulation process is conducted just once for each unique material.

For each material the LUT contains the following information obtained within a voxel for a specified energy range of proton:

- average reduction in the proton energy (Energy_Reduction)

- standard deviation of average reduction in the proton energy (Energ_Reduction_SD)

- fraction of the protons that:
    - leave the voxel:
        * forward (Protons_Forward)
        * sideways (Protons_Sideways)
        * backwards (Protons_Backwards)
    - are decreased due to inelastic interactions inside the voxel (Protons_Inside)

The LUT population process can be divided into three main aspects.

First, an ideal standalone voxel needs to be created so that proton interactions with matter can be studied and data gathered from it. Regarding the voxel geometry, it was decided to use a cylinder. In terms of dimensions, it was decided to use 1 mm for both the diameter and height of the cylinder. This size is chosen since it is the value used as the side length for box-shaped voxels in simulations using the probability-based algorithm, making later comparisons easier.

Second, the generation and tracking of protons will be carried out. Regarding proton generation, protons are generated inside the phantom micrometer away from the interface with the surrounding medium. This is done so that every proton interaction with matter occurs within the phantom, thus minimizing data mining mistakes. When it comes to proton tracking, the main purpose of the algorithm has to be considered. Since the objective of the algorithm is to generate PES only primary protons are to be tracked. This is because 97% of PES are produced from the interaction of primary protons with matter [Bauer et al., 2013], which makes it so that secondary particles can be disregarded.

Third, the process of data recording will be carried out. This process can be divided into two scenarios. One is to record the reduction in proton energy, and

the other is to record the coordinates where the proton track ended. In relation to the measurement of proton energy, there are two instances in which its recording occurs. The first instance is when protons leave the volume of the voxel, in which case the reduced energy equals the change in proton energy caused by their inter-action with matter inside the voxel. The second instance is when proton energy is reduced to zero within the volume of the voxel, so the reduced energy is equal to the initial energy of the proton when it is generated. Regarding the recording of the protons track end, after either the protons kinetic energy is decreased to zero or the protons leave the volume of the voxel, their tracking status is immedi-ately stopped and the position where it occurs is saved. When all protons tracks have ended, the saved positions are used to determine the fraction of protons that stopped inside the phantom or went forward, sideways, or backwards.

It is important to note that during data mining, protons that experienced elastic scattering were not considered in the recording of the reduction in proton energy. When this type of interaction occurs to a proton, Geant4 considers the reduction in proton energy to be close to the total kinetic energy of the proton. Thus, when protons have a high kinetic energy the energy loss during this process is high when compared to the average reduction in the proton energy within a voxel. If the percentage of elastic scattering occurring were to be small there would be no problem since its energy loss values would be offset by those from other types of interactions in a sample where a considerable number of protons are used. The problem is that for high energy protons the chances of it experiencing elastic scattering is in the range of 20% (Figure 7.1). Therefore, this particular process was disregarded in order to reduce the statistical fluctuations of the reduction in proton energy data.
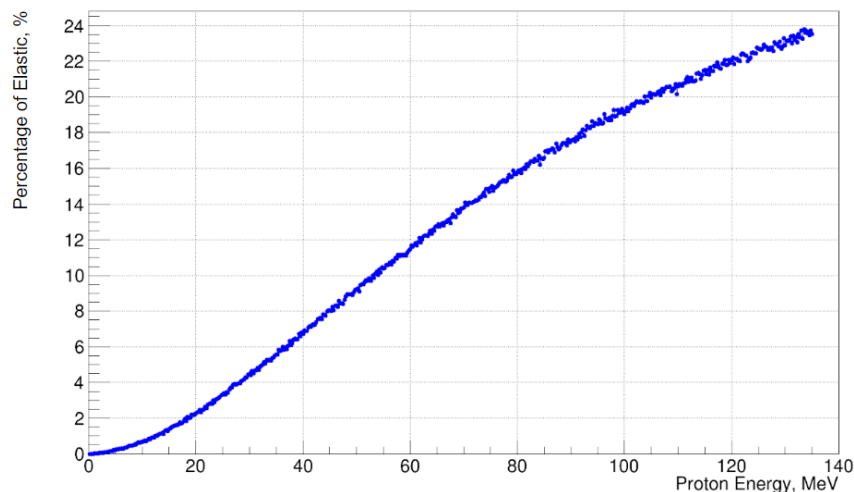
Figure 7.1: Percentage of protons that experience elastic scattering per proton energy in PMMA phantom

Now that all of the mechanisms involved in the data mining phase have been pre-sented, it is necessary to determine the parameters that must be used so that data values obtained for a specified energy range of protons through simulation are closely aligned with those obtained through an experiment. The most important parameter is the number of generated protons in the phantom. This quantity in-

fluences the statistical fluctuations seen in data values, showing that when there are more protons generated, more data is collected, leading to improved accuracy. However, because timing is also an important factor in these simulations, it is necessary to know after which increase in the number of generated protons there is no longer a change in data statistical fluctuations. After collecting data using different numbers of protons, it was observed that after 10^7 protons, the discrepancies in the obtained results become negligible.

In addition to the previously mentioned parameter, it is important to also take into account the energy step after which a new set of protons are generated, ensuring that their corresponding data is collected. The selection of an optimal value for this parameter is very important in the implementation of the algorithm, since it can greatly influence its time of execution. Due to this reason, a value of 0.1 MeV was chosen. The reasoning behind this decision is interconnected with the method used to extract data from the LUT (see sub-section 7.3 for more information).

Using a PMMA phantom two main graphs can be constructed using information from the created LUT:

Figure 7.2: Average reduction in proton energy for 1 mm voxel in PMMA phantom

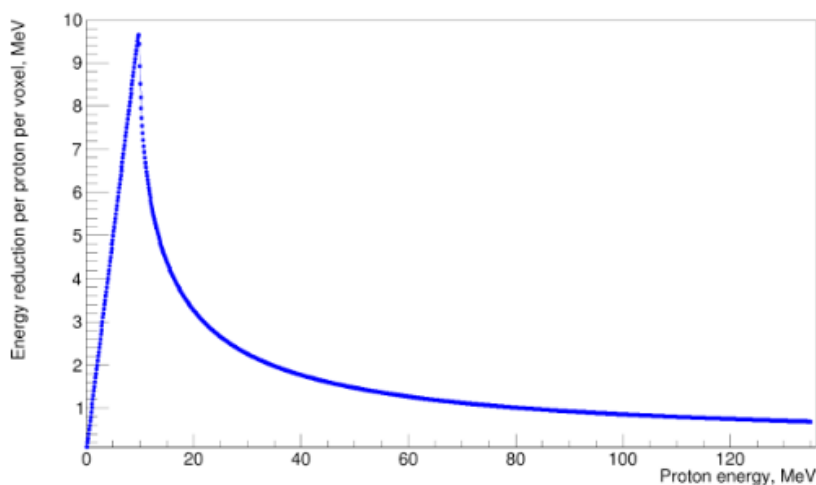Figure 7.2 shows the average reduction in proton energy inside 1 mm voxel. It can be seen that until 9.5 MeV, all protons energy is dissipated within 1 mm. After this point, the average reduction in proton energy for 1 mm exhibits a different pattern, which is characterized by an exponential decay-like behavior.
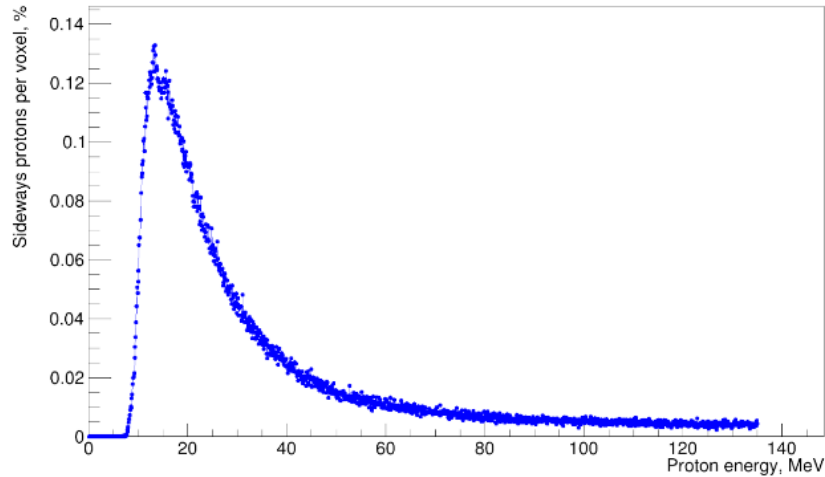
72

Figure 7.3: Fraction of sideways exiting protons from a 1 mm diameter PMMA voxel for an interval of proton energies

Figure 7.3 shows that when only the interactions confined within the 1 mm diameter voxel are considered, the fraction of protons that manage to travel sideways is very small.

In terms of the number of protons that travel backwards, the data obtained using the PMMA phantom showed that this process is extremely rare, so it can be completely ignored in the algorithm's application.

7.3   Data extraction from LUT

When applying the mathematical models of the fast algorithm to the information contained in a voxel, it is necessary to extract the proton related data from the LUT. Upon the start of a simulation conducted using the fast algorithm, depending on the composition of the phantom, LUTs are automatically loaded. The search of LUT data can be divided in two phases.

The first phase, since there might be more than one LUT accessible in the simulation, is to determine which LUT is necessary for the considered voxel. As already mentioned, each voxel contains information regarding the type of material it is composed of. This information is stored in the form of the index assigned by Geant4 for that material at the beginning of the simulation. Thus, a search is executed to find the respective LUT based on this number.

The second phase is to obtain the proton related information for a certain energy. Because the goal of the algorithm is to obtain the results as quickly as possible, the search for this information has to be done in the most effective way time-wise. Therefore, possible methods such as linear interpolation and binary search were excluded, and a method to immediately obtain the index (term used to distinguish the location where information is stored) of the necessary information in the LUT was used. This method obtains the index by dividing the intended proton energy with the energy step used in the LUT which is then considered as

an integer value. Through this method, the acquired proton-related information pertains to the requested energy rounded to the nearest value available in the LUT. To ensure minimal disparities between the obtained information and the requested data, it is imperative to employ a small energy step. In the investigation, it was found that using a step interval of 0.1 MeV yielded results very similar to those obtained using linear interpolation.

7.4 Proton lateral straggling

In the implementation of the fast algorithm, proton lateral straggling was disregarded and protons are treated as only moving parallel to the y axis. To ascertain the feasibility and applicability of this approach, an investigation is necessary. This algorithm was developed so that it could be used to obtain the spatial distribution of produced PES based on the source characteristics of the MD Anderson Cancer Center, thus, the source used for this study is the MDA beam.

Therefore, this study delves into two distinct scenarios involving the utilization of the MDA beam: one is to study the divergence of the beam and the other is to analyze the beam broadening in the phantom.

7.4.1 Divergence of the beam

The purpose of the first assessment is to evaluate the effect that the divergence of the MDA beam has on transportation of the protons in a certain volume. In order to do so, it is necessary to describe how the protons are generated in accordance with the beam setup at MD Anderson Cancer Center. The origin of the generated protons is a point situated 2520 mm away from the isocenter (Y direction, offsets in X and Z are zero). The position where the protons would hit the iso-plane is then generated based on a Gaussian distribution. In accordance with the dataset provided by MD Anderson, for the initial energy of the proton beam (135 MeV) this Guassian has a FWHM of about 20 mm , which corresponds to a sigma of 8.5 mm.

Thus, in accordance with this distribution, 95% percent of protons arrive at the iso-plane within 17 mm (2 x sigma) range in both X and Z directions. Knowing this distance, the lateral shift that occurs in the volume due to the MDA beam can be calculated. In order to obtain this value a geometrical comparison between two triangles is executed. The first triangle is constructed considering the position where protons are generated and hit the iso-plane and the second triangle is constructed considering a position 100 mm inside the volume.This process is illustrated in Figure 7.4.

From the congruency of the triangles, it becomes possible to use the ratio of their respective catheti, leading to the derivation of the following equivalence:

$$z_2 = \frac{z_1}{y_1} \times y_2 = \frac{16.98}{2429} \times 100 = 0.7mm \tag{7.1}$$

From this comparison, it was observed that the lateral shift for the considered range (17 mm), attributed to the beam's divergence within the volume, reaches a maximum deviation of 0.7 mm. This is the maximum lateral shift, so it means that for the majority of protons the observed lateral shift is even less. This observation suggests that proton transportation can be done along the stack of voxels (parallel to the y-axis). However, it is crucial to emphasize that this observation does not account for proton interactions with matter. Therefore, further evidence is necessary to evaluate the impact of proton lateral straggling on the overall dynamics of proton transportation.
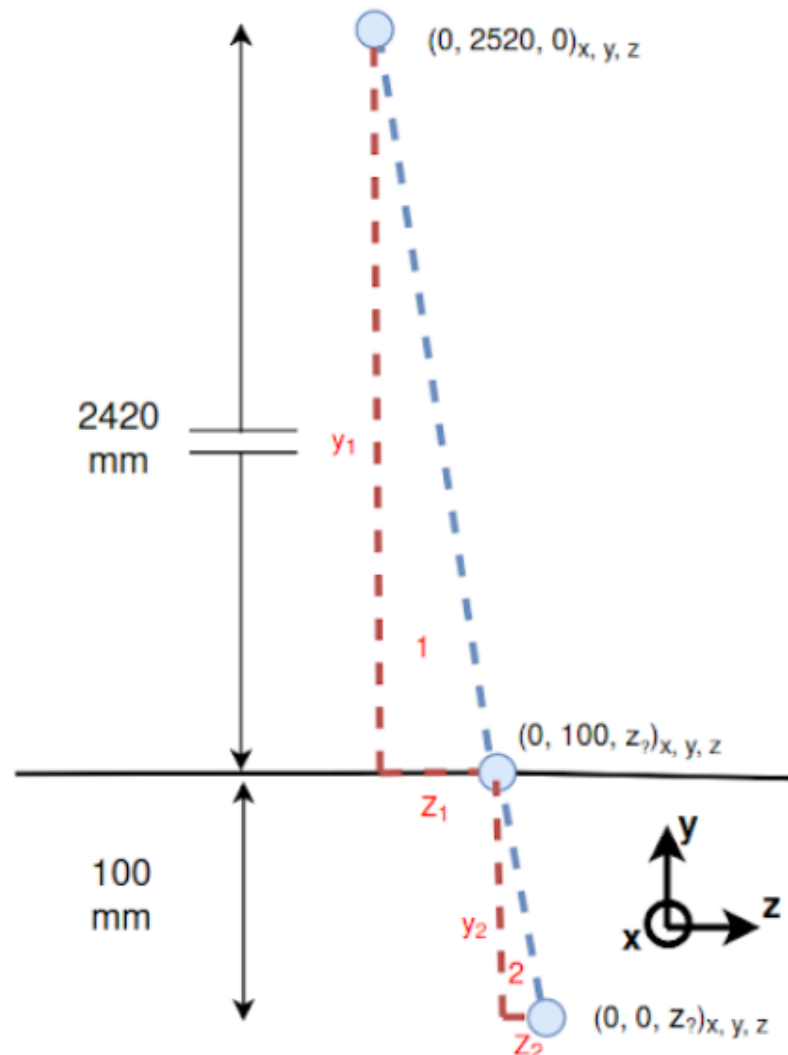
Figure 7.4: Illustration of the geometrical forms created based on the MDA beam

7.4.2 Analysis of beam broadening in a phantom

Second assessment is used to observe the broadening that occurs to the MDA beam inside the phantom due to lateral straggling of the protons. In order to obtain results regarding this broadening, a simulation using 10^5 protons was conducted using a PMMA phantom, from which the proton fluence (number of protons passing through an infinitesimal element of area perpendicular to the beam)
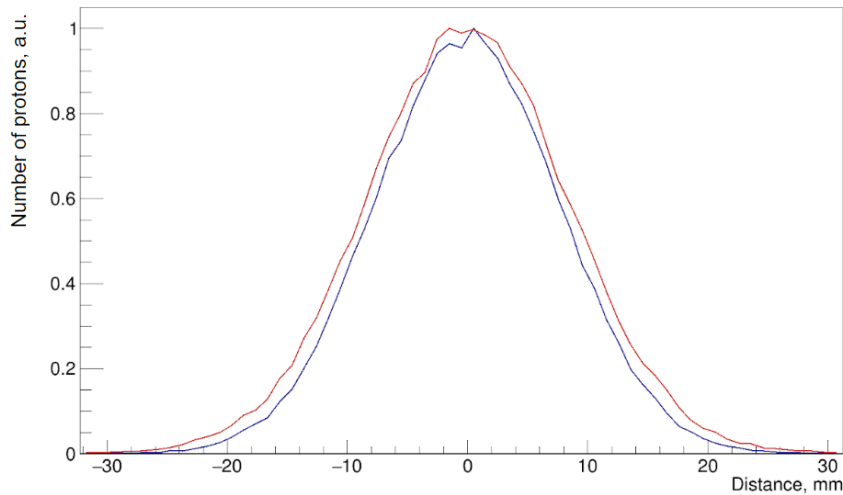
Figure 7.5: Projections of a perpendicular profile of the MDA beam at the beginning of the PMMA phantom (blue curve) and Bragg peak region (red curve)

[Gottschalk, 2011] was registered in a ASCII file. This file was used to plot the proton fluence. From this graphical representation a perpendicular profile of the beam was obtained at the beginning of the phantom and at the Bragg peak region (Figure 7.5).

Comparing both projections, it can be seen that the broadening of the beam inside the phantom is in the range of approximately 1 mm (red curve expanded in comparison to blue curve). Since the beam has 20 mm FWHM, this value of broadening can be considered negligible.

These findings suggest the proton lateral straggling is negligible in the case of the MDA beam. Therefore, this process can be disregarded and the assumption that protons only move in a direction parallel to the y axis can be adopted.

7.5   Implementation of the fast algorithm

This sub-section describes the implementation of the fast algorithm when using the MDA beam.

When the fast algorithm simulation is initialized the phantom is divided into equally sized voxels. Each of these voxels is unique, meaning that each one can be identified according to a set of indices depending on their coordinates (Figure 7.6). Each voxel is assigned the index of a material depending on the composition of the phantom in that volume.

Figure 7.6: Illustration of a phantom division into voxel with their respective indices

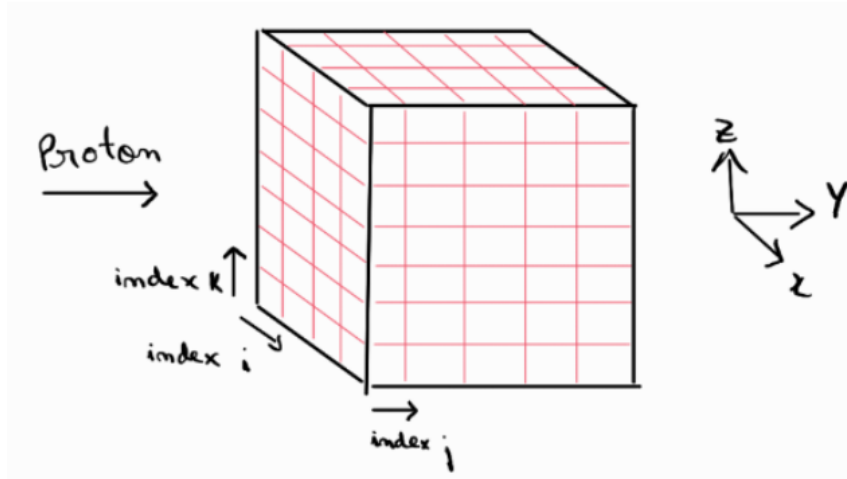After the phantom division, generated protons are allocated to the first slice of voxels (index j = 0) of the phantom according to the spatial distribution characteristic of the MDA beam.

Upon the completion of proton allocation, the subsequent phase involves the application of fast algorithm mathematical models to individual voxels. In this simulation scenario, the initial voxel slice comprises multiple discrete voxels. Consequently, there is a chance that certain voxels may contain no protons, necessitating the sequential application of the fast algorithm's mathematical models to the subsequent voxel within the initial slice. On the other hand, if the new voxel contains protons, these mathematical models are iteratively employed along the stack of voxels until proton transportation is no longer possible due to the kinetic energy of protons reaching zero.

In each iteration of the algorithm, using the proton related information extracted from the LUT, three outputs are generated based on the application of the mathematical models. These outputs encompass the average number of protons that "survive" and move forward, the proton energy subsequent to energy reduction and the total number of PES produced in the voxel.

In the following sub-sections the mathematical models of the fast algorithm are presented.

7.5.1 Average number of protons in a voxel

The average number of protons (Number_Protons) that move to the next voxel is determined according to the following expression:

$$Number\_Protons_{j+1} = Number\_Protons_j \times (Protons\_Forward_j + Protons\_Sideways_j)$$
$$(7.2)$$

As it was presented in sub-section 7.4 proton lateral straggling is disregarded

when using a MDA beam. Therefore, the associated fraction of protons (Protons_Sideways) is included in the fraction of those that move forward. This is done because the fraction of protons that travel sideways, although reduced, cannot simply disappear without depositing their energy.

The data collected from the fast algorithm for proton fluency was compared to the fluency of protons obtained using Monte Carlo simulations. A PMMA phantom was used to collect this data.
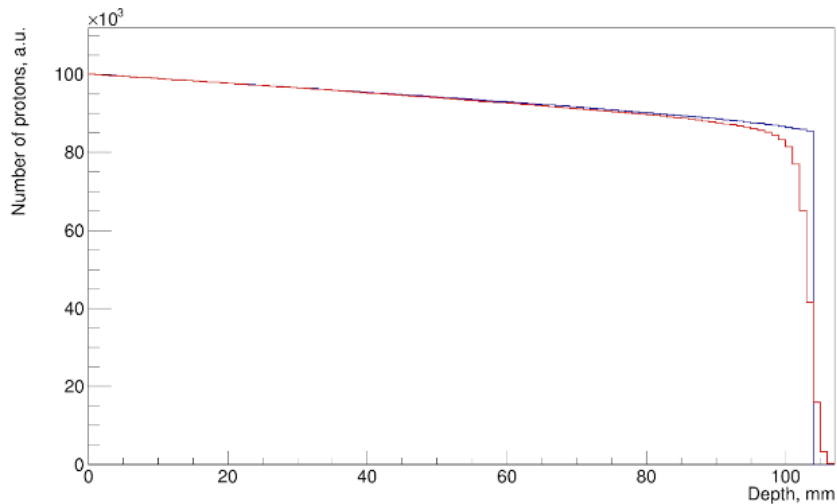
Figure 7.7: Proton fluency along the beam direction given by the fast algorithm (blue curve) and the Monte Carlo simulation (red curve) for a PMMA phantom using the MDA beam

As shown in Figure 7.7, both curves match well at shorter depths. After about 45 mm, the curves begin to diverge, with the main differences occurring close to the 100 mm region, where the fast algorithm's curve has a sharp decrease and the MC's curve a more slower decrease. Lastly, it can be seen that the fast algorithm delivers a good proton range prediction.

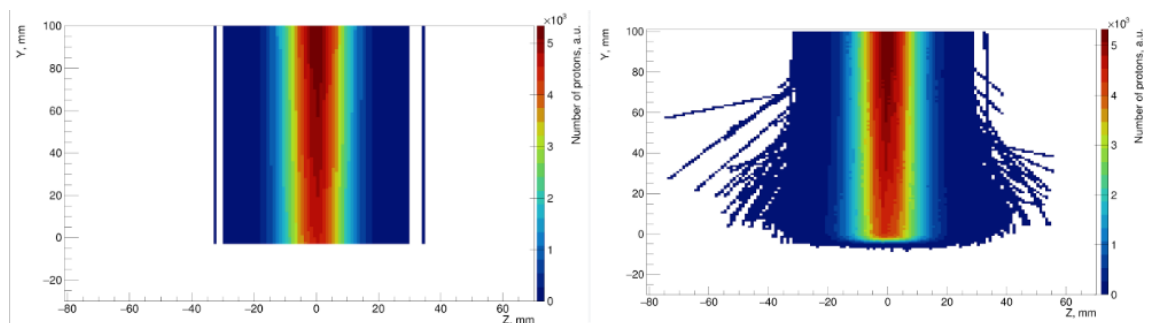Figure 7.8: 2D projection of proton fluency given by the fast algorithm (left) and Monte Carlo simulations (right) for a PMMA phantom using he MDA beam

When analyzing proton fluency through the 2D projections shown in Figure 7.8, it becomes evident that both algorithms yield comparable beam shapes. The pri-

mary distinction between the two graphical representations lies in the region beyond the Z-axis interval spanning from -30 mm to 30 mm. Notably, the disparity arises due to the omission of proton lateral straggling in the fast algorithm (Figure 7.8 left). Nevertheless, it is worth noting that, as shown in Figure 7.8 right, this phenomenon affects only a limited number of protons, thereby mitigating its substantial impact on the overall results.

7.5.2 Proton energy in a voxel

The proton energy (Proton_Energy) to be passed to the next voxel is determined according to the following expression:

$$Proton\_Energy_{j+1} = Proton\_Energy_j - Energy\_Reduction_j \qquad (7.3)$$

The data collected for the fast algorithm on proton energy was compared to the energies of protons per millimeter of depth obtained using Monte Carlo simulations along the beam. This data was collected using a PMMA phantom and 10^5 protons.
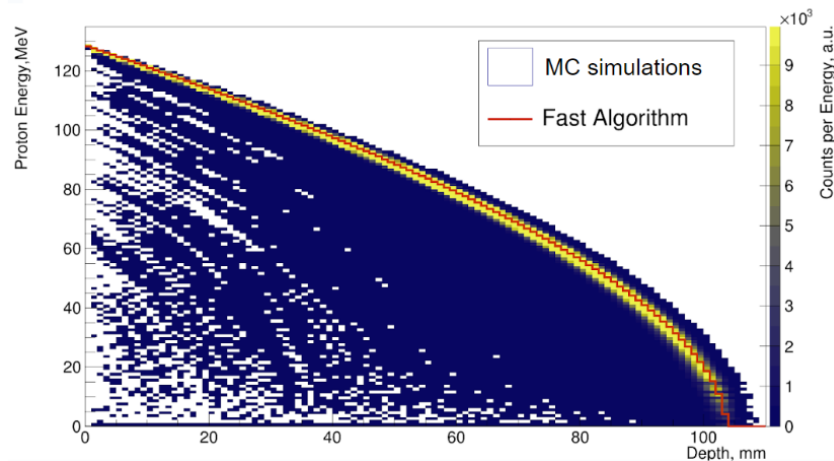
Figure 7.9: Proton energy along the beam using fast algorithm vs proton energy values per millimeter of depth given by Monte Carlo simulations for a PMMA phantom using the MDA beam

As shown in Figure 7.9, focusing on the results obtained using the Monte Carlo simulations it can be seen that the most probable values of proton energy per millimeter of depth (yellow region) get progressively wider as lower depths are taken into consideration. When the results obtained using the fast algorithm are taken into account, it can be seen that the proton energy per millimeter of depth is in accordance with the anticipated behavior since its values are inside the yellow region. The major difference occurs for depths >104 mm where the proton energy obtained using the fast algorithm has reached zero which is not the case for the Monte Carlo simulation results.

7.5.3 Number of produced PES in a voxel

In this algorithm the time when PES are produced (timestamp) was not considered. For each voxel the total number of produced PES is determined for each nuclear reaction. This value is determined by the number of protons in the voxel as well as the probability of creating all possible PES in the material present in the voxel. The probability of each PES is determined by the isotope from which it is derived, specifically its energy dependent cross-section (CS) and number density (ND).

This algorithm is limited to certain nuclear reaction channels depending on the cross-sections available. At the moment the reactions considered are the same presented for the Monte Carlo approach (Chapter 5 sub-section 5.2): 12C(p, pn)11C, 16O(p, 3p3n)11C, 16O(p, pn)15O, 16O(p, 2p2n)13N, 40Ca(p, 2pn)38K and 31P(p, pn)30P.

So in order to get the total number of each individual produced PES per voxel the following expression is used:

$$Produced\_PES_j = Number\_Protons_j \times CS_{PES} \times ND_{Parent isotope PES} \qquad (7.4)$$

To assess the algorithm's effectiveness, results from the fast algorithm using different phantoms were compared to those obtained from the probability-based algorithm under the same simulation conditions.

To test the implementation of the algorithm a HDPE phantom, which is rich in the carbon element, was used. Under these conditions, the following results were obtained:

Figure 7.10: 1D distribution of the total number of produced PES along the beam for a HDPE phantom given by the fast algorithm (blue curve) vs probability-based algorithm (red curve) using the MDA beam

Figure 7.10 shows that the curves given by both algorithms have similar patterns, particularly at shorter depths where they match well. The issue arises after the

peak of the curves, when the total number of PES produced by the fast algorithm is slightly higher. This problem is discussed in sub-section 7.5.4.

To test the implementation of the algorithm in another material a PMMA phantom, which besides carbon also contains oxygen, was used. Under these conditions, the following results were obtained:
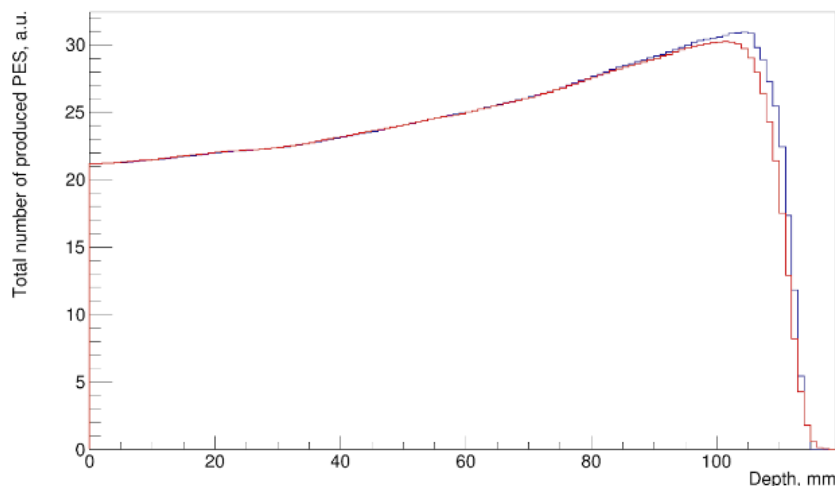

Figure 7.11: 1D distribution of the total number of produced PES along the beam for a PMMA phantom given by the fast algorithm (blue curve) vs probability-based algorithm (red curve) using the MDA beam. The arrow indicates the region where the fast algorithm curve produces a greater number of PES in relation to the probability-based algorithm.

Figure 7.11 shows that despite the material considered being different, the results given by both algorithms still match well for short depths, and the problem occurs in the region after the curve peaks. Additionally, in this phantom, there was a greater increase in the total number of PES produced by the fast algorithm at the end of the curve (region pointed by an arrow). This problem is discussed in sub-section 7.5.4.

To test the implementation of the algorithm in a non-homogeneous phantom, a phantom composed of three different materials was created. Under these conditions, the following results were obtained:
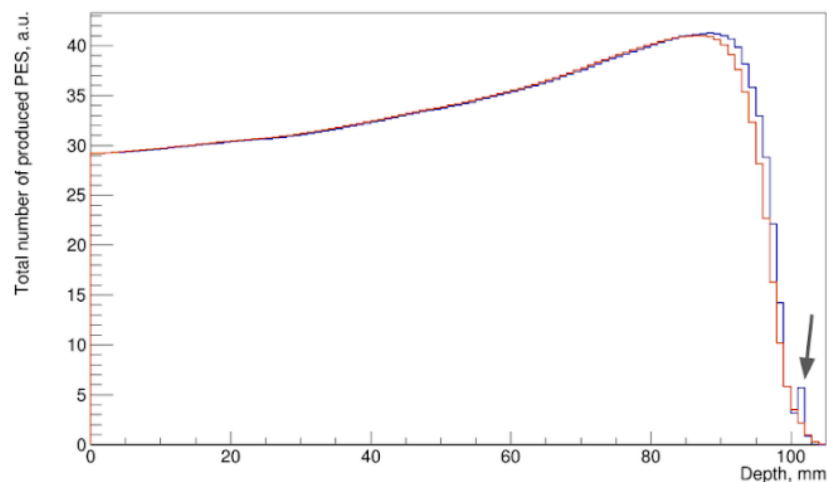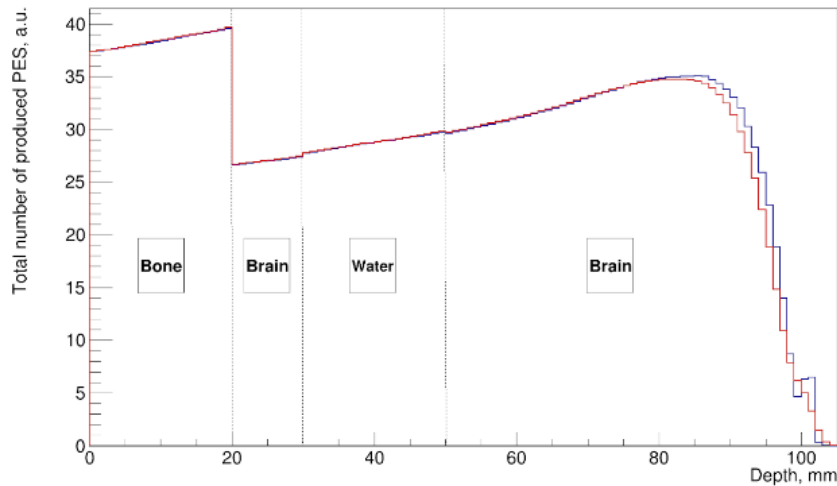
Figure 7.12: 1D distribution of the total number of produced PES along the beam in a non-homogeneous phantom given by the fast algorithm (blue curve) vs probability-based algorithm (red curve) using the MDA beam

It can be seen that for this type of phantom, the results given by the fast algorithm still match well for short depths and that the problem arises in the region after the peak of the curves. This implies that the implementation of the fast algorithm is applicable to all types of materials.

7.5.4   Challenges of the fast algorithm

All the results presented in sub-section 7.5 consistently indicate that the problem with this fast algorithm occurs near the region of the curve's distal edge, where the number of produced PES remains high before gradually reducing to zero. The main reason for this occurring is that in this region of depth, the average number of protons considered using the fast algorithm is not coherent with what occurs in reality, which can be approximately represented by the probability-based approach. It is in fact slightly higher as it can be seen from Figure 7.7. Since the average number of protons in a voxel is higher than what it is supposed to be, it is natural that the number of produced PES obtained using the fast algorithm, which depend on the number of protons in the voxel (Equation 7.4), is higher than those obtained using the probability-based algorithm (Figures 7.10, 7.11 and 7.12). Figures 7.11 and 7.12 have a higher increase in the number of produced PES near the end of the fast algorithm curve (region pointed by the arrow). This increase is due to the presence of ^{16}O in the phantom, which can lead to the creation of ^{13}N, with a comparatively higher cross-section in the lower range of proton energies than the other nuclear reactions (Figure 5.2 of chapter 5). Thus, this reason added to the fact that the average number of protons is not properly spatially distributed leads to the wrong increase of PES near the end of the fast algorithm's curve.

The reason behind the problem mentioned above is the method used to process the reduction in proton energy, since the implemented method the kinetic energy

of protons reaches zero at shorter distances than what it should (Figure 7.9). This problem was identified but not solved due to time constraints.

7.6   Algorithm run time

The purpose of developing this algorithm was so that results regarding the production of PES could be obtained faster than those given by the Monte Carlo approaches. Thus, in this sub-section a comparison between the running time of this algorithm versus the probability-based algorithm (fastest algorithm that uses MC simulations) is presented. The simulation running time for both algorithms varies depending on the materials presented in the phantom, but it can be seen that under the same simulation conditions, the results of the fast algorithm can be obtained approximately two orders of magnitude faster than the probability-based algorithm when using one beamlet of the MDA beam. Note that in the administration of the treatment, 1000 beamlets are used.

For example, for a PMMA phantom using the fast algorithm the simulation total run time is equal to 0.3 seconds per beamlet. Using the probability-based algorithm the simulation total run time is equal to 46.8 seconds per beamlet.

Chapter 8

Conclusions

The TPPT Consortium is currently engaged in the development of an in-beam TOF-PET system prototype for proton therapy range verification. This project is motivated by the numerous advantages offered by this approach in contrast to the offline PET, including the notable reduction in biological washout and the minimization of patient discomfort due to the substantially shorter imaging duration. Additionally, since the quantity of beta plus decays available for detection when using in-beam PET is higher than in offline PET it contributes to an improvement in the number of coincidences used to generate PET images.

In order to simulate the operation of the TOF-PET prototype designed by the TPPT consortium, a framework was developed using the Geant4 toolkit. However, a notable limitation of this framework was its reliance on Monte Carlo simulations, which can be a problem due to its substantial computational costs. Given the necessity for conducting daily fractions in proton therapy administration, rapid generation of activity results is imperative. Therefore, an alternative to the brute-force algorithms had to be provided, as it requires approximately 12 hours to compute the activity generated within a PMMA phantom using one beamlet with 10^8 protons utilizing a single processing thread. In contrast, the probability-based approach demonstrated substantial improvements, reducing this computation time by three orders of magnitude. Nevertheless, in the context of a clinical environment with numerous treatment sessions conducted each day and considering that the treatment plan of the MD Anderson Cancer Center comprises a substantial number of beamlets (~1000 in total), coupled with the utilization of an anthropomorphic phantom, which increases even more the computational costs, it becomes evident that further optimization is required to ensure timely beam range verification.

Using the probability-based algorithm the range of positrons was studied in brain and bone tissue. It was found that the positron range only has a significant impact on bone activity. Therefore, for the accurate simulation of PET image reconstruction within a bone region, it is necessary to conduct positron generation prior to gamma pair production. On the other hand, in the case of a brain region, it is possible to skip the positron generation process and directly generate gamma pairs at the point of PES decay.

Given the considerable computational costs associated with Monte Carlo-based algorithms, a more efficient algorithm was developed during work on this thesis to attain the spatial distribution of produced PES within a phantom. The principal strategy for improving computational efficiency involves eliminating the need for individual proton tracking within the phantom. Instead, the algorithm simplifies proton transportation within the phantom by treating protons within each voxel as a single entity and assuming they move in a straight line along the beam axis. This method allows to perform tracking along a stack of voxels only once.

The new algorithm exhibits promising results in PES generation, since it reduces the computation time by two orders of magnitude when compared to the probability-based algorithm. However, proton fluence near the end of the proton path is not accurately represented resulting in a slightly lower mean proton range in comparison to the probability-based algorithm by approximately 2 mm. Therefore, this discrepancy affects the production of PES within this specific region, resulting in the fast algorithm yielding a slightly higher number of PES than the probability-based algorithm.

Future Work

The considerations presented in "Conclusions" emphasize the need for further enhancement of the fast algorithm developed in this work.

To resolve the problem regarding the inaccuracies in proton fluence determination, a new methodology for processing proton energy reduction is proposed. This method differs from the current assumption that protons within a voxel have a single energy value. Instead, it suggests that protons exhibit a distribution of energies. Consequently, when processing the reduction in proton energy, the algorithm determines the energy decrease for various proton energy levels, depending on the energy step considered for analysis. In this process, each energy reduction value is utilized to construct a Gaussian distribution, which is then convoluted with the corresponding proton energy value. The resultant curve represents the distribution of proton energy for the subsequent voxel. In essence, this new approach rejects the notion that energy reduction within a voxel remains constant.

In addition to the fast algorithm, should MD Anderson Cancer Center provide access to their therapy planning software which includes the algorithm for ascertaining the proton fluence spectrum within the proton energy domain, an alternative approach could be used to reduce timing results with an increase in accuracy of produced PES. This approach makes use of the enhanced accuracy of proton number and energy data as they traverse the voxels within the phantom. Coupled with knowledge of material properties, the methodology employed in the fast algorithm to generate the PES can be implemented. This collaborative synergy between algorithms promises to yield significant advancements in both the temporal efficiency and accuracy of results regarding the number of produced PES.

References

F Abouzahr, J P Cesar, P Crespo, M Gajda, Z Hu, W Kaye, K Klein, A S Kuo, S Majewski, O Mawlawi, and et al. The first PET glimpse of a proton FLASH beam. *Physics in Medicine and Biology*, 68(12):125001, 2023. doi: 10.1088/1361-6560/acd29e.

D. L. Bailey. *Nuclear medicine physics: A handbook for teachers and students*. IAEA, 2015.

S Banerjee, G Folger, A Ivanchenko, V N Ivanchenko, M Kossov, J M Quesada, A Schälicke, V Uzhinsky, H Wenzel, D H Wright, and et al. Validation of geant4 hadronic generators versus thin target data. *Journal of Physics: Conference Series*, 331(3):032034, 2011. doi: 10.1088/1742-6596/331/3/032034.

J Bauer, D Unholtz, C Kurz, and K Parodi. An experimental approach to improve the Monte Carlo modelling of offline PET/CT-imaging of positron emitters induced by scanned proton beams. *Physics in Medicine and Biology*, 58(15): 5193–5213, 2013. doi: 10.1088/0031-9155/58/15/5193.

Brian C. Baumann, Nandita Mitra, Joanna G. Harton, Ying Xiao, Andrzej P. Wojcieszynski, Peter E. Gabriel, Haoyu Zhong, Huaizhi Geng, Abigail Doucette, Jenny Wei, Peter J. O'Dwyer, Justin E. Bekelman, and James M. Metz. Comparative Effectiveness of Proton vs Photon Therapy as Part of Concurrent Chemoradiotherapy for Locally Advanced Cancer. *JAMA Oncology*, 6(2):237–246, 02 2020. ISSN 2374-2437. doi: 10.1001/jamaoncol.2019.4889. URL `https://doi.org/10.1001/jamaoncol.2019.4889`.

Britannica, 2018. URL `https://www.britannica.com/science/cross-section-physics`. Accessed on September 08, 2023.

P Cambraia Lopes, J Bauer, A Salomon, I Rinaldi, V Tabacchini, T Tessonnier, P Crespo, K Parodi, and D R Schaart. First in situ TOF-PET study using digital photon counters for Proton Range verification. *Physics in Medicine and Biology*, 61(16):6203–6230, 2016. doi: 10.1088/0031-9155/61/16/6203.

Genevieve Chaput and Laura Regnier. Radiotherapy. *Canadian Family Physician*, 67(10):753–757, 2021. doi: 10.46747/cfp.6710753.

Simon R. Cherry, Michael E. Phelps, and Magnus Dahlbom. *Pet: Physics, instrumentation, and scanners*. Springer, 2011.

Jongmin Cho. *USE OF POSITRON EMISSION TOMOGRAPHY FOR PROTON THERAPY VERIFICATION*. PhD thesis, The University of Texas MD Anderson Cancer Center UTHealth Graduate School of Biomedical Sciences, 2014.

CMG, 2018. URL `https://cmgi.ucdavis.edu/services/positron-emission-tomography-pet/`. Accessed on September 08, 2023.

Paulo Crespo, Georgy Shakirin, Fine Fiedler, Wolfgang Enghardt, and Andreas Wagner. Direct time-of-flight for quantitative, real-time in-beam PET: A concept and feasibility study. *Physics in Medicine and Biology*, 52(23):6795–6811, Nov 2007. doi: 10.1088/0031-9155/52/23/002.

W Enghardt, P Crespo, F Fiedler, R Hinz, K Parodi, J Pawelke, and F Pönisch. Charged hadron tumour therapy monitoring by means of PET. *Nuclear Instruments and Methods in Physics Research Section A: Accelerators, Spectrometers, Detectors and Associated Equipment*, 525(1):284–288, 2004. ISSN 0168-9002. doi: https://doi.org/10.1016/j.nima.2004.03.128. URL `https://www.sciencedirect.com/science/article/pii/S0168900204004218`. Proceedings of the International Conference on Imaging Techniques in Subatomic Physics, Astrophysics, Medicine, Biology and Industry.

EPA, 2023. URL `https://www.epa.gov/radiation/radioactive-decay`. Accessed on September 08, 2023.

M. A. Flower. *Webb's physics of Medical Imaging*. CRC PRESS, 2nd edition, 2016.

GCO, 2020. URL `https://gco.iarc.fr/today/home`. Accessed on September 08, 2023.

Geant4, 2023. URL `https://geant4-userdoc.web.cern.ch/UsersGuides/ForApplicationDeveloper/html/index.html`. Accessed on September 08, 2023.

github. Tpptsim, 2023. URL `https://github.com/andrmor/TPPTsim`. Accessed on September 08, 2023.

Gottschalk, 2011. URL `https://gray.mgh.harvard.edu/attachments/article/337/Techniques%20of%20Proton%20Radiotherapy%20(04)%20Basics.pdf`. Accessed on September 08, 2023.

Claus Grupen, Ulrich Werthenbach, and Tilo Stroh. *Introduction to radiation protection: Practical knowledge for handling radioactive sources*. Springer, 2010.

S. Guatelli, Dean Cutajar, B. Oborn, and Anatoly Rosenfeld. Introduction to the geant4 simulation toolkit. *AIP Conference Proceedings*, 1345:303–322, 05 2011. doi: 10.1063/1.3576174.

Felix Horst, Wihan Adi, Giulia Aricò, Kai-Thomas Brinkmann, Marco Durante, Claire-Anne Reidel, Marta Rovituso, Uli Weber, Hans-Georg Zaunick, Klemens Zink, and et al. Measurement of PET isotope production cross sections for protons and carbon ions on carbon and oxygen targets for applications in particle therapy range verification. *Physics in Medicine and Biology*, 64(20):205012, 2019. doi: 10.1088/1361-6560/ab4511.

Antje-Christin Knopf and Antony Lomax. In vivo proton range verification: A review. *Physics in Medicine and Biology*, 58(15), Jul 2013. doi: 10.1088/0031-9155/58/15/r131.

Kryder, 2017. URL `https://www.ilcn.org/proton-beam-therapy-versus-photon-beam-therapy-the-debate-continues/`. Accessed on September 08, 2023.

Jonathan E Leeman, Paul B Romesser, Ying Zhou, Sean McBride, Nadeem Riaz, Eric Sherman, Marc A Cohen, Oren Cahlon, and Nancy Lee. Proton therapy for head and neck cancer: Expanding the therapeutic window. *The Lancet Oncology*, 18(5), Apr 2017. doi: 10.1016/s1470-2045(17)30179-1.

William R. Leo. *Techniques for nuclear and particle physics experiments: A how-to approach*. Springer-Verlag, 1994.

Matis, 2001. URL `https://www2.lbl.gov/abc/wallchart/chapters/07/0.html`. Accessed on September 08, 2023.

Mayo, 2022. URL `https://www.mayoclinic.org/tests-procedures/cancer-treatment/about/pac-20393344`. Accessed on September 08, 2023.

Sanga Mitra, Sayak Ganguli, and Jayprokas Chakrabarti. Chapter 1 - introduction. In Dr. Jayprokas Chakrabarti and Dr. Sanga Mitra, editors, *Cancer and Noncoding RNAs*, volume 1 of *Translational Epigenetics*, pages 1–23. Academic Press, Boston, 2018. doi: https://doi.org/10.1016/B978-0-12-811022-5.00001-2. URL `https://www.sciencedirect.com/science/article/pii/B9780128110225000012`.

M Moteabbed, S España, and H Paganetti. Monte Carlo Patient Study on the comparison of prompt gamma and PET imaging for range verification in Proton therapy. *Physics in Medicine and Biology*, 56(4):1063–1082, Jan 2011. doi: 10.1088/0031-9155/56/4/012.

NCI, 2021. URL `https://www.cancer.gov/about-cancer/understanding/what-is-cancer`. Accessed on September 08, 2023.

Nuclear-power, 2018. URL `https://www.nuclear-power.com/nuclear-power/reactor-physics/interaction-radiation-matter/interaction-heavy-charged-particles/bragg-curve-bragg-peak/`. Accessed on September 08, 2023.

H Paganetti and G El Fakhri. Monitoring proton therapy with PET. *The British Journal of Radiology*, 88(1051):20150173, Jun 2015. doi: 10.1259/bjr.20150173.

Harald Paganetti. Range uncertainties in proton therapy and the role of Monte Carlo Simulations. *Physics in Medicine and Biology*, 57(11), 2012. doi: 10.1088/0031-9155/57/11/r99.

E. B. Podgorsak. *Radiation oncology physics: A handbook for teachers and students*. International Atomic Energy Agency, 2005.

Ervin B. Podgoršak. *Interactions of Photons with Matter*, pages 277–375. Springer Berlin Heidelberg, Berlin, Heidelberg, 2010. ISBN 978-3-642-00875-7. doi: 10.1007/978-3-642-00875-7_7. URL https://doi.org/10.1007/978-3-642-00875-7_7.

Radiology-key, 2016. URL https://radiologykey.com/positron-emission-tomography/. Accessed on September 08, 2023.

Samik Raychaudhuri. Introduction to Monte Carlo simulation. *2008 Winter Simulation Conference*, Dec 2008. doi: 10.1109/wsc.2008.4736059.

Eric M. Rohren, Timothy G. Turkington, and R. Edward Coleman. Clinical applications of PET in Oncology. *Radiology*, 231(2):305–332, 2004. doi: 10.1148/radiol.2312021185. URL https://doi.org/10.1148/radiol.2312021185. PMID: 15044750.

Dennis R Schaart. Physics and technology of time-of-flight PET detectors. *Physics in Medicine and Biology*, 66(9), Apr 2021. doi: 10.1088/1361-6560/abee56.

AK Shukla and Utham Kumar. Positron emission tomography: An overview. *Journal of Medical Physics*, 31(1):13–21, 2006. doi: 10.4103/0971-6203.25665.

Margarida Nunes Simões. Monte carlo simulation of an in-beam TOF-PET system for range monitoring in proton therapy, 2022. URL http://hdl.handle.net/10316/106057.

Shan Tong, Adam M Alessio, and Paul E Kinahan. Image reconstruction for PET/CT scanners: Past achievements and future challenges. *Imaging in Medicine*, 2(5):529–545, Oct 2010. doi: 10.2217/iim.10.49.

UT Austin Portugal, 2020. URL https://utaustinportugal.org/wp-content/uploads/2020/09/TOF-PET-.pdf. Accessed on September 08, 2023.

S. Vandenberghe, E. Mikhaylova, E. D'Hoe, P. Mollet, and J. S. Karp. Recent developments in time-of-flight pet. *EJNMMI Physics*, 3(1), Dec 2016. doi: 10.1186/s40658-016-0138-3.

Washington, 1999. URL https://depts.washington.edu/imreslab/from%20old%20SITE/pet_intro/intro_src/section2.html. Accessed on September 08, 2023.

Wright and Incerti, 2009. URL http://geant4.in2p3.fr/IMG/pdf_PhysicsLists.pdf. Accessed on September 08, 2023.

Aleksandra Wronska and Denis Dauvergne. Range verification by means of prompt-gamma detection in particle therapy. In K.Iniewski J.S. Iwanczyk, editor, *Radiation Detection Systems. Medical Imaging, Industrial Testing and Security Applications*, volume chapter 6, page 22 p. CRC Press, 2021. URL https://hal.science/hal-03085504.

Xuping Zhu and Georges El Fakhri. Proton therapy verification with PET imaging. *Theranostics*, 3(10):731–740, Sep 2013. doi: 10.7150/thno.5162.

Sibylle I. Ziegler. Positron emission tomography: Principles, technology, and recent developments. *Nuclear Physics A*, 752:679–687, 2005. doi: 10.1016/j. nuclphysa.2005.02.067.